

# Measuring and quantifying shunt currents in an alkaline water electrolyser shortstack

Dirk IJsbrand Roest

# Measuring and quantifying shunt currents in an alkaline water electrolyser shortstack

by

Dirk IJsbrand Roest

Student Name	Student Number
D. Roest	4485912

## **Master of Science Thesis**

For the degree of Master of Science in Sustainable Energy Technology  
at Delft University of Technology

Principal supervisor: J.W. Haverkort  
Daily supervisor: S. Phadke  
Project Duration: May, 2023 - March, 2024  
Faculty: Faculty of Process & Energy, Delft

# Preface

I am happy to present the following thesis report, which is the result of months of hard work. It marks the end of my academic journey at Delft University of Technology. I would like to take the opportunity to thank my supervisor, Willem Haverkort, for your continuous support and guidance through this project. The opportunity to work on this project and to gain a deeper understanding of electrolysis is something I was actively looking for. Thank you for giving it to me and for challenging me to take it to a higher level. Also, a big thanks to my daily supervisor, Sohan Phadke. Bringing this project from concept to realization would not have been possible without you. I learned a lot about paying more attention to detail due to your feedback.

I also want to thank the members of the research group that actively supported me throughout. Especially my predecessor on this project, Mehmet Pektas, for having such a helpful attitude toward me, even though there was no gain for you. During the start-up of this thesis I learned a lot from you about the design and concepts entailed in this thesis. Jelmer Postma, thank you for helping me with many Solidworks related questions and for playing a big role in showing me around the lab. Gilles deiters and Emile Craye, thank you for your helpful attitude in the lab and for being open to discussions about the topics relevant to this project. A special shout out goes to Hein Haverlag, with whom I journeyed from bachelor to master, to eventually doing a thesis project at the same research group. The laughter (and pain) we shared is something I value greatly.

Finally, my gratitude extends to my family and friends. Thank you mom and dad for supporting me and believing in me during everything. Thanks to my sister and brother for leading by example, and showing me how its done. Also, my girlfriend, for putting up with me and keeping me sane throughout this project.

*Dirk IJsbrand Roest  
Delft, March 2024*

# Abstract

Hydrogen is used in a variety of industrial applications and can function as a green energy carrier, if produced sustainably. Alkaline water electrolysis holds great promise as a production method for green hydrogen, potentially playing an important role in the energy transition. The performance of this technology depends significantly on its electrical efficiency. In some industrial-scale green hydrogen plants, multiple electrolysis cells are coupled together in series or in parallel to form a stack. These electrolyser stacks are being fed with a liquid electrolyte, often a KOH solution, which acts as a good conductor for ions to move between electrodes. The channels through which the electrolyte and gas products are transported in and out of the stack are usually connected to each other via manifolds. Electrolyzer stacks frequently encounter a problem known as shunt current, which is alternatively described as leakage, bypass, or parasitic current in various studies through these channels and manifolds. Mathematically describing the magnitude and nature of these shunt currents has been the topic of a variety of studies. Being able to adequately measure and quantify shunt currents in an actual stack remains a challenge. This study aims to measure and quantify shunt currents in a novel electrolyser stack design by the employment of hydrogen reference electrodes, copper or silver pseudoreference electrodes, and a magnetic current clamp. Numerous experimental findings have been coupled with mathematical models, imaging and theoretical expectations offering detailed insights in the behaviour of shunt currents with varying external factors. The variable parameters in this shunt current research are the applied current density to the stack and the applied liquid flow rate, by an external pump.

The performance of hydrogen reference electrodes, copper and silver wires separately, to measure potential differences in an electric field generated in the highly alkaline environment of a 6M KOH solution was validated. It was found that the hydrogen reference electrodes functioned accurately and stable, giving conductivity results of the electrolyte 7.5 % above measurements performed with a conductivity probe. The copper wires functioned less predictable and stable, giving values 16 % above the validated value, with a larger spread and less reproducibility. The silver wires showed great potential, providing a value of 3 % above the validated value, but showed less stability in measuring constant potential differences. The plain copper and silver wires only functioned for short term measurements, where a potential difference between a baseline potential was the only predictable outcome. Both lacking a stable redox potential, they were found not suitable for accurately measuring potential differences inside the stack.

The hydrogen reference electrodes proved to be useful in quantifying average manifold shunt currents, however leaving uncertainties as to total shunt currents in the experimental set-up used in this research. The magnetic current clamp was used to measure the current running through the external wiring between cells, from which the shunt current could be inferred. These measurements showed much potential in quantifying total shunt currents, but showed a large standard deviation between measurements due to the instantaneous nature of the measurements, alongside unpredictable electrode connections interfering with the outcomes. Both methods, however, were very successful in quantifying the behaviour of shunt currents with respect to varying parameters such as liquid flow rate and applied current. It has been shown that a liquid flow rate three times higher than the current density induced gas flow rate, leads to a constant shunt current through the manifolds. Gas flow rates 100 times higher than liquid flow rates leads to a near zero shunt current through the upper manifolds, and has no effect on the shunt currents through the lower manifold. This is because more gas in the upper manifolds lead to higher resistances, and thus lower shunt currents. In the situation where and gas and liquid flow rate are roughly equal, increasing the current density, and thus the gas flow rate, leads to a steady decrease in shunt currents through the upper manifold and a steady increase in shunt currents through the lower manifolds. This was the case for increasing the gas flow rate to at least two nearly three times the liquid flow rate. The total shunt current decreases in this case.

# Contents

<b>Preface</b>	<b>i</b>
<b>Summary</b>	<b>ii</b>
<b>1 Introduction</b>	<b>1</b>
1.1 Evolution of energy sources . . . . .	1
1.2 Renewable energy and hydrogen . . . . .	2
1.3 Electrolyser design improvements . . . . .	3
1.4 Shunt currents . . . . .	3
1.5 Project scope . . . . .	4
<b>2 Theory</b>	<b>5</b>
2.1 Alkaline water electrolysis . . . . .	5
2.1.1 Working principles of an electrolysis cell . . . . .	5
2.1.2 Thermodynamics . . . . .	6
2.1.3 Overpotentials and resistances . . . . .	8
2.2 Electrolyser Geometry . . . . .	9
2.2.1 Electrode spacing . . . . .	9
2.2.2 Cell configuration . . . . .	10
2.2.3 Electrode shape . . . . .	11
2.3 Shunt currents . . . . .	12
2.4 Reference Electrodes . . . . .	14
2.4.1 Pseudoreference Electrodes . . . . .	15
<b>3 Experimental setup and equipment</b>	<b>16</b>
3.1 Reference electrode validation setup . . . . .	16
3.2 Electrolyser stack design . . . . .	18
3.3 Nickel electrodes . . . . .	23
3.4 Magnetic current clamp measurements . . . . .	24
<b>4 Experimental results and analysis</b>	<b>25</b>
4.1 (Pseudo)reference electrode validation . . . . .	25
4.2 Electrochemical performance of the stack . . . . .	28
4.3 Shunt currents in a 5-cell alkaline water electrolysis stack . . . . .	29
4.3.1 Constant current and variable flow rate . . . . .	30
4.3.2 Constant flow rate and variable current . . . . .	38
4.4 Silver and copper wires as pseudoreference electrodes . . . . .	39
<b>5 Conclusions and Recommendations</b>	<b>40</b>
5.1 Conclusions . . . . .	40
5.2 Recommendations . . . . .	42
<b>References</b>	<b>43</b>
<b>A Electrochemical stability copper and silver</b>	<b>46</b>
<b>B Shunt currents</b>	<b>47</b>
<b>C Dimensions, resistances and void fractions</b>	<b>49</b>
C.1 Stack dimensions . . . . .	49
C.2 Stack resistances . . . . .	50
<b>D (Pseudo)reference electrodes results</b>	<b>54</b>
D.1 raw data reference electrodes . . . . .	55

---

<b>E</b>	<b>Images of the anode and cathode compartment at different flow rate regimes</b>	<b>56</b>
E.1	Constant gas flow rate: O <sub>2</sub> : 78 mL/min, H <sub>2</sub> : 157 mL/min . . . . .	56
E.1.1	Liquid flow rate regime: 0.596 - 47.68 mL/min . . . . .	56
E.2	Constant gas flow rate: O <sub>2</sub> : 39 mL/min, H <sub>2</sub> : 78 mL/min . . . . .	60
E.2.1	Liquid flow rate regime: 11.72 - 117.2 mL/min . . . . .	60
E.3	Constant liquid flow rate: 70 mL/min . . . . .	63
E.3.1	Gas flow rate regime: O <sub>2</sub> : 20 - 98 mL/min, H <sub>2</sub> : 39 - 196 mL/min . . . . .	63
<b>F</b>	<b>Potential difference measurements along the manifolds</b>	<b>67</b>
F.1	Constant current of 278 mA/cm <sup>2</sup> , variable flow rate: 0.596 - 47.68 mL/min . . . . .	67
F.2	Constant current of 139 mA/cm <sup>2</sup> , variable flow rate: 11.72 - 117.2 mL/min . . . . .	68
F.3	Constant current of 139 mA/cm <sup>2</sup> , variable flow rate: 68.4 - 475.8 mL/min . . . . .	70
F.4	Constant liquid flow rate of 70 mL/min per cel, variable current density: 69.4 - 347.2 mA/cm <sup>2</sup> . . . . .	71
<b>G</b>	<b>Shunt current vs void fraction</b>	<b>74</b>

# 1

## Introduction

### 1.1. Evolution of energy sources

Since the onset of the Industrial Revolution around 1800, western civilization has been shaping a world increasingly dependent on substantial energy consumption. Industries and critical infrastructure sectors have expanded significantly, progressively supporting larger populations. This expansion has led to a scenario where the consistent supply of substantial energy amounts became crucial. Until the latter half of the 20th century, the majority of this energy production stemmed from the combustion of fossil fuels, including coal, natural gas, and crude oil, with a minor contribution from traditional biomass and hydropower. The intensive use of fossil fuels for energy meant that these resources were being depleted at a rate millions of times faster than their natural replenishment rate. From the latter half of the 20th century onwards, the focus began to shift towards more sustainable energy production methods such as harnessing the power of the wind and the sun. [1]. Figure 1.1 visualizes the increase in energy consumption over the last 200 years, and shows by what source the energy was produced.

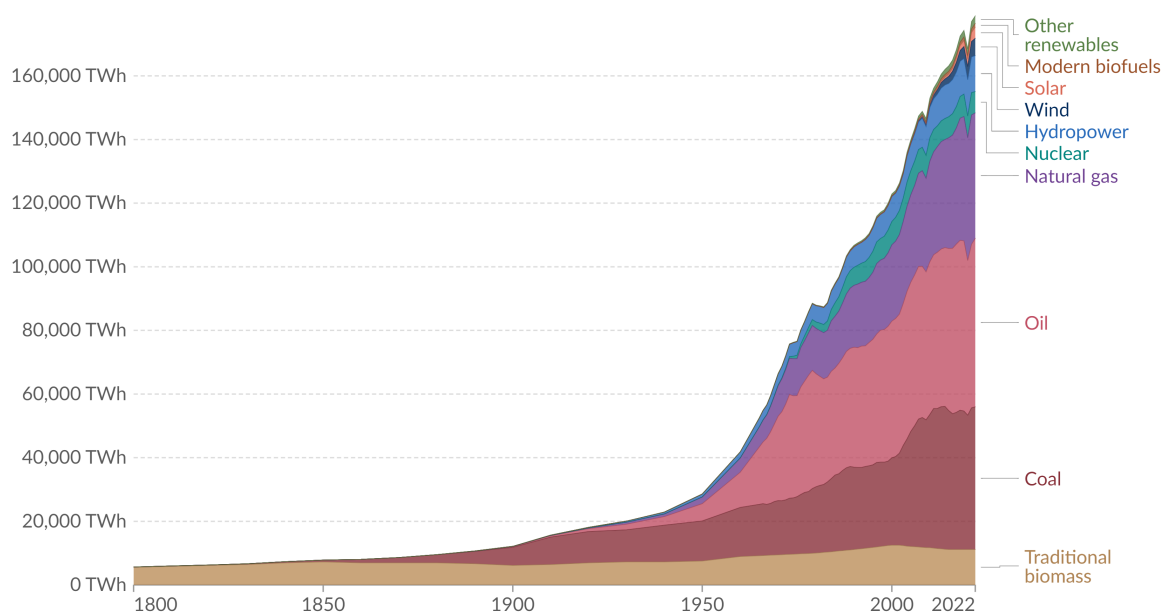


**Figure 1.1:** The global primary energy consumption by source, from the year 1800 till 2022. Retrieved from [1].

The burning of fossil fuels leads to the emissions of greenhouse gases, such as carbon dioxide. If too much of these gases are released into the atmosphere global temperatures rise, resulting in drastic changes of climate circumstances such as extreme drought, heavy rainfall and rising sea levels. The effects will differ per geographical location. If the continuous emitting of these greenhouse gases will not stop, everyone will be affected [2] [3]. Besides that, the fossil fuel sources will eventually run out, as they are depleted much quicker than they are

replenished. These are the main motivations behind the upcoming trend in renewable energy generation; these sources (e.g. the sun and the wind) will not run out and there are no greenhouse gases emitted in these processes of energy generation. Figure 1.2 shows the trends of global temperature and CO<sub>2</sub> levels in the atmosphere.

Yearly global surface temperature and atmospheric carbon dioxide (1850-2022)

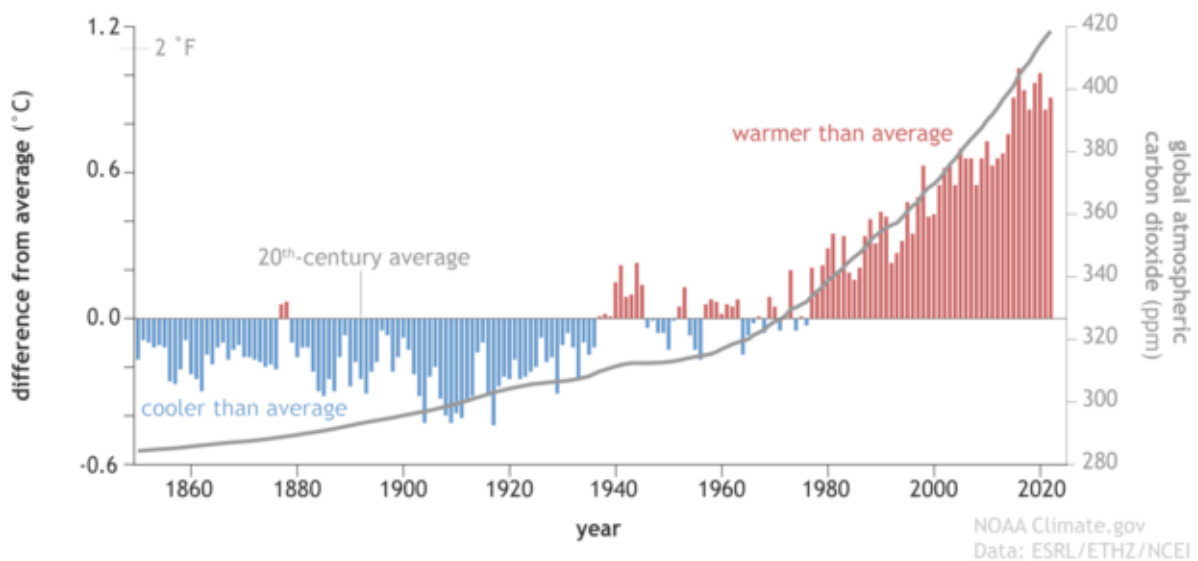


**Figure 1.2:** Yearly temperature compared to the twentieth-century average (red bars mean warmer than average, blue bars mean colder than average) from 1850–2022 and atmospheric carbon dioxide amounts (gray line). Retrieved from [4] with permission.

## 1.2. Renewable energy and hydrogen

The upcoming trend of electricity generation from solar and wind power means that there is a dependency on the unpredictable and intermittent behaviour of these energy sources. There is a clear seasonal pattern in the solar irradiation and wind power at many geographical locations, besides the obvious daily cycle. This results in periods where there is a surplus in electricity generated and in periods where there is a shortage. A surplus in electricity generation can put strain on the electricity distribution network. This leads to a growing demand for means to store large amounts of energy to relieve the electricity network in peak hours and meet the energy demand in shortage hours. Storing energy can be done in a variety of ways; electrochemical energy storage (batteries), mechanical energy storage, thermal energy storage, chemical energy storage (fuels) and more [5]. This paper will emphasize on an element of chemical energy storage through hydrogen.

Hydrogen is considered to be a promising energy carrier as it is a carbon-free chemical carrier. When there is excess power during the charging process, carbon-free or “green” hydrogen can be produced from water via electrolysis and stored in a storage tank. During peak hours, when power availability is limited, electricity is generated from stored hydrogen using fuel cells. An electrolyser uses electrolysis to break down water into hydrogen and oxygen. The oxygen is then released into the atmosphere, while the hydrogen is stored in a storage tank [5]. Hydrogen can be stored in multiple ways, which are not in the scope of this research. Hydrogen can be produced in multiple ways as well, many of which are not carbon-free; the vast majority of hydrogen is being produced by means of steam-methane reforming. As of 2019, renewable sources account for approximately 5% of the overall hydrogen production [6]. As the demand for hydrogen is expected to increase, so are carbon-free means of producing hydrogen.

Green hydrogen can be produced in a number of ways; water splitting by electrolysis (Alkaline water electrolysis (AWE), Solid Oxide Water Electrolysis, Proton Exchange Membranes (PEM) and Anion Exchange membranes) and hydrogen production via biomass. AWE and PEM are considered to be the most mature of these technologies [7]. AWE is a method that makes use of a highly alkaline medium and two non-platinum group metals and is seen as a technology that is reliable for hydrogen production up to the Mega-Watt scale [8],[9],[10]. Forecasts suggest that due to its affordability and the fact that it does not rely on rare materials, AWE technology has the potential to become a more prevalent choice for electrolyzer systems [7],[11]. However, there are some draw-

backs to this technology; generally AWE electrolysers operate at lower current densities, provides lower purity gas than competitors such as PEM, and there is a reduction in the electrolysers performance due to the formation of carbonates on the electrode [8]. To gain more insight in these shortcomings and to be able to overcome them, continuous research and development is required.

### 1.3. Electrolyser design improvements

In 2019, a novel electrolyser design was developed and patented by J.W. Haverkort [12] at the Process & Energy department of Delft University of Technology. The novelty of this design lies in the electrode architecture. Where usually large industrial scale electrolysers are formed by sandwiching flat electrode plates to form a stack of multiple cells, connecting these in series or in parallel, Haverkort et al. came up with a design containing hollow pillar-shaped anodes and cathodes arranged in a ‘checkerboard’ pattern. As all four sides of the flow channels are electrodes, this design takes up 1.5 to two times less volume when compared to the usual sandwich designs. An arrangement of corrugated electrode plates tilted 45 degrees is shown to be equivalent. J.W. Haverkort also came up with the idea that the anodes and cathodes alternate among two cells rather than alternating with each cell, as is usual. Less alternation between cells makes the process safer because the compartments carrying the produced gases are less exposed to each other [13]. Figure 1.3 displays the difference between a regular bipolar stack design and the new design of Haverkort et al. The research of this paper focuses on the design described in [12], and specifically on shunt currents in this design.

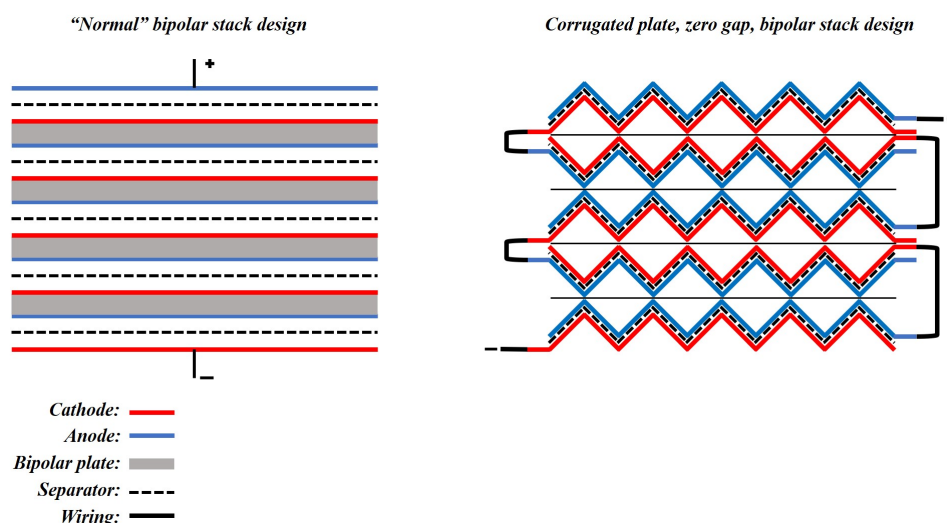


**Figure 1.3:** On the left: a regular bipolar electrolyser stack design that makes use of a bipolar plate in between anode and cathode. The anode and cathode alternate among each cell. On the right: The new corrugated plate, zero-gap, bipolar stack design. The anode and cathode alternate among two cells and the series connection is realized via external wiring. The flow direction is normal to the paper/screen.

### 1.4. Shunt currents

Electrolyzer stacks frequently encounter a problem known as shunt current, which is alternatively described as leakage, bypass, or parasitic current in various studies. Shunt current occurs when ionic flow diverts from its intended path across the diaphragm between cells and instead travels through the feed or exhaust manifold. This detour effectively bypasses the adjacent cells where the current is meant to be channeled. The root of this issue lies in the conductive nature of the electrolyte that circulates through these manifolds [14]. A simplified schematic drawing of a 5-cell stack with shunt currents along the conducting manifolds is shown in Figure 1.4.

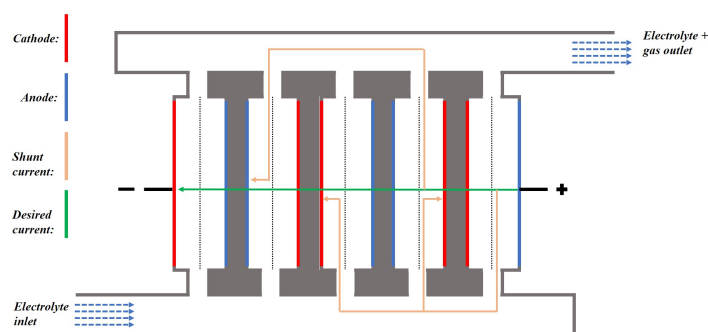


**Figure 1.4:** A schematic representation of shunt currents in a 5-cell electrolyser stack. Only on upper manifold is shown for the sake of simplicity.

## 1.5. Project scope

The scope of this Master thesis entails the realization of the design concepts elaborated in [12] and building of a 5-cell stack to performing measurements to identify and quantify shunt currents. That means building and designing a 5-cell, corrugated plate electrode, series connected alkaline water electrolyser stack. A first version of this design was already realized in a prior thesis, where a 1-cell electrolyser was built [13]. This design was ameliorated to overcome issues concerning leak tightness. The measurement of shunt currents in the connecting manifolds of the stack is done with the use of hydrogen reference electrodes and copper and silver pseudoreference electrodes as well as a magnetic current clamp meter. These reference electrodes can measure potential differences, combined with the Ohmic resistance of a pathway the current can be inferred. The employment of reference electrodes in this context is not how they are commonly used, so additional research is performed to validate and calibrate the usage of reference electrodes to measure small potential differences in alkaline electrolyte. The same research will be conducted on the usage of copper or silver wires to measure potential differences in the highly alkaline environment of a AWE. The usage of the magnetic current clamp meter to measure shunt currents was possible due to the stack design with external wiring. The external wire connections between the electrodes, as seen on the right side of Figure 1.3, were able to be enclosed by a magnetic current clamp. The thesis focuses specifically on the following research questions:

### Research questions

1. Can hydrogen reference electrodes and pseudoreference electrodes like silver or copper wires be used to accurately measure potential differences in an alkaline electrolysis cell? If yes, which is most accurate?
2. Can hydrogen reference electrodes and pseudoreference electrodes like silver or copper wires be used to accurately measure the electrolyte potentials in the manifolds of a 5-cell electrolyser stack, If yes, can shunt currents be accurately inferred from those measurements?
3. Can a magnetic current clamp enclosed around the external wiring be used to accurately measure shunt currents in a 5-cell electrolyser stack with external wiring?
4. What is the influence of varying the current in an electrolyser stack on shunt currents?
5. What is the influence of electrolyte flow rate variations in an electrolyser stack on shunt currents?

Measuring shunt currents in actual stacks is often a challenge due to design constraints. The first three research questions aim to assess different measurement techniques and provide clarity on their applicability in this type of electrolyser stack. The relationship between electrolyte flow rate, applied current and shunt current is not a universal one. The actual impact of these parameters can vary based on system design, operating conditions, and electrolyte characteristics. The last two research questions are meant to provide clarity on these effects for this stack design.

# 2

## Theory

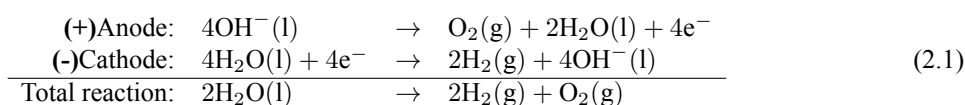
This purpose of this chapter is to provide a theoretical summary of the relevant topics concerning alkaline water electrolysis in stack designs. The fundamental thermodynamical and electrochemical processes taking place are discussed in Section 2.1. The different effects electrolyser geometry has on the working principles of industrial alkaline water electrolysis is described in Section 2.2. Section 2.3 provides an understanding of the existence and modelling of shunt currents in electrochemical stack designs. Lastly, the relevance and electrochemical behaviour of reference and pseudoreference electrodes is concisely discussed in Section 2.4.

### 2.1. Alkaline water electrolysis

The splitting of water into hydrogen and oxygen by means of electricity is called electrolysis. This process has been discovered by accident by in the year 1789. In that year, two Dutchmen from Amsterdam immersed two gold wires connected to a friction-based electrostatic generator in a glass tube filled with water. The water decomposed to hydrogen and oxygen on the gold electrodes. By 1800, the first battery was used for the electrolytic splitting of water. When the water is switched for an alkaline solution, the process is called Alkaline Water Electrolysis (AWE). AWE has garnered renewed vigor over the last years as an alternative to steam methane reforming for hydrogen production. This is largely driven by the potential to reduce environmental effect, satisfy distributed demand and reduce hydrogen cost. Renewable sources contribute about 5% of the total hydrogen production as of 2019 [6]. The following section gives a basic understanding of the working principles of alkaline water electrolysis.

#### 2.1.1. Working principles of an electrolysis cell

An alkaline water electrolyser typically consists of the following parts: two electrodes (anode and cathode) connected to a power supply, an electrolyte solution and a separator (membrane or diaphragm). These parts are schematically portrayed in Figure 2.1. The principle underlying alkaline water electrolysis is rather straightforward. When a direct current is applied to two electrodes immersed in a chemical solution (electrolyte), the process facilitates the separation of oxygen and hydrogen, as depicted in Equation (2.1). Due to the applied potential difference from the power source, electrons are forced to move from the anode to the cathode. At the cathode, these electrons reduce  $\text{H}_2\text{O}$  to  $\text{H}_2$  (hydrogen gas) and  $\text{OH}^-$ . Due to the presence of the electric field,  $\text{OH}^-$  molecules migrate from cathode to anode. At the anode,  $\text{OH}^-$  is oxidized to form  $\text{O}_2$  and  $\text{H}_2\text{O}$ . The electrons released during this oxidation reaction travel through the external wiring to the cathode, where they reduce water again. As long as the applied potential is above a certain threshold value, electrolysis will continue. The hydrogen and oxygen is released in the form of bubbles and ascends due to their buoyancy. These gases can be captured outside of the cell, delivering pure hydrogen at the cathode side and pure oxygen at the anode side.



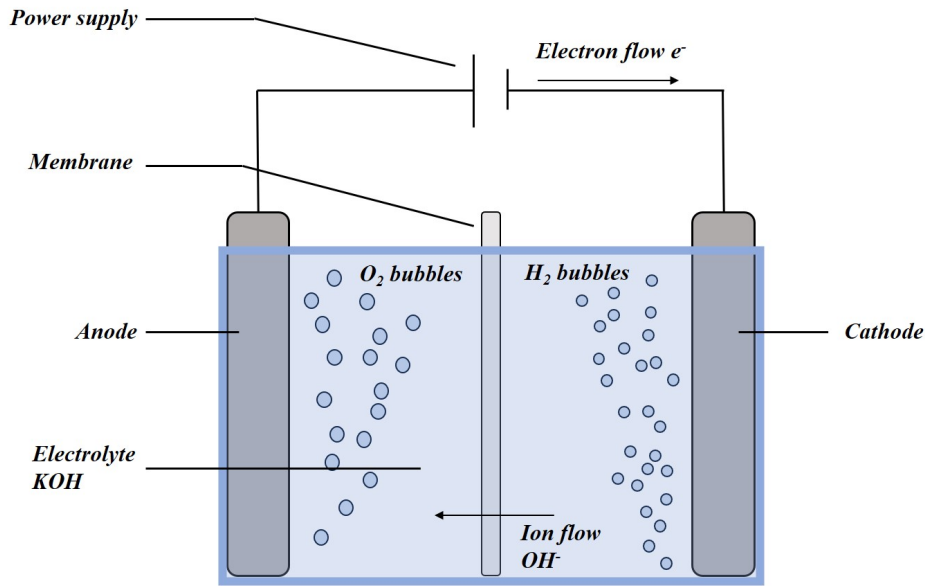


Figure 2.1: Schematic overview of the alkaline water electrolyzer.

The solution through which the ions travel and wherein the electrodes are placed is called the electrolyte. In the case of AWE this is typically a 30 wt% KOH solution, due to its high ionic conductivity. In between the two electrodes resides a separator or diaphragm that prevents the produced gases (hydrogen and oxygen) to mix but allows for ionic transport. In some instances, dissolved gases may also permeate through a separator; however, a predominant fraction of gases manifests in the form of bubbles, which exhibit negligible diffusive properties through such barriers [15]. In Figure 2.1, a membrane is used as a separator. The main reasons why gas mixing in the form of bubbles should be avoided are: (i) Hydrogen gas has to reach very high purity ( $> 99\%$ ) for most industrial applications [6] (ii) to maintain chemical stability or safety (e.g., explosive  $H_2/O_2$  gas mixtures may be avoided); (iii) the separator may prevent physical contact between the anode and cathode if the electrodes are closely spaced [16]. This close spacing of the electrodes is done in an effort to reduce ohmic losses. This is called a “zero gap” configuration and will be elaborated on in Section 2.2.1.

Typical electrode materials used as cathodes for the hydrogen evolution reaction are steel, stainless steel, high-area Ni on steel and Ni. Those used as anodes for the oxygen evolution reaction are Ni oxides, and Ni- and Co-based spinels, e.g.,  $NiCo_2O_4$  on Ti [16]. Membranes are usually made from polymer materials, non-woven fabrics or a combination of different materials. The choice of material depends on factors like the operating conditions of the electrolyzer (temperature, pressure), mechanical strength, longevity, and resistance to the corrosive alkaline environment [17].

When multiple electrochemical cells like the one in Figure 2.1 are connected to each other in parallel or in series, we speak of a “stack”. Stacks are used for large scale industrial hydrogen production.

### 2.1.2. Thermodynamics

As mentioned in Section 2.1.1, electrolysis requires an energy input to take place. The required energy for electrolysis to occur is given by the enthalpy. The enthalpy change ( $\Delta H$ ) initiates the electrolysis reaction at constant temperature and pressure and consists out of a Gibbs free energy part and a thermal energy part. The Gibbs energy ( $\Delta G$ ) is the electrical part of it and the remaining part is thermal energy ( $Q$ ) which equals the multiplication of the process temperature ( $T$ ) and the entropy change ( $\Delta S$ ). This is given by the following expression:

$$\Delta H = \Delta G + T\Delta S \quad (2.2)$$

The Gibbs energy can be written by the following equation [18]:

$$V_{\text{rev}} = -\frac{\Delta G}{zF} \quad (2.3)$$

Where  $z$  is the number of transferred electrons ( $z=2$ ) and  $F$  is the Faraday constant (96485 C/mol) [19].  $V_{\text{rev}}$  is the reversible cell voltage, and considered to be the minimum required potential for electrolysis to occurs.

If the thermal energy ( $T\Delta S$ ) is provided by electricity, the minimum voltage required to start electrolysis is denoted by the thermoneutral voltage ( $V_{\text{tn}}$ ). Because the total energy required is the same as the change in enthalpy during the (ideal) process, the thermoneutral voltage can be calculated according:

$$V_{\text{tn}} = \frac{\Delta H}{zF} \quad (2.4)$$

In the case of standard pressure and temperature conditions ( $T=298.5\text{K}$ ,  $P=1\text{ bar}$ ) the standard Gibbs free energy ( $\Delta G_0$ ) equals 237.2 kJ/mol and the standard enthalpy ( $\Delta H_0$ ) equals 285.84 kJ/mol. When these values are used in Equations (2.3) and (2.4) the following values for the standard equilibrium potential and the thermoneutral potential are retrieved:

$$V_{\text{rev}}^0 = -1.229\text{V} \quad (2.5)$$

$$V_{\text{tn}}^0 = -1.481\text{V} \quad (2.6)$$

These numbers can be interpreted according to the following: when applying only  $\Delta G_0 = 237.2\text{ kJ/mol}$  (or  $-1.229\text{ V}$ ), heat is extracted from the environment in order to keep the reaction going. In order to compensate for this heat extraction, one needs to apply 285.84 kJ/mol ( $-1.481\text{ V}$ ). This sustains the reaction. The relation between the enthalpy, gibbs free energy and the heat demand in the temperature range of 0-1000 °C is shown in Figure 2.2a. The behaviour of reversible and thermoneutral voltage in the temperature range of 0-1000 °C can be seen in Figure 2.2b.

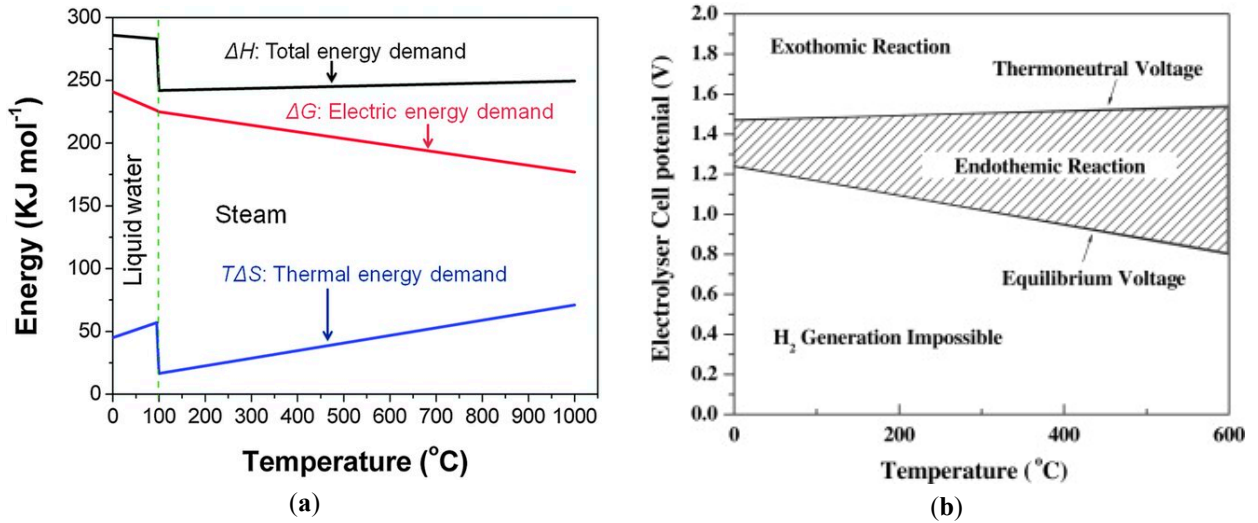


**Figure 2.2:** (a): Total, thermal and electrical energy demand of an ideal electrolysis process as function of the temperature. Retrieved with permission from [20]. (b): Cell potential as a function of temperature. Retrieved with permission from [21].

What can be seen in Figure 2.2a is that as the temperature increases, the thermal energy demand  $\Delta Q$  increases. Simultaneously, the electrical energy demand  $\Delta G$  decreases. This can be interpreted as an increase in electrical efficiency at elevated temperatures. However, an external heat source is required to achieve this. Figure 2.2b shows that the reaction requires a heat input in the range between the equilibrium voltage and the thermoneutral voltage, and is thus endothermic. Above the thermoneutral voltage the reaction becomes exothermic.

The reversible potential, or equilibrium potential, to be applied can be calculated with the Nernst equation, given below.

$$V_{\text{rev}} = V_{\text{rev}}^0 - \frac{R_g T}{2F} \ln \left( \frac{P_{\text{H}_2} P_{\text{O}_2}^{0.5}}{P_{\text{H}_2\text{O}}} \right) \quad (2.7)$$

Where  $V_{\text{rev}}^0$  is the standard equilibrium potential again,  $R_g$  is the gas constant ( $R=8.314 \text{ J/mol.K}$ ),  $T$  the absolute temperature and  $P_{H_2}$ ,  $P_{H_2O}$  and  $P_{O_2}$  are the partial pressures of the molecular species. Actually the Nernst equation should be expressed in activity instead of partial pressure. Activity in this context is a measure of the ‘effective’ concentration. However, since activity coefficients are often unknown in aqueous and non-aqueous electrolytes, it is accepted to approximate it with concentration or partial pressure of the reactants and products at low concentrations [22].

### 2.1.3. Overpotentials and resistances

$V_{\text{rev}}$  is the theoretical equilibrium potential, actual cell voltage needed to continue the reaction is higher with the addition of ohmic loss of the electrolyte and separator and overpotential due to electrode kinetics [6]. The actual cell potential can be written as the sum of the reversible potential and overpotentials [18]:

$$V_{\text{cell}} = V_{\text{rev}} + \eta_{\text{act,a}} + |\eta_{\text{act,c}}| + \eta_{\text{ohm}} \quad (2.8)$$

The total overpotential can be expressed as:

$$\eta_{\text{tot}} = V_{\text{cell}} - V_{\text{rev}} = \eta_{\text{act,a}} + |\eta_{\text{act,c}}| + \eta_{\text{ohm}} \quad (2.9)$$

Where  $\eta_{\text{act,a}}$  and  $\eta_{\text{act,c}}$  are the activation potentials at the anode and cathode electrodes, respectively (by definition, the cathodic overpotential is negative in sign) [23] and  $\eta_{\text{ohm}}$  represents the ohmic losses in the system caused by the electrolyte and separator. The activation losses on the anode and cathode side,  $\eta_{\text{act,a}}$  and  $\eta_{\text{act,c}}$ , are calculated through the following equations:

$$\eta_{\text{act}} = \eta_{\text{act,a}} + \eta_{\text{act,c}} = \frac{R_g T}{\alpha_a n F} \ln \left( \frac{j}{j_{0,a}} \right) + \frac{R_g T}{\alpha_c n F} \ln \left( \frac{j}{j_{0,c}} \right) \quad (2.10)$$

This equation is called the Tafel Equation. Where  $\alpha_a$ ,  $\alpha_c$ ,  $j_{0,a}$ , and  $j_{0,c}$  are charge transfer coefficients and exchange current densities for anode and cathode, respectively.  $R_g$  is again the gas constant and  $T$  the temperature. Exchange current density,  $j_0$ , strongly depends on the electrode structure such as materials and roughness [18]. This equation can be simplified to the following expression:

$$\eta_{\text{act}} = b \ln \left( \frac{j}{j_0} \right) \quad (2.11)$$

Which result in the following total overpotential term:

$$\eta_{\text{tot}} = b \ln \left( \frac{j}{j_0} \right) + jAR \quad (2.12)$$

Here  $jAR$  is a multiplication of the applied current density ( $j$ ), the electrode area ( $A$ ) and the ohmic resistance ( $R$ ). This term describes the ohmic overpotential previously expressed as  $\eta_{\text{ohm}}$ .

Figure 2.3 shows how the magnitude of the contributions to cell voltage vary with current density. With increasing current densities the contribution from ohmic losses becomes more prominent, becoming the dominant factor at high values. The overpotential at the anode can be seen to be greater than that at the cathode.

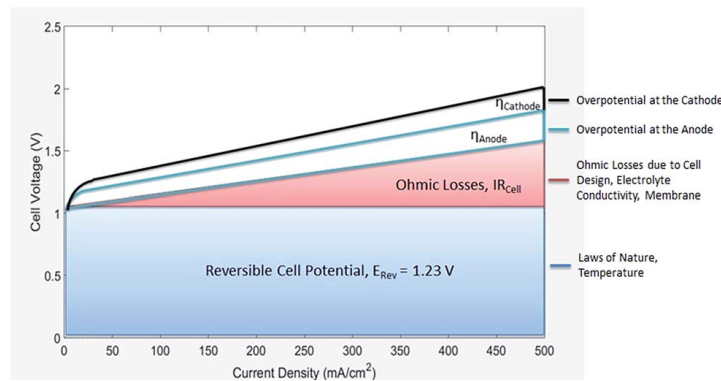


**Figure 2.3:** Graph showing the individual contributions to cell voltage, this allows each contribution to be targeted individually, allowing a systematic approach to reducing the cell voltage. Retrieved from [24] with permission.

The ohmic losses cannot be calculated solely on the basis of Ohms law, that is, it is not possible to calculate it from the solution conductivity, the distance of the electrodes, and their surface area. This is due to the presence of bubbles from the evolving gases decreasing the active cross section of the electrolyte solution as a current conducting medium [23]. However, when the resistances of the successive components are known, a good estimation of the ohmic losses can be performed. The total cell resistance can be approximated by a sum of the following resistance components:

$$R_{\text{cell}} = R_{\text{circuit}} + R_{\text{electrolyte}} + R_{\text{bubbles}} + R_{\text{membrane}} \quad (2.13)$$

Where  $R_{\text{circuit}}$  contains the resistance of the wiring, the anode and cathode.  $R_{\text{electrolyte}}$  and  $R_{\text{membrane}}$  are dependent on the solution and material used. These can be retrieved from data sheets, literature or by experimental validation. In the case of a stack of cells, the resistance of the bubbles is often accounted for by adding a void factor in the resistance calculation of a certain ionic pathway, this is elaborated on in Section 2.3.

## 2.2. Electrolyser Geometry

The design of electrolyzer stacks extends beyond their electrochemical properties, encompassing geometric attributes that significantly impact operational outcomes. This section takes a closer look at how factors like electrode spacing and shape, the choice between bipolar and monopolar designs, and the arrangement of cells in series or parallel, can influence the behavior of electrolysis processes.

### 2.2.1. Electrode spacing

When compared to electrolysis in acidic or neutral environments, alkaline conditions allow for the use of cheaper earth abundant metals as electrodes, but generally operate at a lower efficiency, requiring larger devices and thus higher costs. So how could the efficiency of alkaline electrolysis be maximized? One answer lies in the distance between the electrodes, which is the topic discussed in this sub section.

As is visible in Equation (2.13), the total cell resistance depends on the added resistances of multiple components, including the membrane and the electrolyte. According to the general formula for resistance, visible in Equation (2.14), where  $\rho$  is the resistivity of the conducting medium,  $L$  is the distance travelled and  $A$  is the cross sectional area of the medium, the distance travelled by the current through the electrolyte is linearly proportional to the resistance. This suggests that minimizing the distance would minimize the resistance component of the electrolyte, thus increasing the overall efficiency.

$$R = \frac{\rho L}{A} \quad (2.14)$$

By compressing two porous electrodes on either side of a hydroxide ion conducting membrane or gas separator the electrode spacing is minimized. This is called the "zero gap" design. Figure 2.4 shows that the main difference between the traditional setup and the zero gap design is the employment of porous electrodes rather than solid metal plates. This allows cells with a very small inter-electrode gap, compact design and high efficiency. It forces gas bubbles to be released from the backside of the electrodes, reducing their contribution to the cell voltage [24].

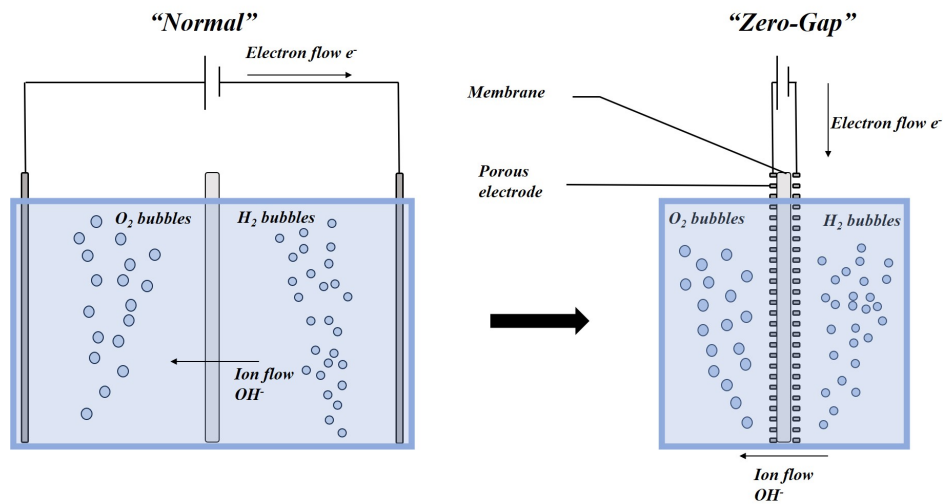


**Figure 2.4:** On the left the “Normal” setup. On the right the “zero gap” setup showing the principal differences in design. Porous electrodes are pressed either side of the membrane to reduce the inter-electrode gap, and a conducting gas diffusion layer provides an electrical connecting from the electrodes to the bipolar current collector.

### 2.2.2. Cell configuration

Regarding cell configuration, an electrolyser can be either unipolar (i.e. monopolar) or bipolar. This polarity refers to the manner in which the electrodes are electrically connected to each other.

The concept of unipolarity entails that electrodes of equal polarity are all coupled together in parallel. This results in a stack with alternating positive and negative electrodes, separated by a porous separator. A plant-scale electrolyzer is then built up by connecting these stacks electrically in series. The total voltage applied to the whole stack is the same as that applied to an individual cell [16]. The voltage of the entire plant is then the added voltages of the stacks in series. The main disadvantage of the much simpler monopolar design is the conductive requirement on the electrodes and current collectors, since current has to be transported out of each cell separately in the transverse direction. Since often a lower current at a higher voltage is preferred to reduce ohmic losses in electrical wiring, additional voltage conversion is typically required.

On the other hand, in a bipolar electrolyzer, a metal sheet (also known as a “bipolar plate”) acts as a connector between neighboring cells in an electrical series. As shown in Figure 2.5b, the electrocatalyst for the negative electrode is applied to one side of the bipole, while the positive electrode’s electrocatalyst for the adjacent cell is applied to the opposite side. This setup means that the total stack voltage is the sum of the individual cell voltages. Consequently, a stack of these cells connected in series forms a module that operates at a higher voltage and lower current compared to the unipolar design. To meet the requirements of a large-scale electrolysis plant, these modules are connected in parallel to increase the overall current output [16].

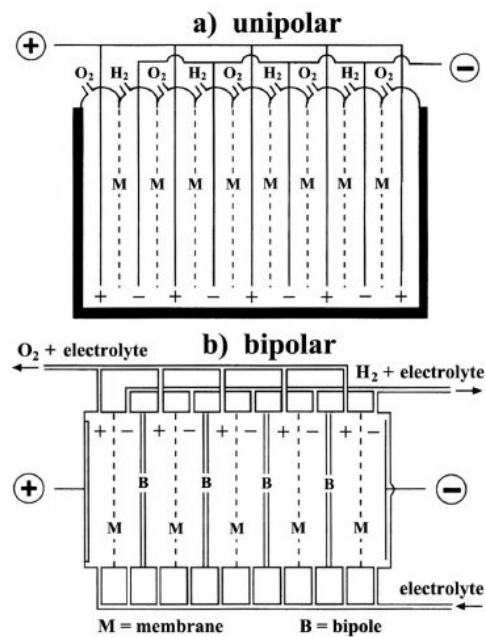


**Figure 2.5:** Electrolyzer modules with a) unipolar and b) bipolar cell configurations. Retrieved from [16] with permission.

An advantage of the bipolar design is a reduction in ohmic losses, due to lower currents needed to operate the stack. A disadvantage is that it poses design restrictions to counteract shunt currents, or bypass currents. These shunt currents reduce the electrical efficiency of electrolyser stacks and will be discussed in Section 2.3. Another disadvantage is the production of oxygen and hydrogen close together, requiring additional space and material costs to ensure separation. As you can see in Figure 2.5, the electrodes are ordered in alternating fashion (ACA-CACAC...) for both unipolar and bipolar arrangements. A different approach to this is discussed in the following section.

### 2.2.3. Electrode shape

While the majority of research considering alkaline water electrolysis focusses on advancing catalysts and appropriate electrode materials, there is notably less emphasis on exploring cell and electrode configurations. An exception is found in [12], where an alternative compact electrode architecture with hollow pillar-shaped anodes and cathodes arranged in a ‘checkerboard’ pattern is analysed and shown to be equivalent to a particular arrangement of corrugated plate electrodes. It is estimated that with this design, a volumetric energy density gain of 1.5 to two times can be obtained, when compared to regular flat electrodes. A schematic overview of the corrugated electrode design is displayed in Figure 2.6.

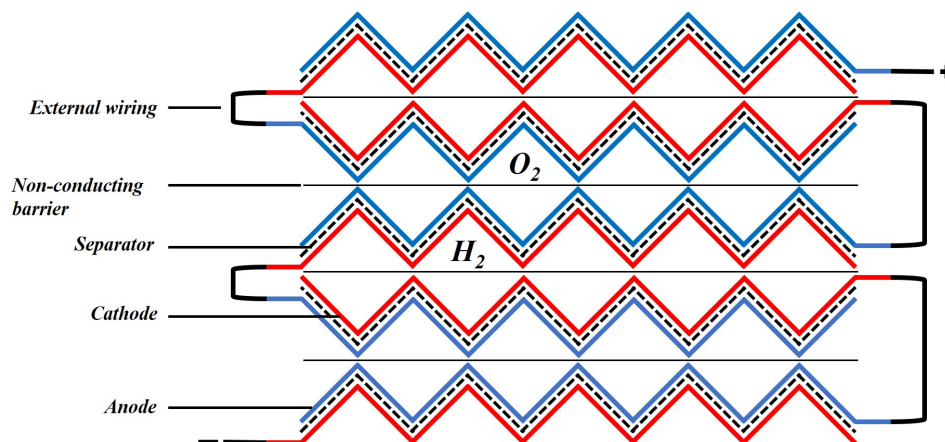


**Figure 2.6:** A corrugated electrode and membrane configuration. The flow direction is normal to the paper/screen. In between two of the same electrodes resides a non-conducting barrier to prevent parasitic shunt currents between these electrodes.

As mentioned in the previous section, this electrode arrangement differs from the usual alternating topology (ACACACACAC) and orders the electrodes such that cathodes face cathodes and anodes face anodes (ACCAAC-CAAC). The alteration in topology achieved by connecting adjacent electrodes of identical polarity offers notable advantages in manufacturing simplification, while also enabling current extraction from the sides. It also means that there is no need for bipolar plates in between the electrodes. In regular designs, bipolar plates have a risk of corroding which can lead to the mixing of gases. Removing the bipolar plates ensures that oxygen and hydrogen have no chance of mixing, reducing the risk of explosion.

## 2.3. Shunt currents

An efficiency limiting phenomena occurs in bipolar electrolyser stacks referred to as shunt currents, or bypass currents. These currents bypass the electrolysis contributing direction and flow through the inlet and outlet channels of the electrolyte and produced gases (oxygen and hydrogen). These currents can propagate between different cells along these channels and bypass cells in between, not contributing to electrolysis as they potentially could. An image portraying shunt currents can be seen in Figure 2.7.

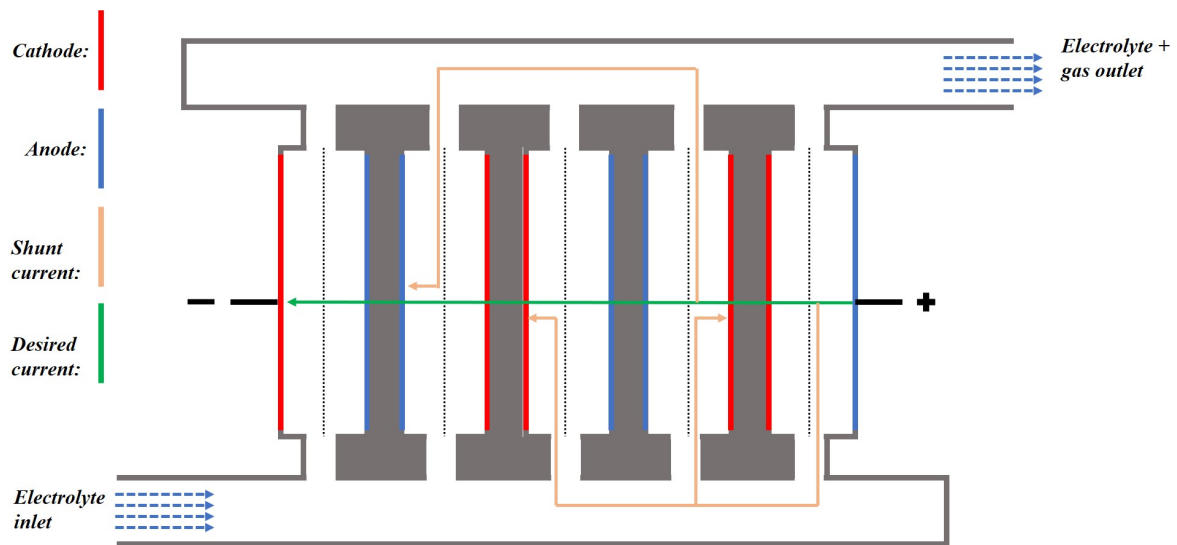


**Figure 2.7:** A schematic representation of shunt currents in a 5-cell electrolyser stack. Only one upper manifold is shown for the sake of simplicity. Same as Figure 1.4.

As long as there is a conductive pathway through the inlet/outlet channels and manifolds between the cells, these currents can occur. Increasing the resistance of these pathways by making the dimensions narrower will lead to lower shunt currents, but also higher pressure drops [25]. The following section describes models of how these shunt currents can be approximated and predicted.

A commonly used method to approximate shunt currents is the equivalent circuit model (ECM) (e.g. [25], [26], [27], [14]). This method calculates the shunt resistance according to the structure of the flow channels and the conductivity of the electrolyte. An electrolyser stack is then modelled as an electrical network with constant resistances and power sources. A typical structure of how a 3-cell electrolyser stack is modeled according to the ECM is shown in Figure 2.8.

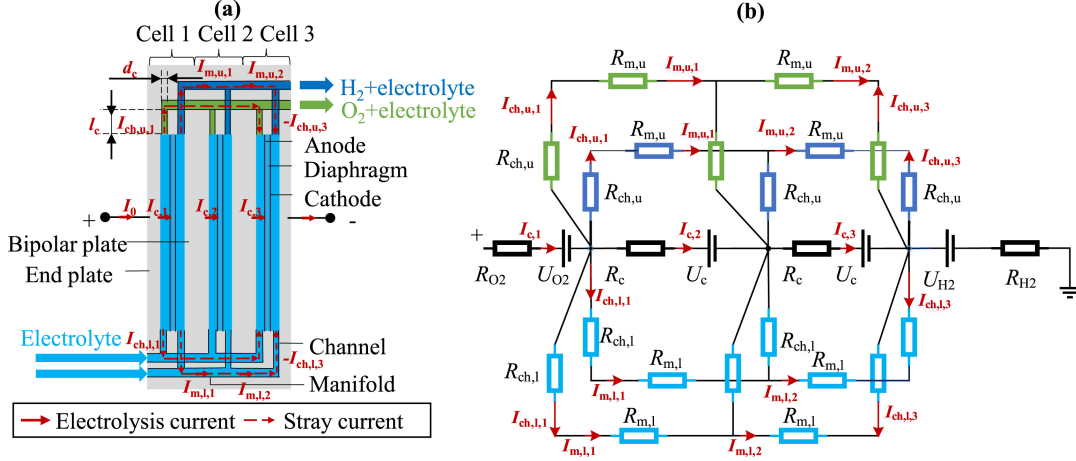


**Figure 2.8:** Schematic diagram (a) and equivalent circuit (b) of a 3-cell alkaline electrolysis stack. Retrieved from [25] with permission.

The cells are of zero-gap configuration with the electrodes and diaphragm in close contact. Each two adjacent cells are electrically connected in series through a shared metallic bipolar plate. There is one manifold for the electrolyte inlet of positive and negative half side each, and every single cell is supplied by the manifolds via channels drilled into the frame of each cell. For the outlet manifold, we assume the same situation, so in total it is expected to have four manifolds for the whole stack, and four channels for each cell.  $R_c$  and  $U_c$  are the internal resistance and potential of a single cell.  $R_{ch}$  and  $R_m$  represent the resistance in the channels and manifold, calculated using the respective dimensions and the electrolyte conductivity along Equation (2.14). The subscripts u and l represent the upper and lower channels or manifolds. The increase of resistance due to the bubbles present is accounted for by the Bruggeman Equation (2.15), that includes a factor to account for the void fraction in the channels and manifolds  $\alpha_{ch/m}$ . The Bruggeman equations can be used to model the effective electrical conductivity of the heterogeneous mixture. The Bruggeman correlation provides a way to estimate the effective conductivity of the mixture based on the volume fraction and properties of each phase. Bruggeman considered a process of embedding two different phases in a sample and based his reasoning on these assumptions [28]:

- The sample consists of two homogeneous and isotropic phases.
- Each phase consists of particles that are small in comparison to the sample size.
- Each phase is randomly distributed in the sample.

The void fraction is estimated as the percentage of the gas flow rate in the total flow rate, as seen in Equation (2.16).

$$R_{\text{actual}} = R * (1 - \alpha_{ch/m})^{-1.5} \quad (2.15)$$

$$\alpha_{ch/m} = \frac{q_g}{q_g + q_{liq}} \quad (2.16)$$

Here  $q_g$  and  $q_{liq}$  are the gas and liquid flow rate, estimated by Equations (2.17) and (2.18):

$$\bar{q}_2 = \bar{q}_{H_2} + \bar{q}_{O_2} = \left( \frac{I_0}{2\mathcal{F}} + \frac{I_0}{4\mathcal{F}} \right) \frac{R_g T}{P_0} \quad (2.17)$$

$$q_{liq} = \frac{q_0}{n} \quad (2.18)$$

In which  $I_0$  is the current input of the stack,  $T$  and  $p_0$  are the stack temperature and pressure respectively. In Equation (2.18)  $n$  represents the number of cells in the stack.

The current distribution in the stack can be calculated with Kirchoff's current law and Kirchoff's voltage law and boundary conditions, presented in Equations (2.19), (2.20) and 2.21 [25], respectively. This model can be sized up to accommodate calculations for larger stacks.

$$\begin{aligned}
I_{c,k+1} + 2I_{ch,u,k} + 2I_{ch,1,k} &= I_{c,k}, \quad k = 1, 2, \dots, n \\
I_{m,u,k+1} &= I_{m,u,k} + I_{ch,u,k+1}, \quad k = 1, 2, \dots, n-2 \\
I_{m,1,k+1} &= I_{m,1,k} + I_{ch,1,k+1}, \quad k = 1, 2, \dots, n-2
\end{aligned} \tag{2.19}$$

$$\begin{aligned}
R_{ch,u}I_{ch,u,k} + R_{m,u}I_{m,u,k} - R_{ch,u}I_{ch,u,k+1} &= R_c I_{c,k+1} + U_c, \quad k = 1, 2, \dots, n-1 \\
R_{ch,1}I_{ch,1,k} + R_{m,1}I_{m,1,k} - R_{ch,1}I_{ch,1,k+1} &= R_c I_{c,k+1} + U_c, \quad k = 1, 2, \dots, n-1
\end{aligned} \tag{2.20}$$

$$\begin{aligned}
I_{c,1} &= I_0 \\
I_{ch,u,1} &= I_{m,u,1}, \quad I_{ch,1,1} = I_{m,1,1} \\
I_{m,u,n-1} + I_{ch,u,n} &= 0, \quad I_{m,1,n-1} + I_{ch,1,n} = 0.
\end{aligned} \tag{2.21}$$

A similar approach is handled in [29], where an electrical analog for a typical electrochemical stack is constructed, similar to the one described above, and used to estimate a bypass current ratio. In this approximation, the ratio of the electrical resistance through the electrochemical cell to the electrical resistance of the bypass conductive path is considered to be proportionate to the total shunt current. Also, the resistances of the inlet and outlet channels are much larger when compared to the resistances of the manifolds, making them negligible. This ratio is expressed as  $\beta$  and defined according to Equation (2.22):

$$\beta = \frac{V_C}{I_0} * \left( \frac{1}{R_I} + \frac{1}{R_E} \right) \tag{2.22}$$

Where  $V_C$  is the cell voltage minus the ohmic drop over the diaphragm,  $I_0$  is the current running through the cell,  $R_I$  and  $R_E$  are the resistances of the inlet and exit channels of the electrochemical cell. After simplifying and working out the electrical scheme of a stack with  $N$  cells, the following expression for the bypass current ratio,  $\psi$ , emerges:

$$\psi = \frac{\beta}{12} (N^2 - 1) \tag{2.23}$$

This current bypass ratio gives the fraction of the total input current which bypasses the electrodes in a cell assembly.

Most of these papers are in agreement that the ionic shunt current, the current flowing in an inlet or outlet manifold through the channels, is S-shaped when plotted against cell number. Meaning that the current is highest at one end of the stack, decreases to a value of zero at the channels in the centre of the stack and then increases once more but in the opposite direction at the other end of the stack. The total leakage current, that is the shortfall of between applied current to the stack and the current applied to the cells, is smallest at the outermost cells and highest at the centre. This means that the magnitude of the current leaking out of the cells through the channels is different from the current running through the manifold [14]. This is visualized in Figure 2.9.

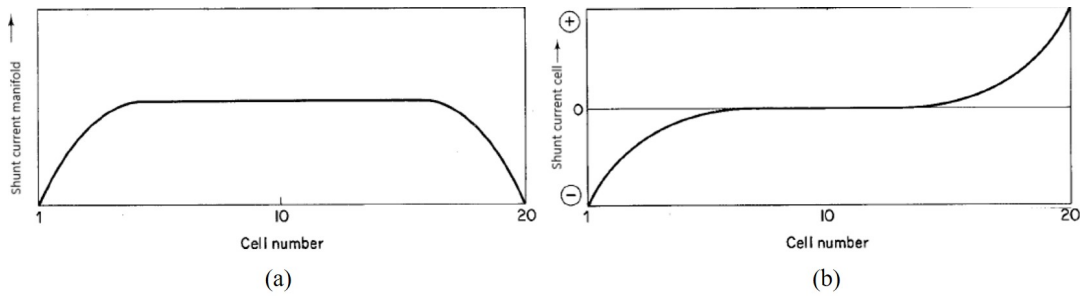


**Figure 2.9:** Schematic representation of the shunt currents flowing through the manifolds (a) and the inlet/outlet channels (b) in an electrolyzer stack consisting of 20 cells. Retrieved from [14] with permission.

## 2.4. Reference Electrodes

To facilitate the measuring of shunt currents a common approach is the use of reference electrodes. These reference electrodes serve two crucial purposes: First, they enable the control of the potential at a working electrode. Second, they allow for the measurement of the potential at an indicator electrode in relation to the reference electrode [30]. This section describes the working principles of reference electrodes and pseudoreference, or

quasi-reference, electrodes in electrochemical systems and explains the relevance in the context of shunt currents.

A reference electrode is an electrode with a consistent and well known electrode potential. In a cell, the entire chemical process consists of two distinct half-reactions that depict the chemical transformations at the two electrodes. To focus on the reaction happening at the working electrode, the reference electrode is standardized with constant (buffered or saturated) concentrations of each participant of the redox reaction [31]. When electric current flows through an electrochemical cell, it's important that the potential of one of the electrodes, specifically the reference electrode, remains nearly constant. This stability is essential for obtaining a well-defined value for the electrode potential of the electrode or solution you're studying or monitoring. The choice and design of the reference electrode depend on various experimental and technical factors. These factors include the magnitude of the applied current, the characteristics and composition of the electrolyte (such as whether it's an aqueous solution, nonaqueous solution, or a molten substance), the pH of the electrolyte and the temperature conditions [30].

In the case of a shunt current that exists in a lower or upper manifold of an electrolyser stack, the current exists due to a difference in potential between separate points of that channel. Measuring these potential differences with the use of reference electrodes or pseudoreference electrodes (see Section 2.4.1) and dividing by the calculated ohmic resistance of that channel section allows for the calculation of the magnitude of the shunt current in that section. In this scenario, two reference electrodes are used to measure a potential difference in the space between them. Because the reference electrodes have the same fixed redox potential, any potential difference measured between them is the result of a current and resistance in the space between them ( $U = IR$ ). In the scenario that there is no current running, the potential difference should be zero. However, because the redox potentials of two of the same reference electrodes is not exactly the same, a calibration measurement with no applied current always has to be performed. In the case of pseudoreference electrodes this process is less straightforward. The next section will provide an explanation for the difference between pseudoreference and actual reference electrodes.

### 2.4.1. Pseudoreference Electrodes

In some cases where it is not possible to use actual reference electrodes, e.g. because of design constrictions or because of difficulty in finding a reference electrode for a non-aqueous solvent that does not contaminate the test solution, a pseudoreference (or quasireference) electrode is employed. The essential difference between a true reference electrode and a pseudoreference electrode is the lack of thermodynamic equilibrium in the latter case.

In many cases simply platinum, silver or copper wires serve as pseudo- or quasi-reference electrodes with the assumption that the potential of this wire, although unknown, will not change during a series of measurements. This assumption should always be validated in a controlled environment with similar environmental conditions. The actual potential of the quasireference electrode vs. a true reference electrode must be calibrated before reporting potentials with reference to the SHE (0 V by definition).

The use of pseudo-reference electrodes offers certain advantages. They are known for their simplicity and are directly submerged in the electrolyte within the cell. This leads to minimal ohmic resistance (impedance), eliminates the occurrence of liquid junction potential, and typically prevents contamination of the test solution by solvent molecules or ions, a concern with conventional reference electrodes.

Nevertheless, there are several drawbacks associated with pseudo-reference electrodes. First, they lack thermodynamic equilibrium, making it impossible to calculate their potential. Second, as these electrodes are not perfectly nonpolarizable, their potential may shift during measurements, depending on the applied current density. Third, most pseudo-reference electrodes operate effectively within a limited range of conditions, such as specific pH or temperature ranges, and exhibit unpredictable behavior outside of these confines. It is notable, however, that under carefully chosen conditions, the potential of a pseudo-reference electrode, though not quantifiable, can remain surprisingly stable during experiments [30] [31].

# 3

## Experimental setup and equipment

There are two test setups used for experiments. The one in Section 3.1 is used to validate the use of the (pseudo)reference electrodes in the relevant conditions. Section 3.2 lays out the design and setup of the eventual stack that was used to measure shunt currents.

### 3.1. Reference electrode validation setup

In order to investigate whether the reference and pseudoreference electrodes under consideration can be properly used to measure potential differences under the conditions of the realised stack, a controlled test environment was designed. Schematic overviews of a side and top view of the controlled test environment are given in Figure 3.1.

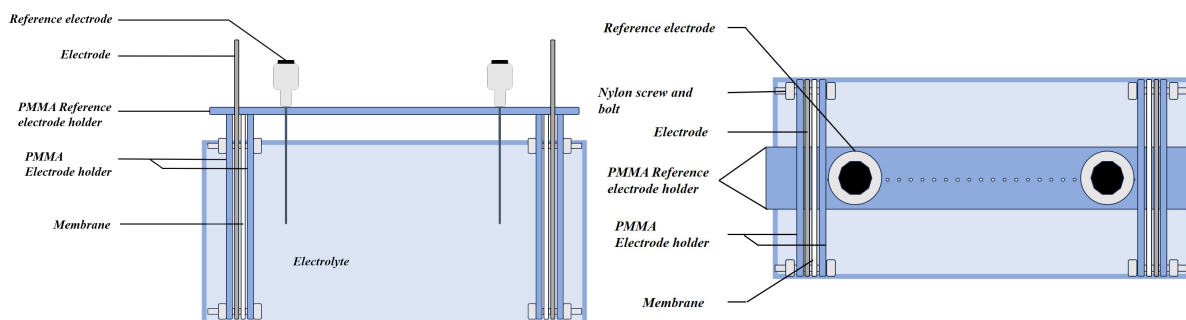


**Figure 3.1:** On the left: A schematic overview of the side view of the (pseudo)reference electrode validation set up. On the right: A top view. The components listed are the same on each side.

The figure shows two reference electrodes placed in the middle of two working electrodes. The distance between the two working electrodes was maintained at 80 mm for all performed measurements. The distance between the (pseudo)reference electrodes can be altered in increments of 5 mm. By applying a potential between the two Nickel electrodes, electrolysis will commence and an electric field emerges in the area between these electrodes. This electric field should result in a linear potential drop between the two electrodes and can be detected with the reference electrodes. This is visualized in Figure 3.2.

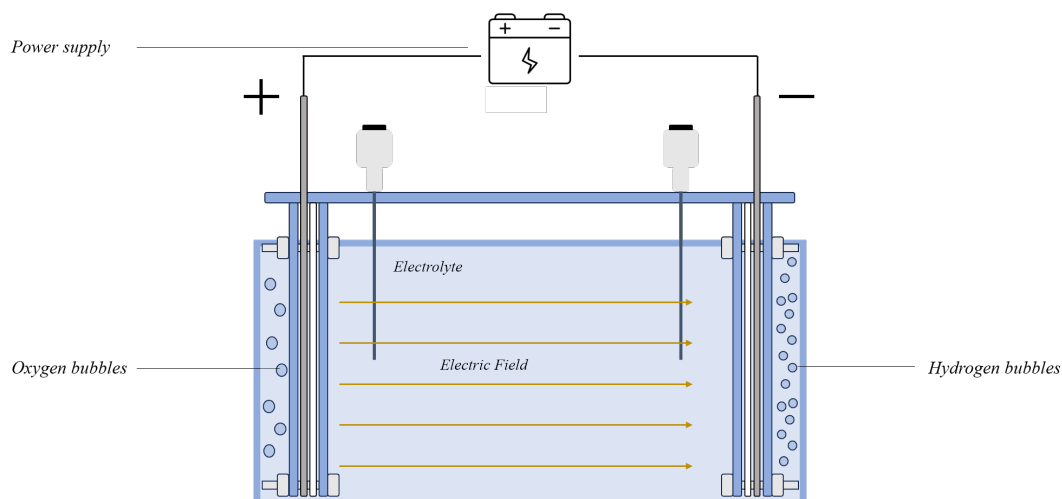


**Figure 3.2:** A schematic overview of the (pseudo)reference electrode validation set up. Connected to a power supply.

The same set-up is used with copper wires and silver wires as pseudoreference electrodes instead of the reference electrodes. This is done to gain an understanding of the behaviour of these pseudoreference electrodes when compared to actual reference electrodes. The cross-sectional area through which the ions move is not completely 1 dimensional, due to the design of the electrode holder. With the goal of completely shielding off bubbles from interfering the potential measurements in between the electrodes, the membrane was clamped tightly to the front side of the electrode by the electrode holder. The shape of the electrode holder can be seen in Figure 3.3.

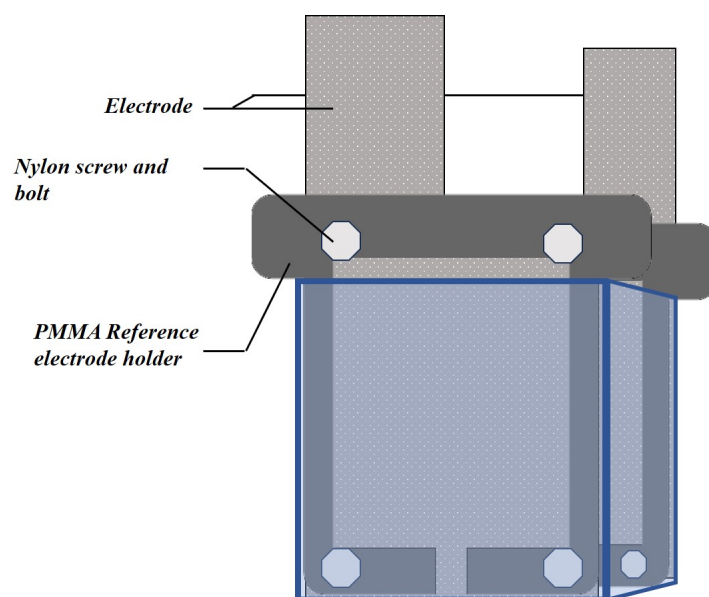


**Figure 3.3:** A schematic representation of a short side view of the (pseudo)reference electrode validation set up. The membrane, (pseudo)reference electrode holder and the reference electrodes are left out for a clearer view.

An image of the used set-up is visible in Figure 3.4.

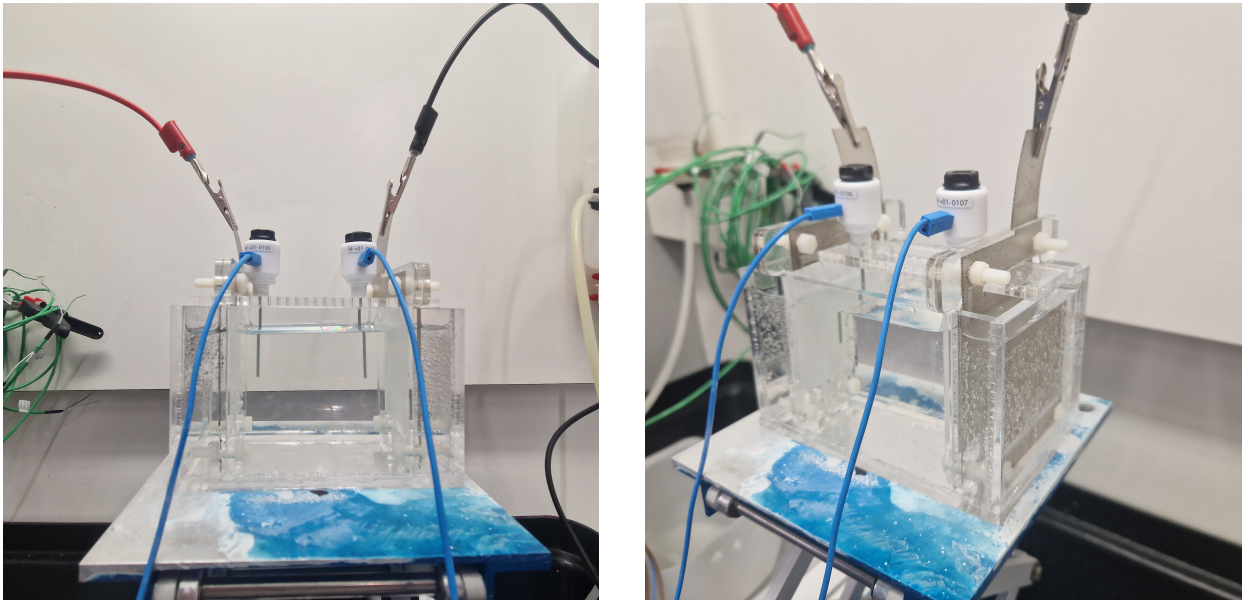


**Figure 3.4:** The controlled test environment used for (pseudo)reference electrode validation and calibration.

The reference electrodes used are made by Gaskatel and contain a hydrogen cell with a constant redox potential. This type is specifically designed to be used in highly concentrated alkaline solutions and is effective in a pH range of -2 through 16. The measuring electrode is made out of a Platinum and Palladium alloy. A schematic overview of the used reference electrodes is given in Figure 3.5

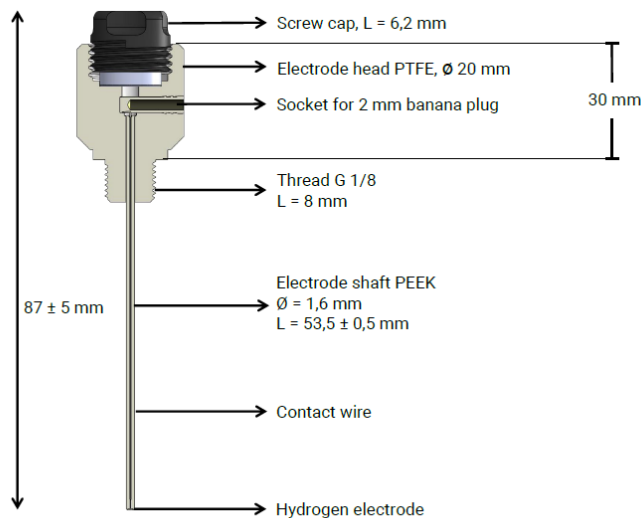


**Figure 3.5:** A schematic overview of the Gaskatel mini Hydrogen reference electrode. Retrieved from [32]

The pseudoreference electrodes used are copper and silver wires. Because the wires lack a thermodynamic equilibrium it is not accurate to use copper and silver simultaneously; it is either copper or silver. The copper has a 0.4 mm diameter and is of a purity of 99.9 %. The silver has a 0.5 mm diameter and is of a 99.95 % purity.

### 3.2. Electrolyser stack design

A 5 cell alkaline water electrolyser stack was designed according to the design principles from [12] and [13], using the zero gap, corrugated electrode, series connected and bipolar electrodes as described in Section 2.2. A design according to these principles was already realized to construct a 1-cell version in a prior thesis [13]. This

design was ameliorated to solve issues related to leak tightness. A schematic overview from this design, made in Solidworks, is shown in Figure 3.6. The realized stack is visible in Figure 3.7.

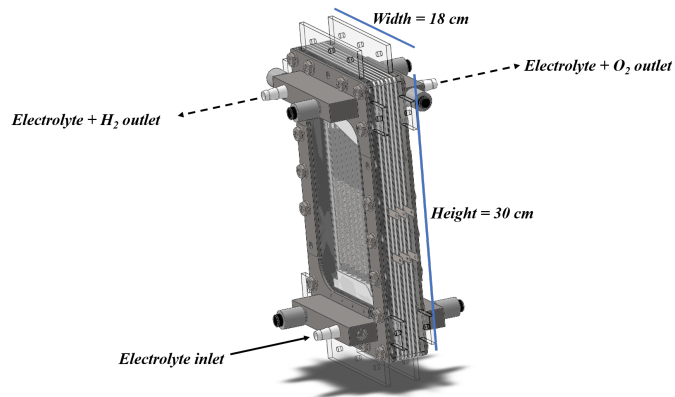


**Figure 3.6:** A schematic overview of the corrugated plate electrode, zero-gap, electrolyser. Made in SolidWorks.



**Figure 3.7:** A frontview of the built 5-cell electrolyser stack. ERIKS, a specialized industrial service provider that offers a wide range of technical products, was the main sponsor of this project.

The entire stack is compressed by tightening 20 M8 bolts along the outside edges and 8 M4 bolts along the top and bottom of the inside edges of the stainless steel frame. The anodic and cathodic outlet manifolds are on opposite sides of the electrolyser, as visualized in Figure 3.6. An exploded view of a single cell of the design is given in Figure 3.8, all indicated components are described in table 3.1. Numbers 5,6,7,8,9 and 10 are repeated to create the remaining 4 cells.

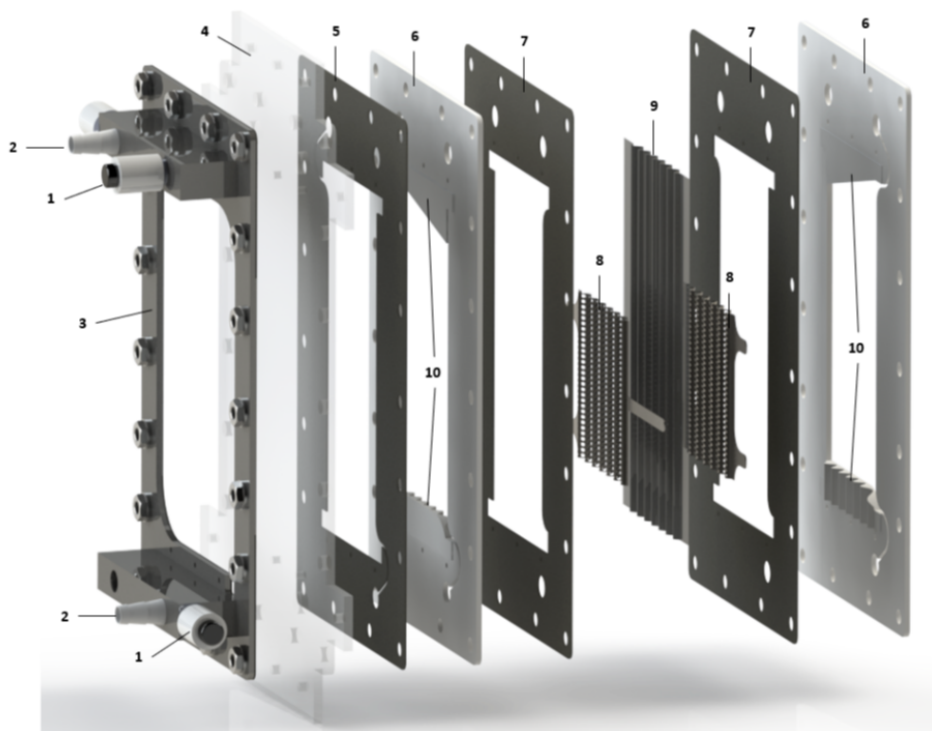


**Figure 3.8:** An exploded view of a single cell of the zero-gap, corrugated plate electrode electrolyser.

Number	Component name	Function	Thickness
1	Reference electrode	Measured potential difference along entire length of headers and footer	-
2	Tube connector	Connects the electrolyte basin to the pump and to the electrolyte inlet at the bottom. Connects the anodic and cathodic outlet headers to gas-liquid separators.	-
3	Stainless steel frame	Allows for an even pressure profile along the outside of the electrolyser.	3mm
4	PMMA endplate	Closes the stack externally and allows for an open view of the front and back electrode.	4mm
5	EPDM Gasket	Seals the PMMA plates so no leakages occur. Allows for the electrode flaps and pseudoreference electrodes to stick out on the sides without leakages occurring.	1mm
6	PMMA plate cell	provide a compartment for the anodes and cathodes	4mm
7	EPDM gasket	Seals the PMMA plates so no leakages occur. Allows for the electrode flaps and pseudoreference electrodes to stick out on the sides without leakages occurring.	1mm
8	Nickel electrode	Electrical conductor that makes contact with the electrolyte and acts as either an anode or a cathode depending on the connection to the power supply.	0.5mm
9	Zirfon perl membrane	Separates the produced gases in the compartments. Is sandwiched between two nickel electrodes.	0.5mm
10	Slanted clamping block from 3D-printed ABS	Clamps the membrane (9) in order to prevent deformation due to flow during electrolysis. Secondary, it leads the gas bubbles towards the outlet channel of the compartment.	4mm

**Table 3.1:** Description of all indicated electrolyser components listed in Figure 3.8.

The electrolyte is inserted in the ‘Electrolyte inlet’, indicated in Figure 3.6, with the use of a Heidolph peristaltic pump to realize high flowrates with a range of 342 - 2379 mL/min and a BT100-3J peristaltic pump from Longer to realize lower flowrates ranging from 2.98 to 586 mL/min. Immediately downstream of this inlet is the footer (refer to Figure 3.12), which is in direct contact with all 10 electrode compartments via narrow channels. The anodic and cathodic chambers are simultaneously filled with the electrolyte through these inlet channels at the bottom, indicated in red in Figures 3.9 and 3.10. When all compartments are filled with electrolyte, the outer two electrodes can safely be connected to a power supply, making the back electrode anodic (positively charged) and the front electrode cathodic (negatively charged), by choice. All 8 electrodes in between are connected in a series connection, further explained in Section 3.3. When electrolysis commences, hydrogen and oxygen are produced at each cathode and anode, respectively. The gases ascend, forced by both their buoyancy as well as the pump, and are guided through their respective outlet channels, also marked in red in Figures 3.9 and 3.10. When these channels are passed, the gas-liquid mixture reaches its respective header. The anode and cathode headers are highlighted from a top view in Figure 3.11.

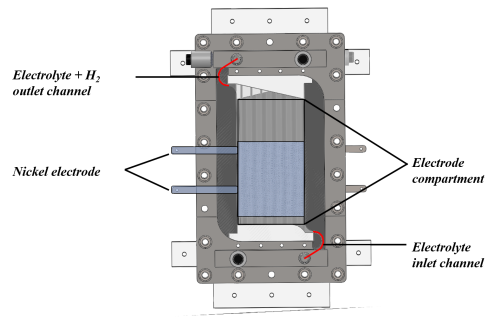


**Figure 3.9:** A schematic drawings of the front side of the electrolyser stack. The red arcs indicate the narrow channels through which is the electrolyte inserted in the electrode compartment and where the electrolyte-hydrogen mixture leaves the electrode compartment.

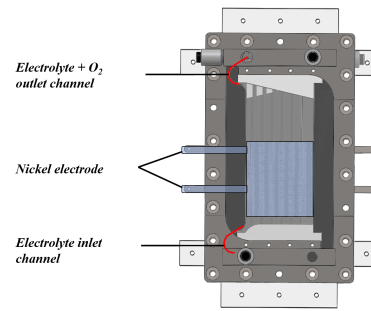


**Figure 3.10:** A schematic drawings of the front side of the electrolyser stack. The red arcs indicate the narrow channels through which is the electrolyte inserted in the electrode compartment and where the electrolyte-oxygen mixture leaves the electrode compartment.

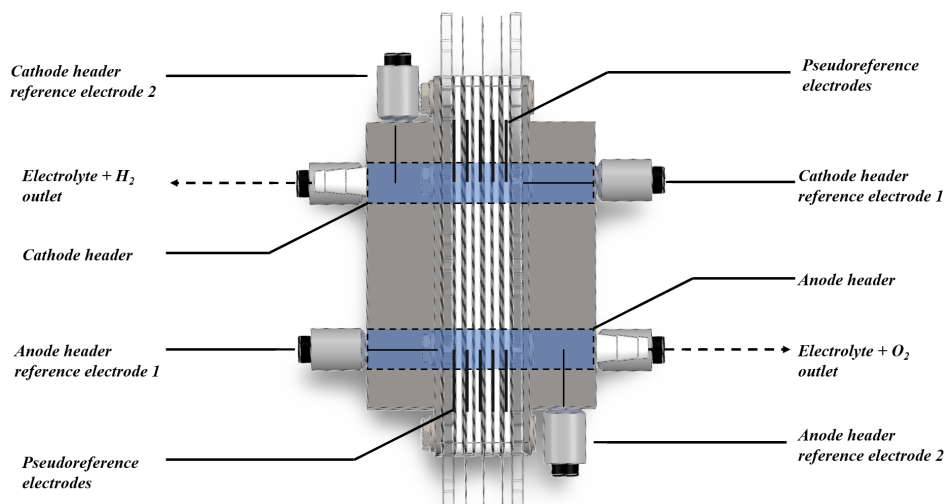


**Figure 3.11:** A schematic drawing of the topview of the electrolyser stack. The two headers (anodic and cathodic) are highlighted including the locations of the reference electrodes and pseudoreference electrodes. The locations of the reference electrodes and pseudoreference electrodes are similar for the footer.

Downstream of the headers, the gas-liquid mixture is transported through external tubing to gas-liquid separators. Here the oxygen and hydrogen are separated from the electrolyte and ascend into a fume hood. The electrolyte is transported to a basin that is again connected to the Heidolph peristaltic pump and can be re-inserted in the stack.

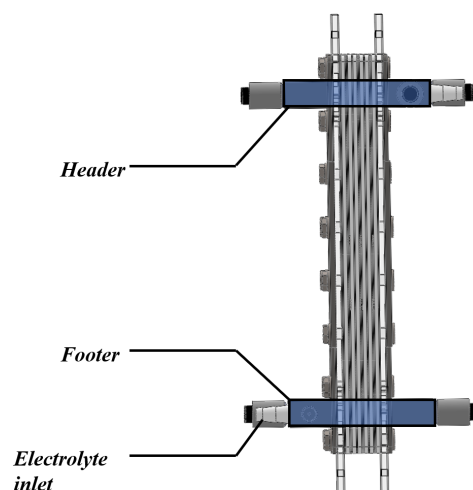


**Figure 3.12:** A schematic drawing of the side of the electrolyser stack. Indicating the header and footer locations.

Figure 3.11 also indicated the locations of the reference electrodes at the beginning and end of each header. There is a similar configuration for the footer. Additionally, the pseudoreference electrodes are portrayed to be between the gaskets just above the 5 outlet and inlet channels, along the headers and footer. An image of copper wires sticking out of the top of the cathodic header is given in 3.13. These reference electrodes and pseudoreference electrodes are used to measure potential differences in the manifolds, from which shunt currents can be calculated. A schematic representation of the inside of the footer, with reference and pseudoreference electrodes is given in Figure 3.14. The same configuration, but upside down, is used for both the cathodic and anodic header.

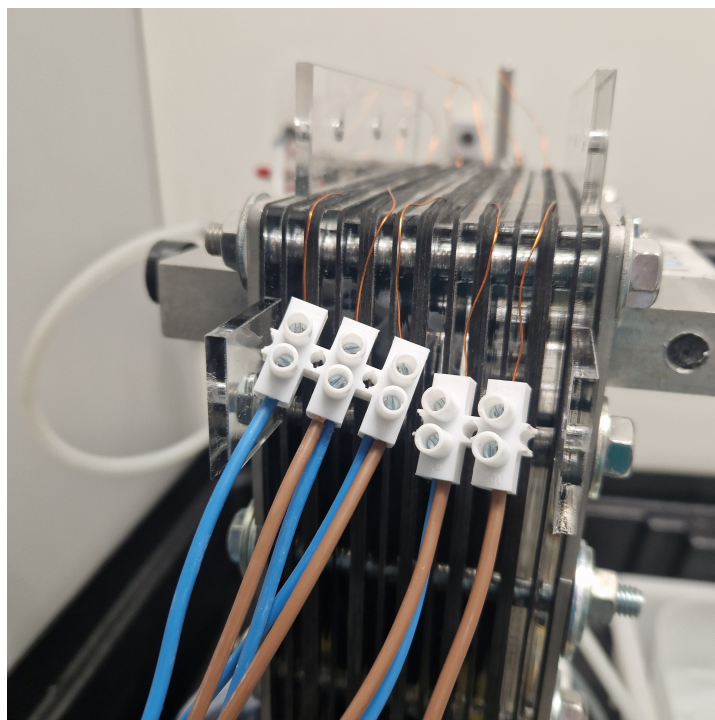


**Figure 3.13:** Copper wires as pseudoreference electrodes sticking out of the cathode header, connected to a terminal block connector.

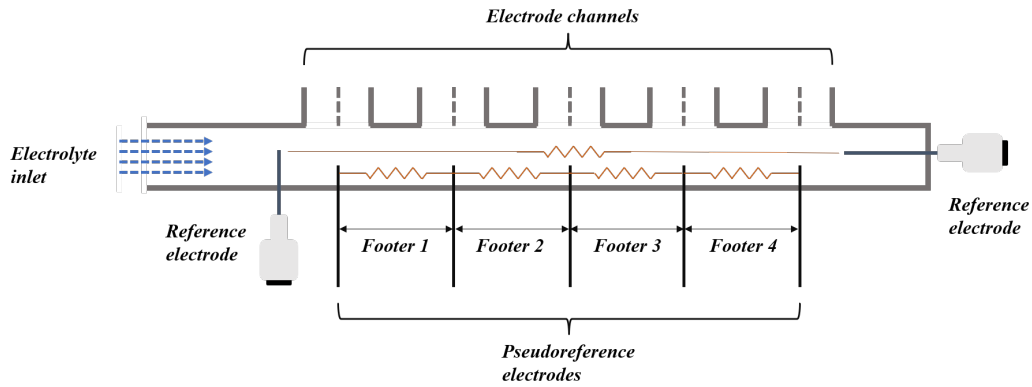


**Figure 3.14:** A schematic representation of the inside of the bottom manifold (footer). The electrolyte is inserted on the left. The 5 pseudoreference electrodes are placed along the length of the manifold. The two reference electrodes are placed at the beginning and end of the manifold. The names Footer 1-4 indicate the four potential differences monitored with the pseudoreference electrodes. The squiggly lines in between the pseudo's and the reference electrodes represent the ohmic resistances along the dimensions of the manifold. The channels that lead to each electrode compartment are visible at the top of the figure.

It must be noted that the manifold resistance used when calculating the manifold shunt current from the potential difference measurements with the reference electrodes, is based on the distance between the first channel and the last channel in the manifold, not the distance between the reference electrodes. As the reference electrodes are located outside the two outer channels, there is no current running in the space between the reference electrodes and the nearest channel.

### 3.3. Nickel electrodes

The electrodes used were made out of a type 201 Nickel plate with a 0.5 mm thickness. This sheet was laser cut in the shape shown in Figure 3.15, where the holes were also lasercut. The wide flaps that stick out to the left form the electrical connection of the electrode. After laser cutting, all plate electrodes received a polish treatment with a #80 SiC foil from Struers. The hole pattern in the electrodes is enlarged in Figure 3.16.

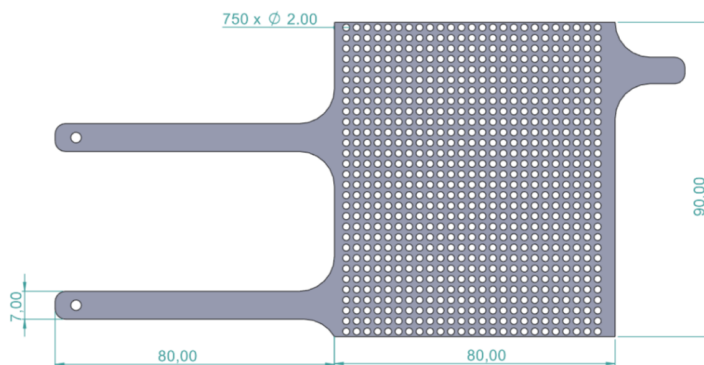


**Figure 3.15:** Nickel electrode

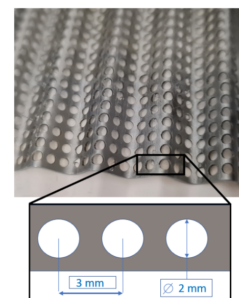


**Figure 3.16:** The hole pattern in the laser cut electrode

In order to corrugate the electrodes, as mentioned in Section 2.2.3, the electrodes were sandwiched with 3D printed molds. This is visualized in Figure 3.17. The waved design increased the electrode surface area to volume ratio approximately by a factor of 1.25[13].

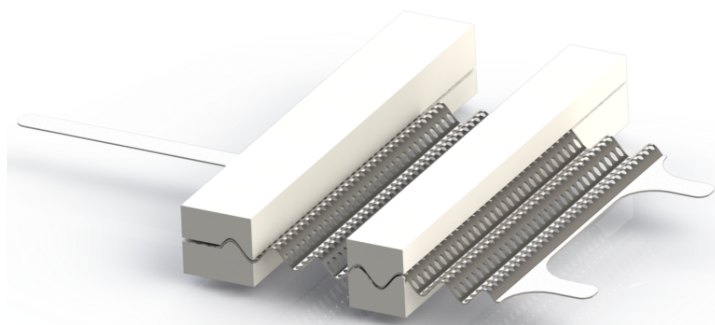


**Figure 3.17:** Nickel electrode corrugation in a 3D-printed mold

All electrodes, except for the test cell, had equal shapes and therefore the same geometric surface area. A single electrode had a geometric surface area of  $8\text{ cm} \times 9\text{ cm} = 72\text{ cm}^2$  that contributed to the electrolytic reaction. The electrodes in the electrolyzer were placed in an almost-zero-gap configuration. As the electrodes did not exactly fit together, the distance between them fluctuated locally between 2 and 4 mm.

The corrugated electrodes are connected in series, to achieve a configuration where the necessary applied current is generally lower than for a parallel connection. In order to realize this series connection, in combination with the topology described in Section 2.2.3, the electrodes are connected to each other externally. A schematic representation of this is given in Figure 2.6.

In the described configuration, the outermost electrodes are interfaced with the power source, establishing one as the anode and the other as the cathode. The external wiring of the system, connecting electrodes 2 and 4, 3 and 5, 6 and 8, as well as 7 and 9, facilitates a bipolar arrangement. This configuration ensures that each electrode in these pairs assumes the role of either an anode or a cathode, depending on which electrode they are facing inside the stack. Additionally, the external wiring between the aforementioned electrodes allows for a direct measurement of shunt currents with a magnetic current clamp.

### 3.4. Magnetic current clamp measurements

To validate and cross-reference the shunt current calculations performed based on the potential differences measured by the reference electrodes, a Voltcraft VC-330 Digital Clamp Meter was used. This device registers the magnetic field present in the wire(s) the device encloses with its clamps, and deduces from it the magnitude of the current running. An image of the Voltcraft magnetic current clamp is given in Figure 3.18. Measuring shunt current along this way is solely possible in this unique design where the electrodes are connected via external wires, as the clamp needs to fully enclose the wires to measure accurately. The current running through the four external wires schematically represented in Figure 2.6 was averaged and deducted from the average current running through the wires connecting the outermost electrodes to the power source. This results in an average total shunt current measured for each set of experimental variable parameters.

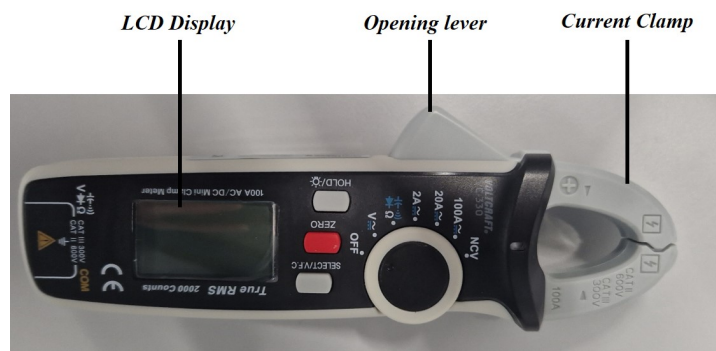


**Figure 3.18:** An image of the Voltcraft VC-330 Digital Clamp Meter

# 4

## Experimental results and analysis

In this chapter, the findings and observations of the experimental research are showcased and analysed. The behaviour of hydrogen reference electrodes, silver pseudoreference electrodes and copper pseudoreference electrodes in an electrolysis generated electric field are treated in Section 4.1. Secondly, the results of the shunt current measurements with reference electrodes and magnetic current clamp meter in the 5-cell, corrugated electrode, bipolar alkaline water electrolysis stack are handled in Section 4.3. The results from the silver and copper wires as pseudoreference electrodes to measure potential differences in the manifold sections are treated in Section 4.4. All measurements depicted below were performed at atmospheric pressure and room temperature. All visual representations of data are analysed in and made by the use of Matlab.

### 4.1. (Pseudo)reference electrode validation

In order to investigate the behaviour and accuracy of the hydrogen reference electrodes, the silver and copper pseudoreference electrodes, the set-up described in Section 3.1 and visualised in Figure 3.1 was used. For each measurement, the electrolysis cell was operated at an applied voltage of 2.5 V and current density of 266 A/m<sup>2</sup>. The effective electrode area of both working electrodes is 37.53 cm<sup>2</sup> and the used electrolyte was a 6 Molar KOH solution. During the measurements of the silver and copper pseudoreference electrodes, the distance between the wires was gradually decreased from 60 to 5 mm in increments of 5 mm. For the reference electrodes the distance was decreased only to 20 mm due to limitations imposed by the dimensions of the gaskatel hydrogen reference electrodes, portrayed in Figure 3.5. At each distance point, the potential difference between the used (pseudo)reference electrodes was recorded. The potential difference was calculated by subtracting the difference in potential after turning on the power supply from the potential when no power was supplied. A total of four measurements were performed for each type of (pseudo)reference electrode to gain insight in the reproducibility of the results and the reliability of the respective (pseudo)reference electrode. Out of these four measurements an average was calculated and plotted with the standard deviation included as errorbars for each individual type of (pseudo)reference electrode. The results are visible in Figure 4.1. A least squares fit with a forced y-intersect at x=0 is applied to each set of data points. Three distinct plots with all 4 measurements per (pseudo)reference electrode are portrayed in Appendix D.

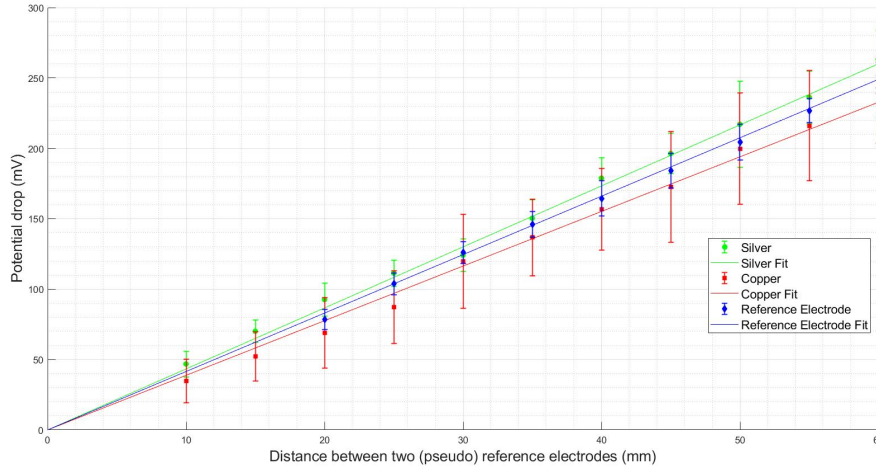


**Figure 4.1:** Average potential difference vs the distance between them in the controlled test cell for (pseudo)reference electrode validation for hydrogen reference electrodes, copper wires and silver wires.

The above figure show linear behaviour for each of the used (pseudo)reference electrodes, according the expected relation between voltage ( $U$ ), electric field ( $E$ ) and distance ( $x$ ) seen in Equation 4.1.

$$E = -\frac{dV}{dX} \quad (4.1)$$

From the gathered data presented in the above graphs, it is possible to calculate a value for the conductivity of the electrolyte,  $\kappa$ , by rewriting the general equation for the resistance,  $R$ , of an object given below.

$$R = \frac{L}{\kappa A} \quad (4.2)$$

Where  $L$  is the length of the object and  $A$  is the cross-sectional area of the object. Isolating  $\kappa$  and taking the distance between the (pseudo)reference electrodes  $dX$  and the measured potential difference between them  $dV$  results in Equation 4.3:

$$\kappa = \frac{dX}{A * \frac{dV}{I}} \quad (4.3)$$

Where  $\frac{dX}{dV}$  is the inverse of the slope of the fitted line per data-set.  $I$  is the applied current which is kept constant throughout the measurements. This is done for all 12 measurements; the values are given in Table 4.1, including the average per used (pseudo)reference electrode. Differences in calculated values based on measurements and the value that results from literature could be caused by the geometry of the set-up described in Section 3.1. As can be seen in Figure 3.3, the exposed area of the electrode is not equal to the cross-sectional area of the container. This can cause an uneven distribution of the electric field between the two electrodes, leading to uncertainties in the calculated values, as Equation (4.3) assumes an homogeneous electric field. Also visible in Figure 3.3 is the asymmetry in the electrodes due to the flaps sticking out of the top on one side. This asymmetry can lead to the current distributing in-homogeneously over the electrode, also resulting in a non-uniform electric field.

A clear noticeable distinction between the 3 fits is the variability of the four measurements. The spread of the measurements is visually the largest for the copper wires and the smallest for the reference electrodes. This is expressed mathematically in outermost right column of Table 4.1, where the standard deviation of the conductivity calculations is given.

Type	Calculated conductivity (S/m)	Average (S/m)	Standard deviation(S/m)
Reference electrodes	67.8	64.3	2.76
	61.1		
	64.6		
	63.8		
Silver wires	70.0	61.7	5.69
	58.29		
	57.82		
	60.5		
Copper wires	73	69.7	10.62
	82.65		
	65.32		
	57.89		
Conductivity probe		59.8	
Literature [33]		56.97	

**Table 4.1:** Conductivity calculations of 4 different measurements of two reference electrodes, silver wires and copper wires in the controlled (pseudo)reference electrode validation set-up. The outright column gives the calculated standard deviation values based on the four measurements of the conductivity.

The lowest value of 2.76 for the reference electrodes is as expected, as the reference electrodes have a fixed and stable redox potential, as mentioned in Section 2.4. This stability is supposed to ensure a constant measurement of the electric field and the measurements performed support this, at least in relation to the pure silver and copper wires. Concerning the standard deviation values, there is also a difference between copper and silver. The silver wires seem to perform considerably better and more stable as pseudoreference electrodes when compared to the copper wires. This also follows from the Pourbaix diagrams of both copper and silver portrayed in Appendix A. In alkaline solutions, silver has a well-defined oxidation potential, forming a layer of silver oxide ( $\text{Ag}_2\text{O}$ ). This oxide layer can be stable and provides a relatively consistent reference potential [34]. This  $\text{Ag}_2\text{O}$  layer is stable between the range of approximately +0.3 and -0.8 V, when analyzing the pourbaix diagram. Considering copper, metallic copper ( $\text{Cu(s)}$ ) is stable at potentials below about -0.8 V at a pH of 16. In the range between -0.8 V and 0 V there can be a mixture of  $\text{Cu}_2\text{O}$ ,  $\text{CuO}_2^{2-}$  and  $\text{Cu(s)}$ , indicating the instability visible in Table 4.1. This is further supported by the raw data graphs of the potential difference versus distance measurements of copper and silver, given in Figures 4.2 and 4.3.

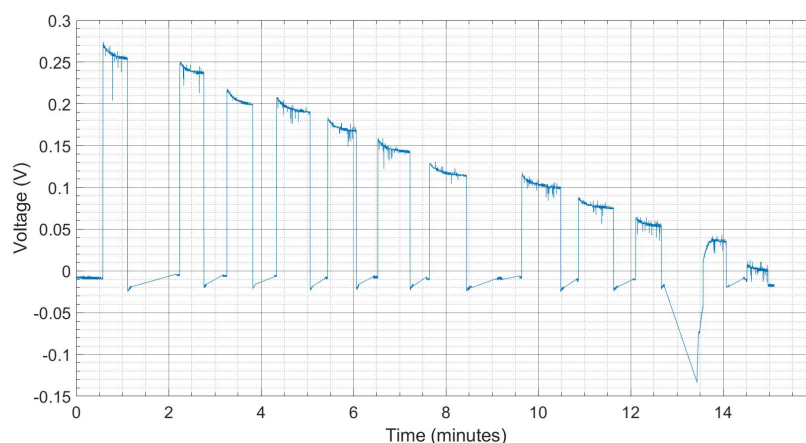


**Figure 4.2:** Potential drop versus distance measurement for the silver wires. Each voltage jump at a specific time interval indicates a different distance between the reference electrodes. The first step is at 60 mm and the last step at 5 mm. The distance is decreased by increments of 5 mm.

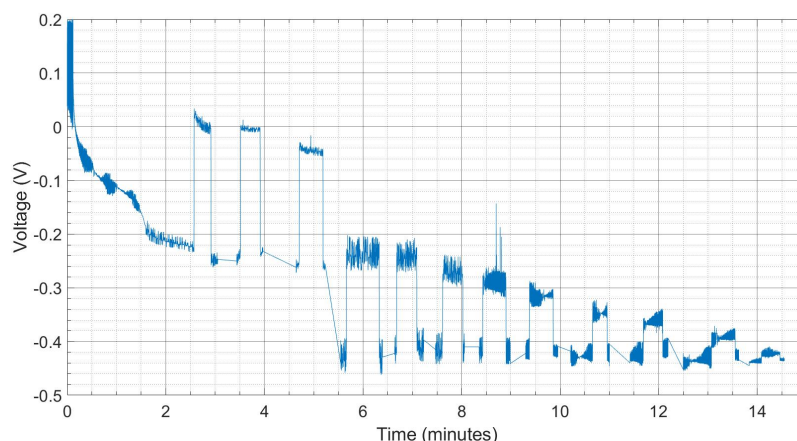


**Figure 4.3:** Potential drop versus distance measurement for the copper wires. Each voltage jump at a specific time interval indicates a different distance between the reference electrodes. The first step is at 60 mm and the last step at 5 mm. The distance is decreased by increments of 5 mm.

As mentioned before, voltage differences were systematically recorded at varying distances in the presence of an electric field. These measurements were compared to corresponding voltage values obtained in the absence of an electric field, at the same distances. Specifically, after each voltage measurement under an electric field, the power supply was deactivated, allowing the system to reach an equilibrium value. This process resulted in step decreases in voltage observed at specific time points, as evidenced by the graphical data. Subsequently, the distance was reduced by 5 mm, and the power supply was reactivated for further measurements. Upon examining the data for copper, a notable deviation was observed after the third measurement, approximately 6 minutes into the experiment. Here, the equilibrium potential decreased from -0.25 V to -0.43 V. This shift suggests a potential alteration in the predominant ionic species present at the surface of the copper wire. In contrast, the data for silver wires demonstrated more consistent results. The equilibrium potential values for silver returned to nearly identical levels after each measurement, indicating a more stable behavior in comparison to the copper wire measurements. A raw data measurement plot for the reference electrodes, showing a stable baseline potential, is portrayed in Appendix D.

Table 4.1 also shows the average calculated value for the conductivity of the electrolyte for each used (pseudo)reference electrode, as well as the values that follow from literature and a conductivity probe measurement. The reference electrodes measure a deviation of 7.5 % from the probe measurement whereas the silver wires measure a deviation of only 3.2 %. Even though this is unexpected and likely due to coincidence, it indicates that the silver wires, under the given circumstances, function surprisingly well to measure potential differences. It can be concluded that silver wires are preferable to use as pseudoreference electrodes than copper wires, under the circumstances described.

## 4.2. Electrochemical performance of the stack

Figure 4.4 shows the j-V curve of the assembled stack. It portrays the total voltage at specified current densities.

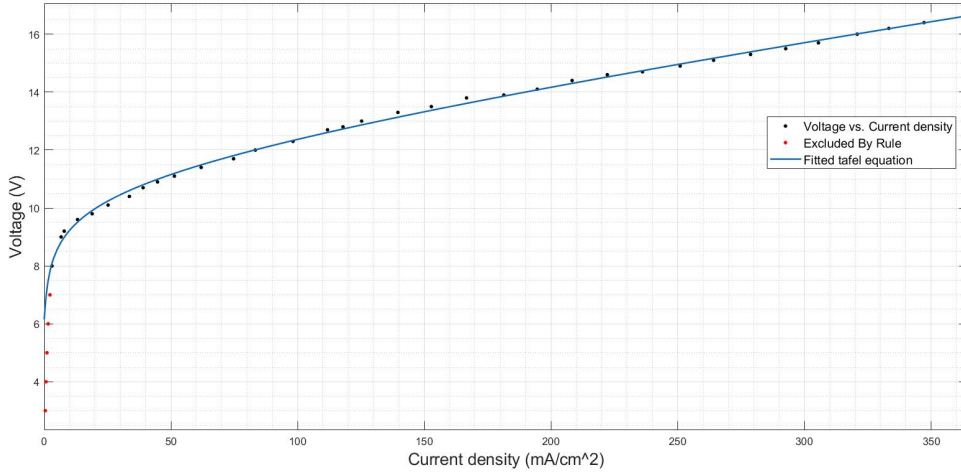


**Figure 4.4:** j-V curve of the stack at room temperature, atmospheric pressure and with 6M KOH electrolyte. Data points with a value below  $V_{\text{stack}} = 8$  V are excluded by rule as the stack is not operating in a manner expressible by this equation in that region.

The fitted curve is made by adapting Equation (2.12) by adding a term for the standard equilibrium potential  $V_{\text{rev}}^0$ , and approximating the natural logarithm as an inverse hyperbolic sine function, which is valid the situation where  $x \gg 1$ . This results in the following expression to calculate the cell potential:

$$V_{\text{stack}} = 6.15 + b \operatorname{asinh} \left( \frac{j}{2j_0} \right) + jAR \quad (4.4)$$

In Equation (4.4), the first term (6.15) is the standard equilibrium potential of a 5-cell stack (5 times 1.23 V). The second term represents the activation overpotentials and the third term stands for the ohmic resistances in the stack. Data points with a value below  $V_{\text{stack}} = 8$  V are excluded by rule as the stack is not operating in a manner expressible by this equation in that region. From this fit, expressions could be retrieved for the Tafel slope ( $b$ ), the exchange current density ( $j_0$ ) and the ohmic resistance times the electrode area ( $AR$ ). These are shown in Table 4.2 below.

<b>Coefficients:</b>	$j_0$ (mA/cm <sup>2</sup> )	$b$ (V)	$AR$ (k $\Omega$ * cm <sup>2</sup> )
<b>Values:</b>	2.609	0.9071	0.0117

**Table 4.2:** Parameters resulting from fitting Equation (4.4) on the data points visualized in Figure 4.4.

It must be noted that to extract the activation overpotential and ohmic resistance of a single cell, the values must be divided by five.

### 4.3. Shunt currents in a 5-cell alkaline water electrolysis stack

The following section presents and analyzes the results from the shunt current measurements of the 5-cell, bipolar, series-connected, corrugated electrode, alkaline water electrolyser stack described and visualized in Section 3.2. The shunt currents are calculated based on measured potential differences with the reference electrodes in the manifold sections and the calculated ohmic resistances of the respective manifold sections. The conductivity of the electrolyte used in the calculations is the value measured with the conductivity probe from Table 4.1. Additionally, the shunt currents are recorded through instantaneous measurements by the hand of a magnetic current clamp to cross-reference and compare the values that result from the potential difference measured with the reference electrodes. The variable parameters during this research are the pump flow rate and the applied current density with the power source. Each set of parameters has a specific void fraction that results in a specific resistance calculation according to Equations (2.15) and (2.16). Alongside the measured shunt currents, the expected total shunt current is calculated based on Equation (2.23). The expected shunt current is calculated for each combination of liquid and gas flow rate, each with a distinct void fraction affecting the channel resistances of the headers. The channel resistance of the bottom channels remain the same for each flow rate, as no gas bubbles

interfere and increase the resistance. In this expected shunt current calculation the cell voltage ( $V_C$ ) used is the total applied voltage divided by 5, minus the ohmic resistance per cell that follows from (4.4). The  $R_E$  and  $R_I$  used in this calculation are the anode and cathode channel resistances. In total, the equation for the shunt current ratio looks like the following:

$$\psi = \frac{V_C}{12I_0} * \left( \frac{1}{R_{u,c}} + \frac{1}{R_{u,a}} + \frac{1}{R_{l,a}} + \frac{1}{R_{l,c}} \right) (N^2 - 1) \quad (4.5)$$

Here  $R_{u,c}$  and  $R_{u,a}$  are the upper cathode and anode channel resistances, which depend on the void fraction at that specific flow rate and current density regime according to Equations (2.15) and (2.16). These are all given in Appendix C.  $R_{l,a}$  and  $R_{l,c}$  are the lower channel resistances, also given in Appendix C, which are constant throughout all measurements as the void fraction is always zero for the lower channels.  $I_0$  is the applied current for that measurement, which can be left out of the equation if the total shunt current is to be calculated, as the total shunt current is retrieved by multiplying the shunt current ratio with the applied current.

It must be noted that the shunt current in the manifolds (cathode header, anode header, footer) are calculated based on the manifold resistances and the measured potential differences with the reference electrodes and the total expected shunt currents are calculated based on the channel resistances and the cell potential.

Images were made at each set of parameters of the outermost anode and cathode to substantiate the measurements and calculations with regards to gas and liquid flow rate. A 38 MP microscope camera from Hayear was used for this purpose. All relevant images made are portrayed in Appendix E. The dimensions of the stack and the void fraction at each flow rate and current density regime used for resistance calculations are listed in Appendix C.

### 4.3.1. Constant current and variable flow rate

In order to investigate the effect of the liquid (electrolyte) flow rate on the behaviour of shunt currents, a series of measurements were performed where the pump flow rate was varied. Relevant variables here are the gas flow rate and the liquid flow rate, as represented in Equations (2.17) and (2.18). Measurements were performed in regimes where the gas flow rate is up to a 10 x higher than, equal to, and down to 100 x lower the liquid flow rate.

#### Lowest liquid flow rate regime

Figure 4.5 shows the average shunt current through both headers and the footer of three identical measurements where the applied current density remained constant at 278 mA/cm<sup>2</sup> and the liquid flow rate was step wise increased from 0.596 to 47.68 mL/min. At this current density the H<sub>2</sub> gas flow rate is 157 mL/min and the O<sub>2</sub> flow rate is 78 mL/min. The standard deviation between the three measurements is visualized in the form of error bars at each data point.

Clearly visible in Figure 4.5 is the virtually zero shunt current in the anode and cathode headers in the region where the liquid flow rate is more than 100 times smaller than the gas flow rate. Due to gas build-up in the top of the electrode compartments, the channels and manifolds are entirely free of the conducting electrolyte. This leads to all shunt current flowing through the footer, which is visibly higher in that region when compared to regions with higher liquid flow rates. The difference in gas build-up between a liquid flow rate of 0.596 mL/min and 47.68 mL/min in the outermost anode is clearly visible in Figures 4.8 and 4.9. Images of the remaining flow rate regimes are portrayed in Appendix E.1.1. Also clearly visible is the higher shunt current in the anode manifold when compared to the cathode manifold at the same electrolyte flow rate. As seen Equation (2.17), the oxygen flow rate is twice as low as the hydrogen flow rate at the same induced current. That means that the void fraction in the anode compartments is always lower at every applied liquid flow rate, when compared to the cathode void fraction. Lower void fraction leads to a lower resistance, and thus a higher shunt current.

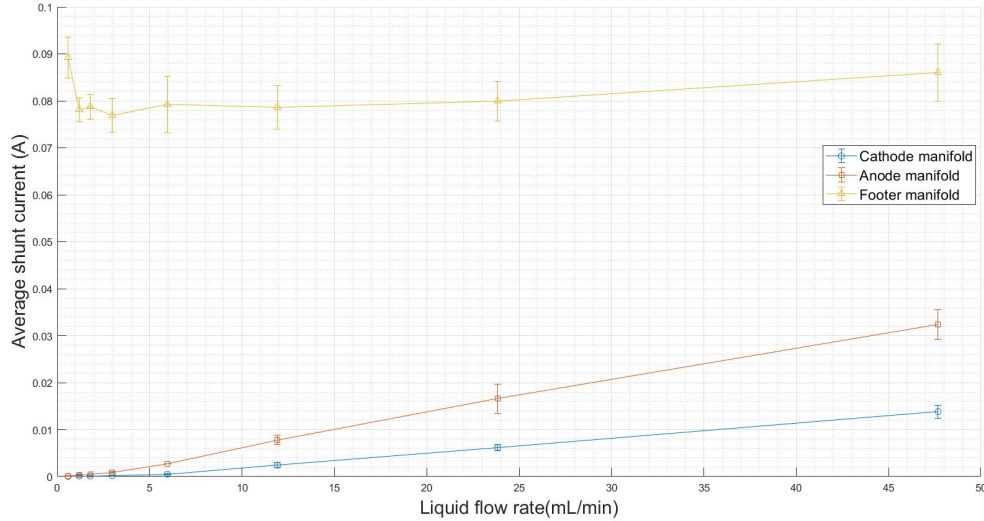
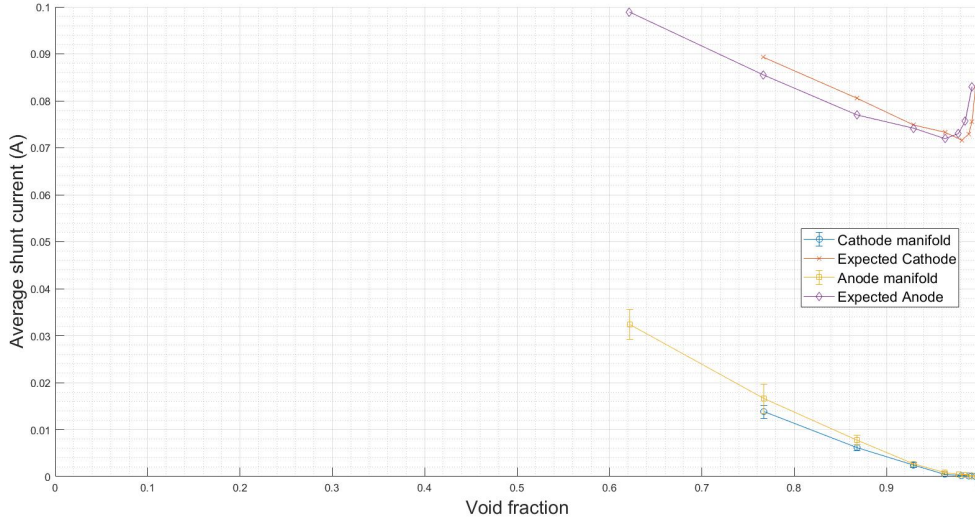


**Figure 4.5:** Average shunt currents in the cathode header, anode header and footer calculated based on potential differences measured with reference electrodes at electrolyte flow rates ranging from 0.596 to 47.68 mL/min. The stack is being supplied with a constant current density of 278 mA/cm<sup>2</sup>. At this current density the H<sub>2</sub> gas flow rate is 157 mL/min and the O<sub>2</sub> flow rate is 78 mL/min.

A graph where the shunt current in the anode and cathode header are plotted against the void fraction, together with the expected shunt current at that void fraction, is to be seen in Figure 4.6. The expected value is an adaptation of equation (4.5) to account only for either anode or cathode. The expected shunt current in this context is calculated according to:

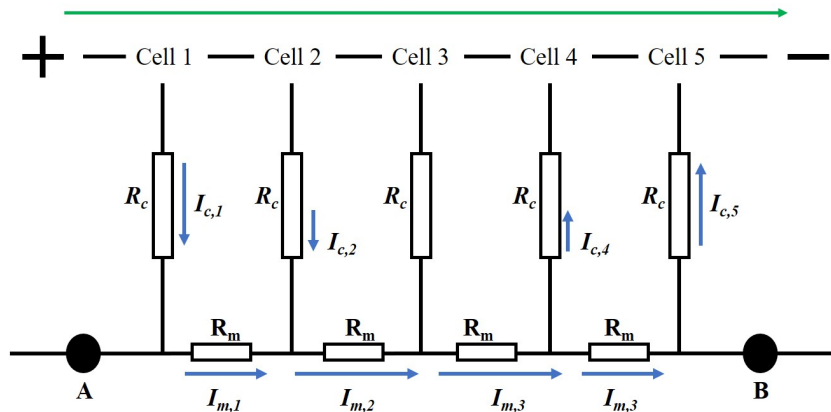
$$I_{\text{shunt,cathode/anode}} = \frac{V_C}{12} * \left( \frac{1}{R_{u,c/a}} + \frac{1}{R_{l,c/a}} \right) (N^2 - 1) \quad (4.6)$$

Figure 4.6 indicated the different behaviour expected from anode and cathode at the same void fraction. The reason that the anode and cathode expected shunt current is not the same when the void fractions are the same, is because the void fractions of anode and cathode are not the same at the same point in time and the cell potentials varied slightly over time. So the expected shunt current of the cathode at a specific void fraction is based on a cell potential recorded later in time when compared to the cell potential used to calculate the expected anode shunt current at that void fraction. What is unexpected, however, is that the measured average manifold shunt current is higher on the anode side when compared to the cathode side, for the same void fraction. The reason for this difference can be explained by factors not accounted for in Equation 4.5. That is the inherent differences between the gas types; oxygen and hydrogen. The bubbles on the anode side behave and move differently when compared to the bubbles on the cathode side. This behaviour is however extremely difficult to quantify and is thus not accounted for in the used equations. Also notable is the difference in magnitude of the expected values compared to the measured manifold averages; The expected shunt current entails the total current shortfall between the current running through the anodes and cathodes and the current supplied to the outermost electrodes. The measured current with the reference electrodes gives the average manifold shunt current. A detailed description on what the average manifold shunt current entails is given below by the hand of Figure 4.7



**Figure 4.6:** Shunt current in the cathode and anode header vs void fraction for an electrolyte flow rate ranging from 0.596 to 47.68 mL/min. The H<sub>2</sub> gas flow rate is constant at 157 mL/min and the O<sub>2</sub> flow rate is constant at 78 mL/min. The expected value for the total shunt current for the anodes and cathodes based on Equation (4.5) is also portrayed.

An explanation for the difference in magnitude between the expected shunt current and the measured shunt current in Figure 4.6 can best be explained by the hand of Figure 4.7, where a highly simplified schematic representation of an equivalent circuit model of the footer is portrayed.



**Figure 4.7:** A simplified schematic representation of the electrical circuit analog of the footer. Each channel has resistance  $R_c$  and each manifold section has resistance  $R_m$ . The reference electrodes are placed at points A and B. The green arrow indicates the ‘desired’ current flow and the blue arrows indicate the shunt current. The magnitude and direction of the channel shunt current is inherently different from the manifold shunt current.

As explained in Section 2.3 and visualized by Figure 2.9, the channel shunt current is zero in the middle of the stack and increases towards both ends of the stack in opposite direction, whereas the manifold shunt current is highest in the middle of the stack and zero at both ends, as visualized by the size and direction of the arrows in the above figure. Looking at Figure 4.7, an ionic shunt current  $I_{c,1}$  runs from Cell 1, through channel resistance  $R_c$  to the manifold. In the manifold, the current passes through the first manifold section resistance  $R_m$  continuing through the second manifold resistance to Cell 3, where the channel shunt current  $I_{c,2}$  from cell 2 is added to the manifold shunt current. After passing through the middle of the stack, a portion of the manifold shunt current,  $I_{c,4}$ , flows toward cell 4. If a potential difference is measured with reference electrodes between points A and B and divided by the total manifold resistance of all added  $R_m$ 's, which is the method used in this thesis, the total current calculated does not entail the total current leaked. The current calculated by measuring the potential difference between A and B will only represent a portion of  $I_m$  passing through the manifold resistance, not the

total added  $I_m$ . That is why the reference electrodes measurements result in an average manifold shunt current. Information on the channel shunt currents leaking from each cell is not measured with the set-up used in this thesis. However, the magnetic current clamps do measure the total shortfall between current applied to the outermost electrodes and current flowing in between the inner electrodes.

It must be noted that the manifold resistance used when calculating the manifold shunt current from the potential difference measurements with the reference electrodes, is based on the distance between the first channel and the last channel in the manifold, not the distance between the reference electrodes. As the reference electrodes are located outside the two outer channels, there is no current running in the space between the reference electrodes and the nearest channel.



**Figure 4.8:** An in situ image of the anode compartment at an electrolyte flow rate of 0.596 mL/min and a  $O_2$  gas flow rate of 78 mL/min per cell. This  $O_2$  gas flow rate is achieved at a current density of 278 mA/cm<sup>2</sup>.

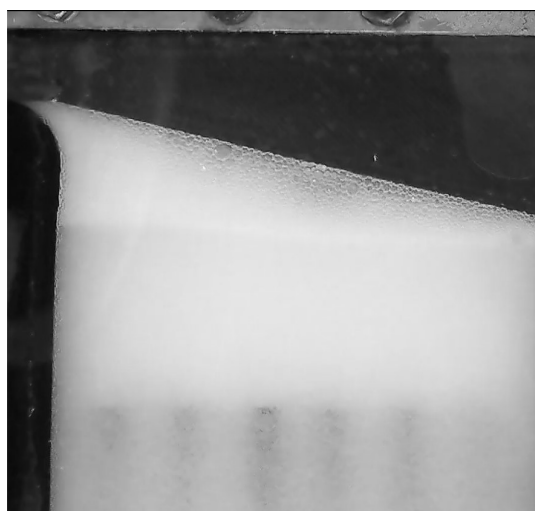


**Figure 4.9:** An in situ image of the anode compartment at an electrolyte flow rate of 47.68 mL/min and a  $O_2$  gas flow rate of 78 mL/min per cell. This  $O_2$  gas flow rate is achieved at a current density of 278 mA/cm<sup>2</sup>.

Figure 4.10 shows the added total average shunt currents through the cathode header, anode header and footer measured with the reference electrodes, the average total shunt current measured with the magnetic current clamp and the expected shunt current calculated with Equation (4.5).

A clear note for these results is the large spread in shunt currents resulting from different measurements with the current clamp, visualized with the error bars. This is likely due to the nature of how the experiments were performed; the clamp measurements are snap shots. At every flow rate regime, which were set for 10 minutes per setting, the current running through the four external wires was measured and subtracted from the current being supplied to the outermost electrodes. The clamp meters could not permanently enclose the wires and measure continuously. Due to the instantaneous nature of these measurements, a large spread is visible.

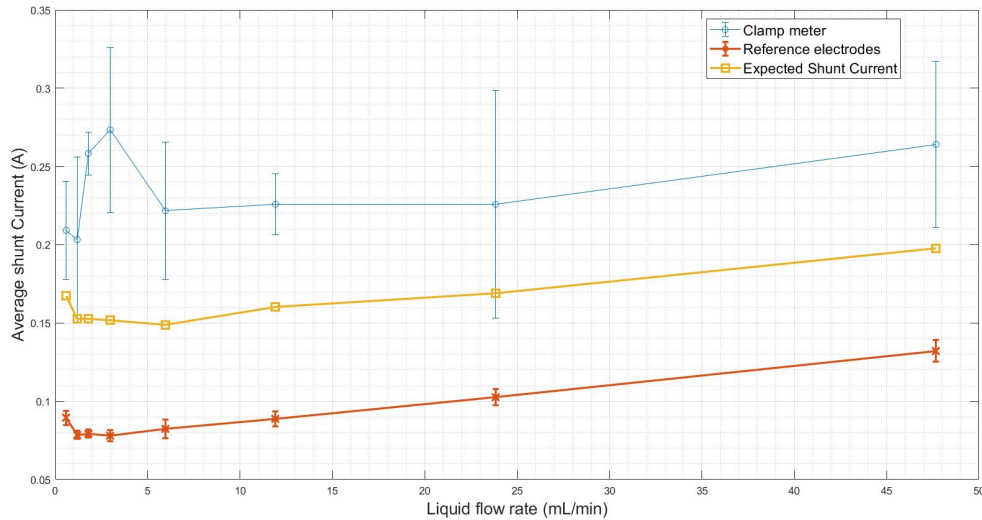


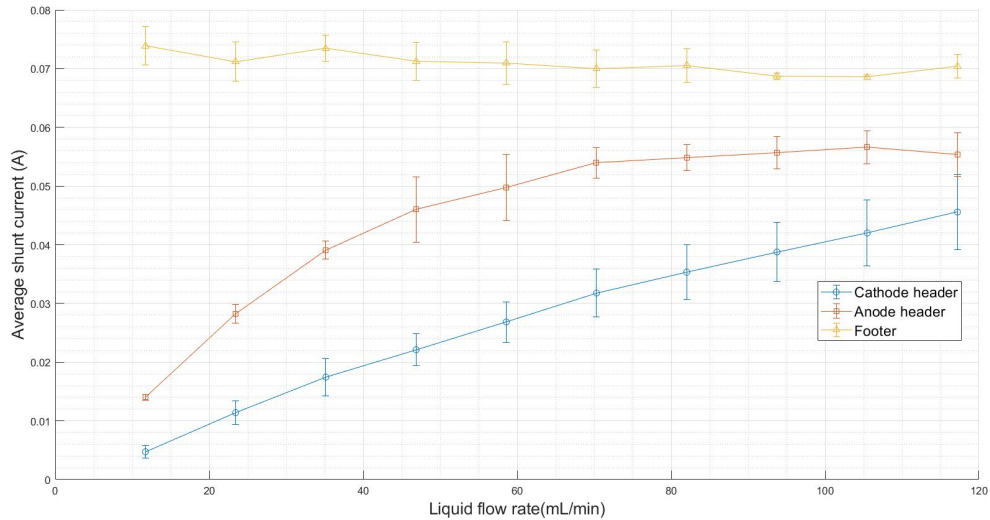
**Figure 4.10:** Total average shunt current measured with reference electrodes and the magnetic current clamp meter including the expected shunt current based on (2.23), at electrolyte flow rates ranging from 0.596 to 47.68 mL/min. The stack is being supplied with a constant current density of 278 mA/cm<sup>2</sup>. At this current density the H<sub>2</sub> gas flow rate is 157 mL/min and the O<sub>2</sub> flow rate is 78 mL/min.

A possible explanation for the difference in magnitude of the expected shunt current based on Equation (4.5) and the shunt current measured with the current clamp are poor contacts between the wires and the electrodes. The wires were connected with M3 bolts and screws to the electrodes and pressed firmly together. As the wires and electrodes were connected and disconnected multiple times for small adaptations, it is very possible that small inconsistencies in the connections took place. If the contact between the wires and electrodes is inconsistent or intermittent, it could lead to fluctuating resistance levels. This can result in variable current flow, which might be averaged out or detected as lower with the current clamp (and thus a higher shunt current).

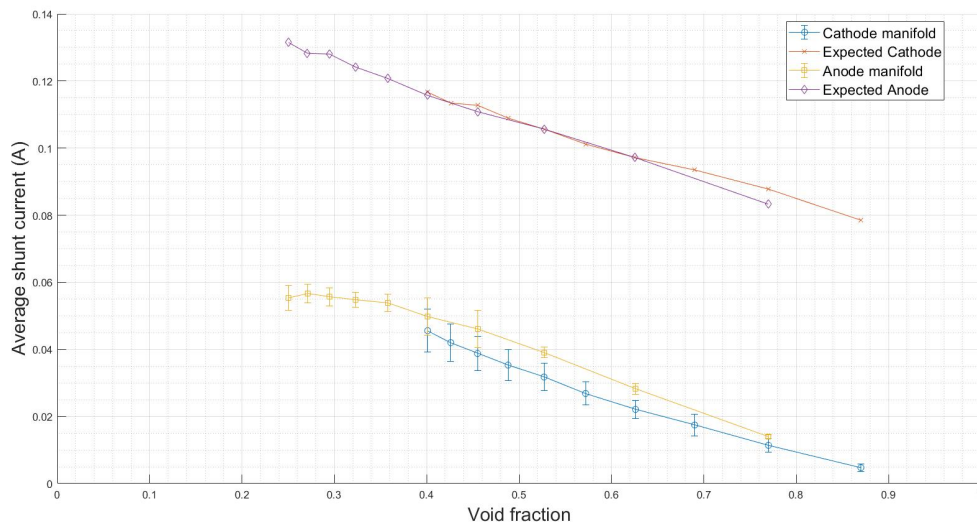
### Medium liquid flow rate regime

Figure 4.11 shows the average shunt current through both headers and the footer of three identical measurements where the applied current density remained constant at 138 mA/cm<sup>2</sup> and the liquid flow rate was step wise increased from 11.72 to 117.2 mL/min. At this current density the H<sub>2</sub> gas flow rate is 77.8 mL/min and the O<sub>2</sub> flow rate is 38.9 mL/min. The standard deviation between the three measurements is visualized in the form of error bars at each data point. Images of the outflow channels of the anode and cathode at each flow rate setting can be seen in Appendix E.2.1.

What can be seen in Figure 4.11 is that the cathode header and anode header shunt current gradually increase with increasing flow rate, while the footer shunt current remains roughly equal. As the liquid flow rate increases to a level where it is about twice as high as the gas flow rate for the anode header (at about 80 mL/min), the shunt current gradually stops increasing and reaches a steady value. For the cathode header, the shunt current keeps increasing nearly linear. What can be seen from the images in Appendix E is that the top of the cathode compartment has large gas build up visible for all flow rates of this regime. The anode compartment has gas build up for flow rates below 58.60 mL/min but not for flow rates higher than this. All flow rates higher than 58.60 mL/min show a homogeneous gas-liquid mixture in the top of the anode compartment. More bubbles in the top of the cell compartment lead to more bubbles in the header, and thus a higher resistance. This leads to lower shunt currents in the cathode header when compared to the anode header, as substantiated by Figure 4.11.



**Figure 4.11:** Average shunt currents in the cathode header, anode header and footer calculated based on potential differences measured with reference electrodes at electrolyte flow rates ranging from 11.72 to 117.2 mL/min. The  $O_2$  gas flow rate is constant at 38.9 mL/min and the  $H_2$  gas flow rate is constant at 77.8 mL/min.



**Figure 4.12:** Shunt current vs void fraction for an electrolyte flow rate ranging from 11.72 to 117.2 mL/min. The  $H_2$  gas flow rate is constant at 77.8 mL/min and the  $O_2$  flow rate is constant at 38.9 mL/min.

Figure 4.12 shows the average measured shunt currents in the cathode and anode manifold plotted against void fraction, together with the expected total shunt current for the anode and cathodes. Just like in Figure 4.13, the expected values are approximately twice as high at each point on the x-axis. This is again due to the nature of the measurements; the reference electrodes measure an average manifold shunt current whereas the expected shunt current refers to the total current mismatch between the current applied and the current running through the electrodes. The behaviour of the expected shunt current and the measured shunt current does show similar behaviour however. Figure 4.13 shows the measured total shunt current values with the current clamp, the manifold shunt current measured with the reference electrodes and the expected shunt current based on Equation (2.23). A clear trend can be spotted in both the measurement techniques and the expected value, indicating that the measurement techniques are in line with the theory.

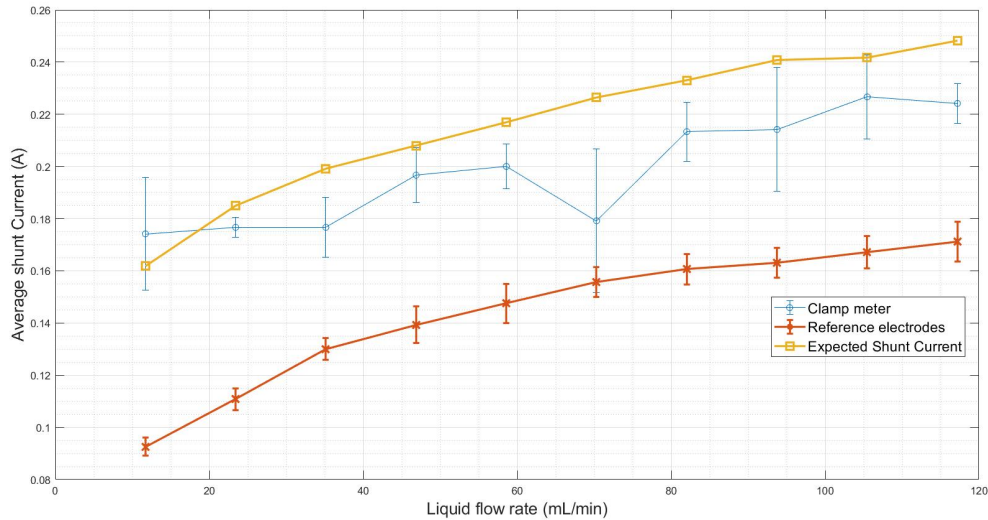


**Figure 4.13:** Total average shunt current measured with reference electrodes and the magnetic current clamp meter, including the expected shunt current, at electrolyte flow rates ranging from 11.72 to 117.2 mL/min. The O<sub>2</sub> gas flow rate is constant at 38.9 mL/min and the H<sub>2</sub> gas flow rate is constant at 77.8 mL/min.

### High liquid flow rate regime

Figure 4.14 shows the average shunt current through both headers and the footer of three identical measurements where the applied current density remained constant at 138 mA/cm<sup>2</sup> and the liquid flow rate was step wise increased from 68.4 to 475.8 mL/min. At this current density the H<sub>2</sub> gas flow rate is 77.8 mL/min and the O<sub>2</sub> flow rate is 38.9 mL/min. The standard deviation between the three measurements is visualized in the form of error bars at each data point. A graph where the shunt current in the anode and cathode header and the void fraction, together with the expected shunt current at that void fraction, is to be seen in Figure 4.16.

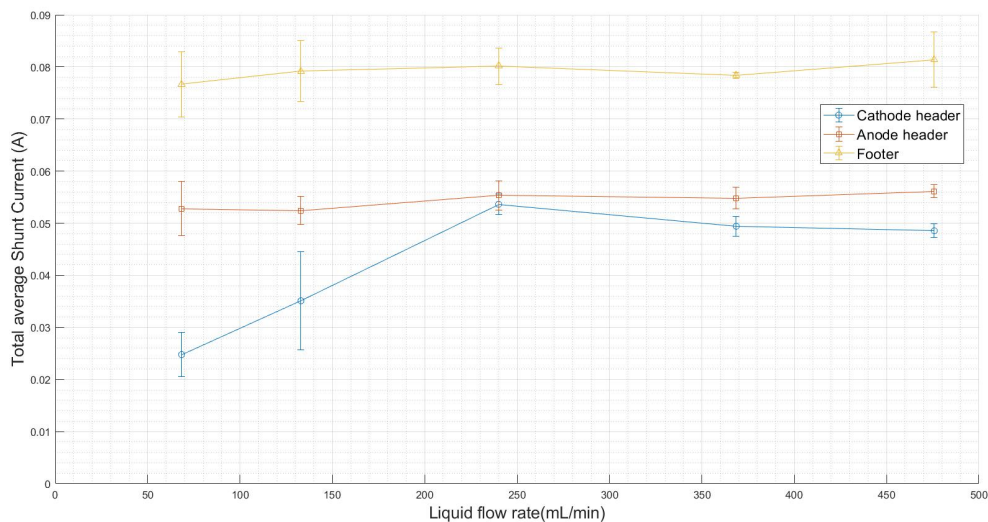


**Figure 4.14:** Average shunt currents in the cathode header, anode header and footer calculated based on potential differences measured with reference electrodes at electrolyte flow rates ranging from 68.4 to 475.8 mL/min. The H<sub>2</sub> gas flow rate is 77.8 mL/min and the O<sub>2</sub> flow rate is 38.9 mL/min.

The figure above shows the increasing shunt current in the cathode header until a liquid flow rate of 240 mL/min. At higher flow rates, all manifold shunt currents seem to remain constant. Increasing the liquid flow rate, and

thus lowering the void fraction, has a significant effect on the shunt current until a certain point. This is supported by the expected shunt current based on Equation (2.23), seen in Figure 4.15. This Figure also shows the large spread of the measurements performed with the magnetic current clamp meter.

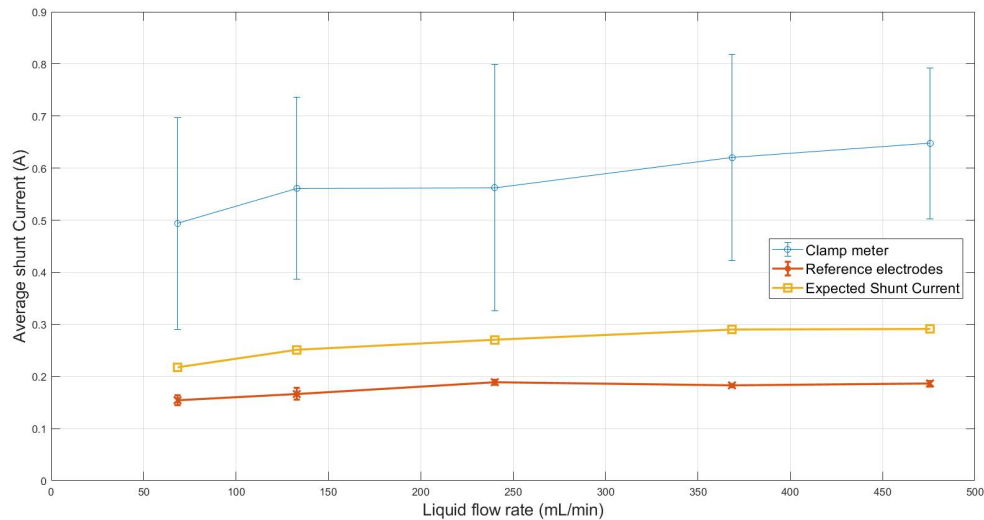


**Figure 4.15:** Total average shunt current measured with reference electrodes and the magnetic current clamp meter, including the expected shunt current, at electrolyte flow rates ranging from 68.4 to 475.8 mL/min. The  $H_2$  gas flow rate is 77.8 mL/min and the  $O_2$  flow rate is 38.9 mL/min.

Looking at Figure 4.16, lowering the void fraction below a value of 0.25 for both anode and cathode seems to bring the average shunt current to steady value. This is however not in line with the expected value based on equation (4.5). Even though the resistances in the manifold decrease with a decreasing void fraction, as can be seen in Table C.12 and C.13, the shunt currents remain constant. This means that the potential differences measured along the headers also decreased, suggesting that Equation (2.23) is no longer valid in the situation where the electrolyte flow rate is more than three times larger than the  $H_2$  flow rate.

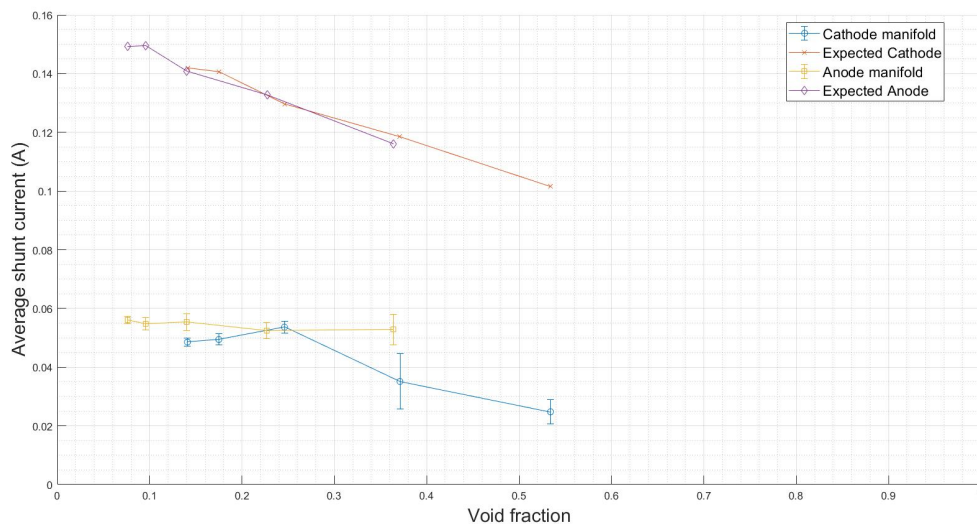


**Figure 4.16:** Shunt current vs void fraction for a electrolyte flow rate ranging from 68.4 to 475.8 mL/min. The  $H_2$  gas flow rate is constant at 77.8 mL/min and the  $O_2$  flow rate is constant at 38.9 mL/min.

### 4.3.2. Constant flow rate and variable current

The results of the variable current measurements are visualized in this section. The applied current density was step wise increased from 60 to 347 mA/cm<sup>2</sup>, while the liquid flow rate remained constant at 70 mL/min per cell. At this current density regime, the O<sub>2</sub> gas flow rate increases step-wise from 20 to 98 mL/min and the H<sub>2</sub> flow rate increased step-wise from 39 to 196 mL/min. The results of the potential measurements along the manifolds can be found in Appendix F.4. Figure 4.17 clearly shows the effect of increasing gas flow rate on the shunt current. As the applied current increases, the amount of gas produced by the anodes and cathodes increases, and thus increasing the void fractions in line with Equations (2.16) and (2.17). This is also substantiated by the images portrayed in Appendix E.3. The increasing amount of gas in the outlet channels and upper manifolds increase the resistance in such a way that the total shunt current in the stack decreases. This is visualized by Figure 4.18. As the footer is not affected by gas bubbles, the resistance of this manifold remains constant. It can be seen that with increasing current density, the shunt current through the footer increases. A graph where the shunt current in the anode and cathode header are plotted against the void fraction, together with the expected shunt current at that void fraction, is to be seen in Appendix G in Figure G.1

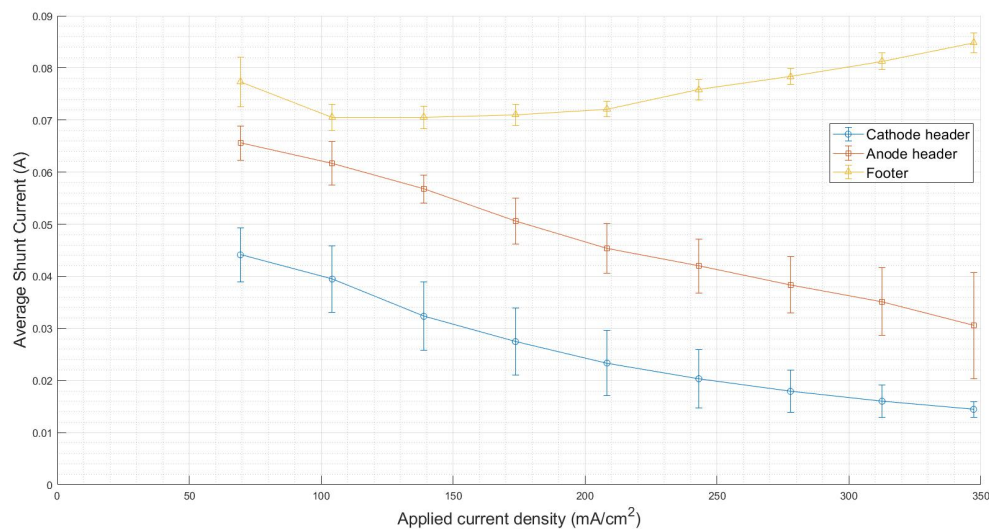


**Figure 4.17:** Average shunt currents in the cathode header, anode header and footer calculated based on potential differences measured with reference electrodes at a constant electrolyte flow rate of 70 mL/min. The O<sub>2</sub> gas flow rate increases step-wise from 20 to 98 mL/min and the H<sub>2</sub> flow rate increased step-wise from 39 to 196 mL/min.

The measurements performed with the magnetic current clamp meter show a more unpredictable behaviour, going up and down. It must be noted that with applied currents higher than 20 A (278 mA/cm<sup>2</sup>), the magnetic current clamp loses accuracy [35]. Both measurements techniques, however, show a clear correlation with the expected shunt current value, indicating that they are effective in quantifying and identifying shunt current in electrolyser stacks of this design.

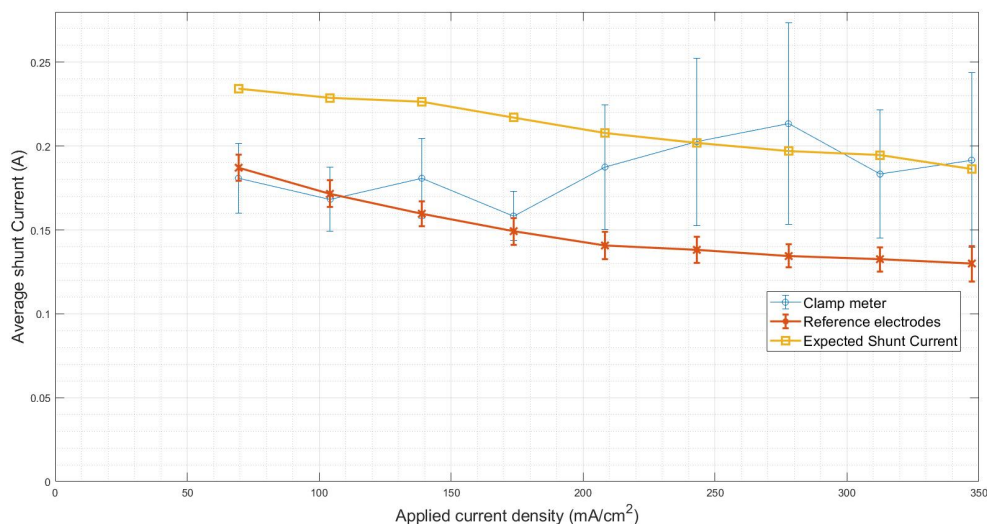


**Figure 4.18:** Total average shunt current measured with reference electrodes and magnetic current clamp meter, including the expected shunt current, at a constant electrolyte flow rate of 70 mL/min. The O<sub>2</sub> gas flow rate increases step-wise from 20 to 98 mL/min and the H<sub>2</sub> flow rate increased step-wise from 39 to 196 mL/min.

#### 4.4. Silver and copper wires as pseudoreference electrodes

The silver and copper wires as pseudoreference electrodes have proven to be ineffective to measure potential differences in this stack design. Whereas the silver wires showed promising results in the controlled test set-up to measure potential differences, the stack results were not reproducible. Figures 4.19 and 4.20 indicate the random and unpredictable behaviour of the potential differences measured with cathode header 1-4. All four potential differences are different in two identical measurements, whereas the green line representing the Hydrogen reference electrodes shows reproducible behaviour. An explanation as to why the silver wires functioned well in the controlled test set-up, but failed to do so in the actual stack, could lie in the manner of how the potential differences were used. In the controlled test set-up, as explained in Section 4.1, the potential differences were measured and subtracted from a baseline value before each individual change of parameter (the distance between the wires). The baseline value was the potential difference measured when no potential was applied between the two electrodes. As mentioned in Section 4.1, that baseline value could vary, and not affect the potential difference measured. In the stack however, to measure actual shunt currents, it is not viable to use only the potential jumps between time intervals with changing parameters. The actual potential difference at each time interval had to be used to measure the actual shunt current.

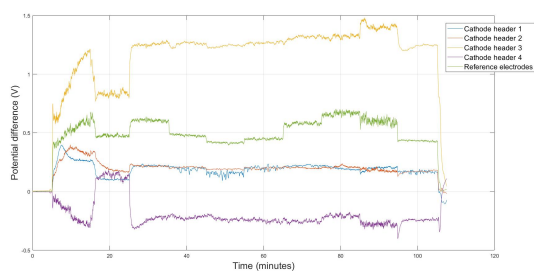


**Figure 4.19:** Potential differences measured with the reference electrodes and silver pseudoreference electrodes along the cathode header. Header 1-4 indicate the potential differences between the subsequent silver wires.

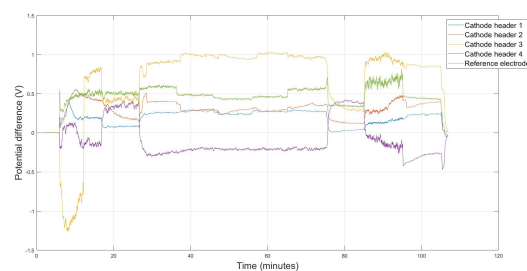


**Figure 4.20:** Potential differences measured with the reference electrodes and silver pseudoreference electrodes along the cathode header. Measurement 2. Header 1-4 indicate the potential differences between the subsequent silver wires.

# 5

## Conclusions and Recommendations

This thesis project aimed to assess different measurement techniques to detect shunt currents in a 5-cell alkaline electrolyser stack and to quantify these shunt currents with respect to electrolyte flow rate and applied current. In order to do so, a literature study was conducted on the fundamental electrochemistry of electrolysis, different stack geometries, shunt currents and mathematical models to describe and predict shunt currents. An experimental study was carried out by building and designing a lab-scale 5-cell, bipolar, external series-connected, electrolyser stack, fitted with hydrogen reference electrodes and silver pseudoreference electrodes to detect potential differences. Additionally, an Excel based mathematical model was designed to approach the realized stack as an Equivalent Circuit Model. Lastly, a controlled test environment was designed and built to focus on the behaviour of the (pseudo)reference electrodes when measuring potential differences in electric fields in a highly alkaline environment. The research was conducted by the hand of the research questions laid out in the introduction, and individually treated in Section 5.1 below. Lastly, recommendations for further research are treated in Section 5.2.

### 5.1. Conclusions

The conclusions from this thesis project are treated per research question below.

***Can hydrogen reference electrodes and pseudoreference electrodes like silver or copper wires be used to accurately measure potential differences in an alkaline electrolysis cell? If yes, which is most accurate?***

The presented controlled test experiment for (pseudo)reference electrode validation in Section 4.1 has shown promising results for copper and silver wires to measure potential differences in an electrolysis cell. The silver wires indicated an electrolyte conductivity +3 % higher than the value measured with a conductivity probe. The copper wires resulted in a value 16 % higher than the value measured with the conductivity probe. It can be concluded that silver wires function better to measure potential differences in an alkaline electrolysis cell, as both the calculated value for the conductivity was closer and the spread (standard deviation) between different, but identical, measurements was significantly smaller (5.69 vs 10.62 S/m). It must be noted that the effectiveness of both pseudoreference electrodes relied on the manner of measuring; after each individual set of parameters, a baseline potential value was recorded at 0 applied potential, from which the potential drop at non zero applied potential was subtracted. Recording solely the potential differences at each set of parameters (distance between wires) resulted in values far off from both theory as conductivity probe validation. With regard to the hydrogen reference electrodes, the results were both stable and reproducible. No potential jumps from baseline values were needed to measure stable potential differences. An electrolyte conductivity was measured at 7.5 % higher than the value measured with the conductivity probe, with a standard deviation between measurements of 2.76 S/m.

***Can hydrogen reference electrodes and pseudoreference electrodes like silver or copper wires be used to accurately measure the electrolyte potentials in the manifolds of a 5-cell electrolyser stack, If yes, can shunt currents be accurately inferred from those measurements?***

The experiments in Section 4.3 showed that hydrogen reference electrodes can effectively indicate shunt currents in the manifolds of the stack. Steady potential differences were measured while the stack was operational. These

potential differences reacted accordingly when parameters such as flow rate and applied current were changed. Alongside a mathematical model that calculates the manifold resistances at each set of parameters, values for shunt currents resulted that approached the theoretically expected value to a great extent. The measured values for the manifold shunt currents showed the same behaviour to varying parameters as the expected shunt current, but with consistently lower values. This can be ascribed to the positioning of the reference electrodes at either side of the manifolds. An average manifold shunt current can be calculated with the experiments performed, not a total shunt current.

The shunt current experiments laid out in Sections 4.3 and 4.4 showed poor performance for both copper and silver wires as pseudoreference electrodes to measure potential differences in a 5-cell stack. The potential differences measured were unstable and not reproducible. An explanation lies in the manner of how the potential differences were used. In the controlled test set-up, as explained in Section 4.1, the potential differences were measured and subtracted from a baseline value before each individual change of parameter (the distance between the wires). The baseline value was the potential difference measured when no potential was applied between the two electrodes. As mentioned in Section 4.1, that baseline value could vary, and not affect the potential difference measured. In the stack however, to measure actual shunt currents, it is not viable to use only the potential jumps between time intervals with changing parameters. The actual potential difference at each time interval had to be used to measure the actual shunt current. A reason for the poor reproducibility of the results is the lack of a stable redox potential for both. As the wires lack a stable and fixed redox potential, the potential difference measured could shift instantaneously during a measurement due to reactions taking place at the surfaces of the wire. Additionally, the wires were enclosed in the stack for more than a month, allowing corrosion to take place and cause more changes on the surfaces of the wires.

***Can a magnetic current clamp enclosed around the external wiring be used to accurately measure shunt currents in a 5-cell electrolyser stack with external wiring?***

The instantaneous current measurements along the external wiring of the electrolyser stack portrayed in Section 4.3 showed varying results. In the flow rate regime where the liquid flow rate and the gas flow rate were of the same order of magnitude, the current clamp data was accurate and approached the theoretically expected values closely. In the low flow rate regime and the high flow rate regime the measured values were consistently higher and showed a large spread over multiple iterations. This is likely due to the nature of how the experiments were performed; the clamp measurements are snap shots. At every flow rate regime, which were set for 10 minutes per setting, the current running through the four external wires was measured and subtracted from the current being supplied to the outermost electrodes. The clamp meters could not permanently enclose the wires and measure continuously. Due to the instantaneous nature of these measurements, a large spread is visible. Another possible explanation for the varying results is the contact between the wires and the electrodes. The wires were connected with M3 bolts and screws to the electrodes and pressed firmly together. As the wires and electrodes were connected and disconnected multiple times for small adaptations, it is very possible that small inconsistencies in the connections took place. If the contact between the wires and electrodes is inconsistent or intermittent, it could lead to fluctuating resistance levels. This can result in variable current flow, which might be averaged out or detected as lower with the current clamp (and thus a higher shunt current). Overall the magnetic current clamp measurements can be seen as a promising method to quantify shunt currents in electrolyser stacks with external wires. The resulting values were of the same order of magnitude as the expected values in nearly all cases.

***What is the influence of varying the current in an electrolyser stack on shunt currents?***

The variable current experiment discussed in Section 4.3.2 indicate the effect of increasing current density on the shunt currents in the stack. As the current density increases, the gas flow rate increases according to Equation (2.17). With gas flow rates higher than the liquid flow rate, gas bubbles coalesce at the top of the electrode compartments and block the outflow channels, this can be seen in Appendix E.3. This results in a blockage of the conductive pathways through the manifolds, leading to a decrease in shunt currents. Intuitively, the shunt current through the footer, not affected by gas bubbles, increases with increasing current density. This is substantiated by the results of the reference electrode measurements. The expected shunt current calculated with Equation (2.23), based on channel resistances at each gas and liquid flow rate setting, support the overall decrease in shunt current with increasing current density, for this stack design. A sidenote to the measured and calculated result is that they are specific to this stack design, with significantly higher channel resistances when compared to manifold resistances. As can be seen in Appendix C. The magnetic current clamp measurements show varying results again.

At first the values and slope of the graph is in line with the reference electrode, after which a sudden increase in shunt current is measured. This variation is largely due to the instantaneous measurement technique. Also, at current above 20 A (278 mA/cm<sup>2</sup>), the accuracy of the current meter declines. It must also be noted that a decrease in shunt currents does not necessarily mean an increase in efficiency of the stack; an accumulation of bubbles in the cell compartment also leads to a higher resistance in the electrode membrane gap, decreasing cell efficiency. This is however not quantified in this thesis.

### ***What is the influence of electrolyte flow rate variations in an electrolyser stack on shunt currents?***

Comparable to the results of the variable current measurements, the variable flow rate measurements describe the interplay of gas and liquid flow rate with regards to shunt currents. In situations where the liquid flow rate is considerably higher than the gas flow rates, a low void fraction leads to lower resistances in the channels and manifolds, leading to higher expected shunt currents and higher shunt currents measured with the reference electrodes. Also the magnetic current clamp measurements substantiate this. The images in Appendix E.1.1 and E.2.1 support the notable difference in homogeneity of the gas-liquid mixture. Liquid flow rates higher than gas flow rates lead to more homogeneity and small gas bubbles whereas liquid flow rates lower than gas flow rates lead to large bubbles and clogging of the channel. The expected shunt current and measured manifold shunt current with the reference electrodes reach a near constant value at a liquid flow rate of 240 mL/min, where the O<sub>2</sub> and H<sub>2</sub> flow rates are 39 and 78 mL/min, respectively. The magnetic current clamp measurements does not show a constant behaviour. Albeit the spread is again relatively large. Extreme cases where the entire electrode compartment top was filled gas were visible at liquid flow rates 100 times lower than gas flow rates, as can be seen in Figure E.1. This also resulted in a shunt current of zero through the top manifolds. It can also be seen that the shunt currents through the Anode header reach an equilibrium value at a lower flow rate when compared to the Cathode header shunt currents, in Figure 4.11. Which is in line with expectation, as the constant O<sub>2</sub> gas flow rate is half that of the H<sub>2</sub> flow rate. Images in Appendix E.2.1 also show larger gas bubbles at the Cathode side when compared to the Anode side, at similar flow rates.

## **5.2. Recommendations**

Recommendations for further research can be found below.

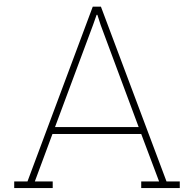
- A possible solution for the large spread in measurements with the magnetic current clamp could be a set-up where magnetic current clamps are permanently enclosing the four external wires. A continuous measurement can average out any inconsistencies.
- As explained through Figure 4.7, the set-up as it is right now gives an average manifold shunt current. The pseudoreference electrodes did not give stable potential measurements, a more complex set-up with hydrogen reference electrodes along the manifold can give more insight in the total shunt current measured. This will bring design challenges as the hydrogen reference electrodes need to be dismantled after measurements to be rinsed with water and then stored in electrolyte.
- Throughout the conducting of experiments with the stack, multiple problems arose with the external wires. The external wires consisted of two parallel 2.5 mm copper wires connected on both sides with cable lugs. The cable lugs were connected with the electrodes with M3 bolts and screws, in combination with wires monitoring the cell potentials and the wires connecting the outermost electrodes with the power supply. This resulted in a situation where inconsistencies in the connections took place, sometimes resulting in over heating and even melting of the wires. This only happened at high potentials. A solution could be to use a single, thicker wire with a better connection to the cable lugs. In turn, connecting the cable lugs more firmly to the electrodes. the distance between electrode flaps sticking out the side of the stack resulted in a narrow working environment, where it was difficult to realize a tight connection. A set-up where the distance between electrodes is larger, creating more space to tighten the bolts would work better. Using double wires is not advised for future research.
- Difficulties arose with realizing a zero-gap configuration of the corrugated electrodes and membrane. As the Zirfon Perl membrane is quite rigid, cracks occurred multiple times during the corrugation process with the 3D printed molds. Additionally, the Zirfon would not permanently remain its corrugated shape after pressing, resulting in small gaps between the electrodes and the membrane. Heating of the Zirfon prior to corrugating might work to make it more flexible. The 3D printed molds were also not ideal, as they cracked under high pressure. Creating molds of a more rigid and stress resistant material will solve this problem.

# References

- [1] H. Ritchie, P. Rosado, and M. Roser, “Energy production and consumption,” *Our World in Data*, 2020, <https://ourworldindata.org/energy-production-consumption>.
- [2] M. Denchak, *Are the effects of global warming really that bad?* <https://www.nrdc.org/stories/are-effects-global-warming-really-bad>, Accessed: [January 12 2024], Natural Resources Defense Council, 2022.
- [3] *The causes and effects of climate change*, <https://www.un.org/en/climatechange/science/causes-effects-climate-change>, Accessed: [12 January 2024], United Nations, n.d.
- [4] P. Tans and R. Keeling, *Trends in atmospheric carbon dioxide*, <https://gml.noaa.gov/ccgg/trends/> and <https://scrippsco2.ucsd.edu/>, Accessed: [12 January 2024], NOAA/GML and Scripps Institution of Oceanography.
- [5] J. Mitali, S. Dhinakaran, and A. Mohamad, “Energy storage systems: A review,” *Energy Storage and Saving*, vol. 1, no. 3, pp. 166–216, 2022, ISSN: 2772-6835. DOI: <https://doi.org/10.1016/j.enss.2022.07.002>. [Online]. Available: <https://www.sciencedirect.com/science/article/pii/S277268352200022X>.
- [6] A. Keçebaş, M. Kayfeci, and M. Bayat, “Chapter 9 - electrochemical hydrogen generation,” in *Solar Hydrogen Production*, F. Calise, M. D. D’Accadia, M. Santarelli, A. Lanzini, and D. Ferrero, Eds., Academic Press, 2019, pp. 299–317, ISBN: 978-0-12-814853-2. DOI: <https://doi.org/10.1016/B978-0-12-814853-2.00009-6>. [Online]. Available: <https://www.sciencedirect.com/science/article/pii/B9780128148532000096>.
- [7] M. David, C. Ocampo-Martínez, and R. Sánchez-Peña, “Advances in alkaline water electrolyzers: A review,” *Journal of Energy Storage*, vol. 23, pp. 392–403, 2019, ISSN: 2352-152X. DOI: <https://doi.org/10.1016/j.est.2019.03.001>. [Online]. Available: <https://www.sciencedirect.com/science/article/pii/S2352152X18306558>.
- [8] E. B. Agyekum, C. Nutakor, A. M. Agwa, and S. Kamel, “A critical review of renewable hydrogen production methods: Factors affecting their scale-up and its role in future energy generation,” *Membranes*, vol. 12, no. 2, 2022, ISSN: 2077-0375. DOI: 10.3390/membranes12020173. [Online]. Available: <https://www.mdpi.com/2077-0375/12/2/173>.
- [9] A. Ursua, L. M. Gandia, and P. Sanchis, “Hydrogen production from water electrolysis: Current status and future trends,” *Proceedings of the IEEE*, vol. 100, no. 2, pp. 410–426, 2012. DOI: 10.1109/JPROC.2011.2156750.
- [10] C. Li and J.-B. Baek, “The promise of hydrogen production from alkaline anion exchange membrane electrolyzers,” *Nano Energy*, vol. 87, p. 106162, 2021, ISSN: 2211-2855. DOI: <https://doi.org/10.1016/j.nanoen.2021.106162>. [Online]. Available: <https://www.sciencedirect.com/science/article/pii/S2211285521004183>.
- [11] R. Chaubey, S. Sahu, O. O. James, and S. Maity, “A review on development of industrial processes and emerging techniques for production of hydrogen from renewable and sustainable sources,” *Renewable and Sustainable Energy Reviews*, vol. 23, no. C, pp. 443–462, 2013. DOI: 10.1016/j.rser.2013.02.01. [Online]. Available: <https://ideas.repec.org/a/eee/rensus/v23y2013icp443-462.html>.
- [12] H. Rajaei and J. Haverkort, “Compact monopolar electrochemical stack designs using electrode arrays or corrugated electrodes,” *Electrochimica Acta*, vol. 332, p. 135470, 2020, ISSN: 0013-4686. DOI: <https://doi.org/10.1016/j.electacta.2019.135470>. [Online]. Available: <https://www.sciencedirect.com/science/article/pii/S0013468619323424>.
- [13] M. C. Pektas, “Slug flow characterization in an alkaline water electrolyser for hydrogen production,” 2023.
- [14] A. T. Kuhn and J. S. Booth, “Electrical leakage currents in bipolar cell stacks,” *Journal of Applied Electrochemistry*, vol. 10, pp. 233–237, 1980. [Online]. Available: <https://api.semanticscholar.org/CorpusID:94770901>.

- [15] A. Hodges, A. L. Hoang, G. Tsekouras, *et al.*, “A high-performance capillary-fed electrolysis cell promises more cost-competitive renewable hydrogen,” *Nature Communications*, vol. 13, no. 1, p. 1304, Mar. 15, 2022, ISSN: 2041-1723. DOI: 10.1038/s41467-022-28953-x. [Online]. Available: <https://doi.org/10.1038/s41467-022-28953-x>.
- [16] D. Santos, C. Sequeira, and J. Figueiredo, “Hydrogen production by alkaline water electrolysis,” *Química Nova*, vol. 36, pp. 1176–1193, Dec. 2012. DOI: 10.1590/S0100-40422013000800017.
- [17] J. Brauns, J. Schönebeck, M. R. Kraglund, *et al.*, “Evaluation of diaphragms and membranes as separators for alkaline water electrolysis,” *Journal of The Electrochemical Society*, vol. 168, no. 1, p. 014 510, Jan. 2021. DOI: 10.1149/1945-7111/abda57. [Online]. Available: <https://dx.doi.org/10.1149/1945-7111/abda57>.
- [18] I. Firtina-Ertis, “Thermodynamic and electrochemical assessment of an alkaline electrolyzer (ae) at different operating parameters,” *Journal of Environmental Chemical Engineering*, vol. 10, no. 2, p. 107 225, 2022, ISSN: 2213-3437. DOI: <https://doi.org/10.1016/j.jece.2022.107225>. [Online]. Available: <https://www.sciencedirect.com/science/article/pii/S2213343722000987>.
- [19] A. Buttler and H. Spliethoff, “Current status of water electrolysis for energy storage, grid balancing and sector coupling via power-to-gas and power-to-liquids: A review,” *Renewable and Sustainable Energy Reviews*, vol. 82, pp. 2440–2454, 2018, ISSN: 1364-0321. DOI: <https://doi.org/10.1016/j.rser.2017.09.003>. [Online]. Available: <https://www.sciencedirect.com/science/article/pii/S136403211731242X>.
- [20] C. Priest, J. Gomez, N. Kane, *et al.*, “Challenges in practical button cell testing for hydrogen production from high temperature electrolysis of water,” *Frontiers in Energy Research*, vol. 11, Sep. 2023. DOI: 10.3389/fenrg.2023.1278203.
- [21] K. Zeng and D. Zhang, “Recent progress in alkaline water electrolysis for hydrogen production and applications,” *Progress in Energy and Combustion Science*, vol. 36, no. 3, pp. 307–326, 2010, ISSN: 0360-1285. DOI: <https://doi.org/10.1016/j.peccs.2009.11.002>. [Online]. Available: <https://www.sciencedirect.com/science/article/pii/S0360128509000598>.
- [22] R. Kortlever, *Electrochemical energy storage 1*, 4-EES-ME45201-Thermodynamics, Delft University of Technology, 2021.
- [23] J. Hnát, M. Paidar, and K. Bouzek, “5 - hydrogen production by electrolysis,” in *Current Trends and Future Developments on (Bio-) Membranes*, A. Iulianelli and A. Basile, Eds., Elsevier, 2020, pp. 91–117, ISBN: 978-0-12-817384-8. DOI: <https://doi.org/10.1016/B978-0-12-817384-8.00005-4>. [Online]. Available: <https://www.sciencedirect.com/science/article/pii/B9780128173848000054>.
- [24] R. Phillips and C. Dunnill, “Zero gap alkaline electrolysis cell designs for renewable energy storage as hydrogen gas,” *RSC Adv*, vol. 6, pp. 100 643–100 651, Oct. 2016. DOI: 10.1039/C6RA22242K.
- [25] R. Qi, M. Becker, J. Brauns, T. Turek, J. Lin, and Y. Song, “Channel design optimization of alkaline electrolysis stacks considering the trade-off between current efficiency and pressure drop,” *Journal of Power Sources*, vol. 579, p. 233 222, 2023, ISSN: 0378-7753. DOI: <https://doi.org/10.1016/j.jpowsour.2023.233222>. [Online]. Available: <https://www.sciencedirect.com/science/article/pii/S0378775323005980>.
- [26] R. Jupudi, G. Zappi, and R. Bourgeois, “Prediction of shunt currents in a bipolar electrolyzer stack by difference calculus,” *Journal of Applied Electrochemistry*, vol. 37, pp. 921–931, Aug. 2007. DOI: 10.1007/s10800-007-9330-4.
- [27] M. Katz, “Analysis of electrolyte shunt currents in fuel cell power plants,” *Journal of The Electrochemical Society*, vol. 125, no. 4, p. 515, Apr. 1978. DOI: 10.1149/1.2131488. [Online]. Available: <https://dx.doi.org/10.1149/1.2131488>.
- [28] B. Tjaden, S. J. Cooper, D. J. Brett, D. Kramer, and P. R. Shearing, “On the origin and application of the bruggeman correlation for analysing transport phenomena in electrochemical systems,” *Current Opinion in Chemical Engineering*, vol. 12, pp. 44–51, 2016, Nanotechnology / Separation Engineering, ISSN: 2211-3398. DOI: <https://doi.org/10.1016/j.coche.2016.02.006>. [Online]. Available: <https://www.sciencedirect.com/science/article/pii/S2211339816300119>.
- [29] J. Burnett and D. Danly, “Current bypass in electrochemical cell assemblies,” 75, pp. 8–13, 1979.

- [30] G. Inzelt, A. Lewenstam, and F. Scholz, *Handbook of reference electrodes*. Springer, 2013, vol. 541.
- [31] A. Bard and L. Faulkner, *Electrochemical Methods: Fundamentals and Applications*. Wiley, 2000, ISBN: 9780471043720. [Online]. Available: <https://books.google.nl/books?id=kv56QgAACAAJ>.
- [32] Gaskatel. [Online]. Available: <https://gaskatel.de/en/shop/mini-hydrogen-reference-electrode-mini-hydroflex/>.
- [33] R. Gilliam, J. Graydon, D. Kirk, and S. Thorpe, "A review of specific conductivities of potassium hydroxide solutions for various concentrations and temperatures," *International Journal of Hydrogen Energy*, vol. 32, no. 3, pp. 359–364, 2007, Fuel Cells, ISSN: 0360-3199. DOI: <https://doi.org/10.1016/j.ijhydene.2006.10.062>. [Online]. Available: <https://www.sciencedirect.com/science/article/pii/S0360319906005428>.
- [34] H. Luo, X. Ji, and S. Cheng, "Investigation into the electrochemical behaviour of silver in alkaline solution and the influence of au-decoration using operando raman spectroscopy," *RSC Adv.*, vol. 10, pp. 8453–8459, 14 2020. DOI: 10.1039/C9RA10282E. [Online]. Available: <http://dx.doi.org/10.1039/C9RA10282E>.
- [35] *Vc-330 ac/dc mini current clamp operating instructions*, 03/2015, Item No. 1307544, Voltcraft, Germany.



# Electrochemical stability copper and silver

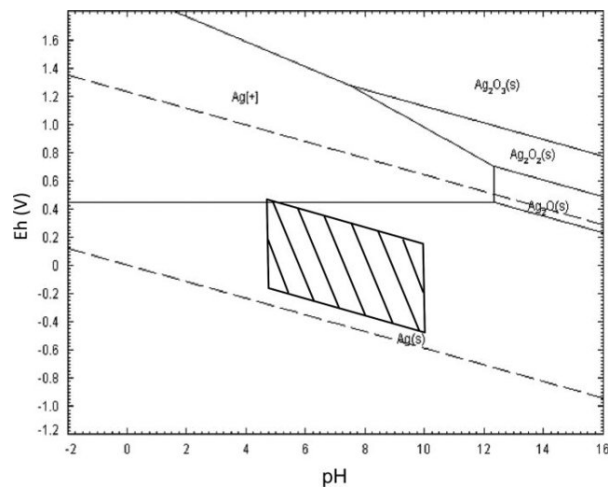


Figure A.1: The Pourbaix diagram of silver

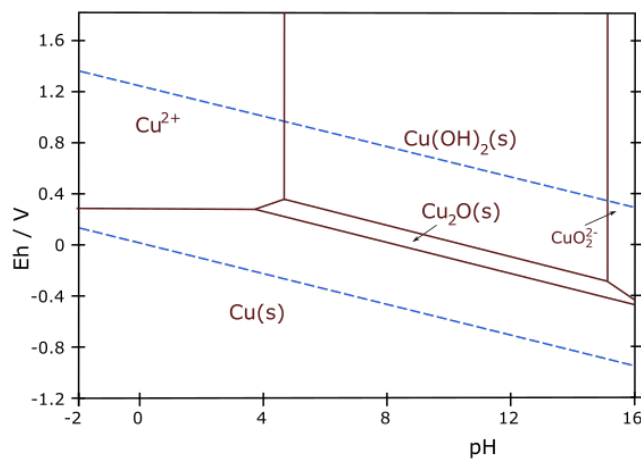
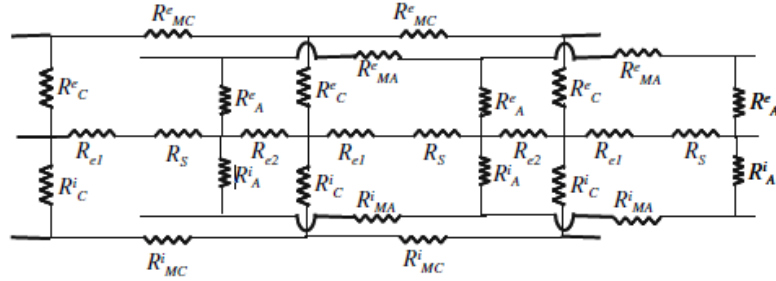


Figure A.2: The Pourbaix diagram of copper

# B

## Shunt currents

In [26], a model is developed to calculate and approximate shunt currents in bipolar electrolyser stacks that can serve as a tool to design such a stack. The electrolyser stack is represented in the form of an equivalent circuit of resistances. Figure B.1 shows the resistance components of an N-cell assembly.



**Figure B.1:** Resistance components in a circuit analog of an N-cell assembly. Retrieved from [26]

Resistances  $R_{e1}$  and  $R_{e2}$  are Ohmic resistances in the cathodic and anodic electrolytes respectively and  $R_S$  represents the resistance due to the membrane separating the anodic and cathodic channels. The resistances are given by:

$$R_{e1} = \frac{\rho L_C}{A_e} \left( \frac{1 + \alpha_C/2}{1 - \alpha_C} \right) \quad (\text{B.1})$$

$$R_{e2} = \frac{\rho L_A}{A_e} \left( \frac{1 + \alpha_A/2}{1 - \alpha_A} \right) \quad (\text{B.2})$$

$$R_S = \frac{\rho N_M L_S}{A_e} \quad (\text{B.3})$$

Where  $N_M$  is the McMullin number, defined as the ratio of the tortuosity to the porosity of the membrane. In this model, the inlet and outlet ports are assumed to be trapezoidal in shape. This leads to the following expression for the resistances in the inlet/outlet ports:

$$R_C^i = R_A^i = \frac{\rho}{2d \tan(\theta/2)} [\ln(h_2/h_1)] \quad (\text{B.4})$$

$$R_C^e = R_C^i \frac{1 + \alpha_{eC}/2}{1 - \alpha_{eC}} \quad (\text{B.5})$$

and

$$R_A^e = R_A^i \frac{1 + \alpha_{eA}/2}{1 - \alpha_{eA}} \quad (\text{B.6})$$

The resistances in the inlet/outlet manifold are computed as follows:

$$R_{MC}^i = R_{MA}^i = \frac{\rho L_M}{(\pi h_1^2/4)} \quad (\text{B.7})$$

$$R_{MC}^e = R_{MC}^i \left( \frac{1 + \alpha_{eC}/2}{1 - \alpha_{eC}} \right) \quad (\text{B.8})$$

$$R_{MA}^e = R_{MA}^i \left( \frac{1 + \alpha_{eA}/2}{1 - \alpha_{eA}} \right) \quad (\text{B.9})$$



# Dimensions, resistances and void fractions

## C.1. Stack dimensions

In the tables below, Header 1-4 and Footer 1-4 indicate the distance between two adjacent pseudoreference electrodes in the cathode and anode header and the footer. RE is the distance between the reference electrodes in the respective header/footer. The radius is the same for all three manifolds.

**Table C.1:** The dimensions of the cathode header

Cathode header	Dimension
Header 1	0.013 m
Header 2	0.011 m
Header 3	0.012 m
Header 4	0.012 m
RE	0.08 m
Radius	0.006m

**Table C.2:** The dimensions of the anode header

Anode header	Dimension
Header 1	0.012 m
Header 2	0.012 m
Header 3	0.011 m
Header 4	0.013 m
RE	0.08 m
Radius	0.006m

**Table C.3:** The dimensions of the footer

Footer	Dimension
Footer 1	0.012 m
Footer 2	0.012 m
Footer 3	0.011 m
Footer 4	0.013 m
RE	0.08 m
Radius	0.006m

**Table C.4:** The dimensions of the electrode compartment. Components are visualized in Figure C.1.

Cell	Dimension
Distance bottom-halfway electrode	0.08 m
Depth	0.006 m
Width	0.082 m
Total Height	0.2 m
Actual height	0.1605 m

**Table C.5:** The dimensions of the channels between manifolds and electrode compartment. Components are visualized in Figure C.1. Depth is the distance between the walls of the channel perpendicular to the screen.

Channel	Dimension
Curved section	0.0284 m
Straight section	0.014 m
Depth channel	0.006 m
Width channel	0.002 m

**Table C.6:** The dimensions of the electrode.

Cell	Dimension
Area electrode	0.0072 $m^2$
Width electrode	0.08 m
length electrode	0.092 m
Width flap	0.007 m
Length flap	0.07 m
Thickness electrode	0.0005 m

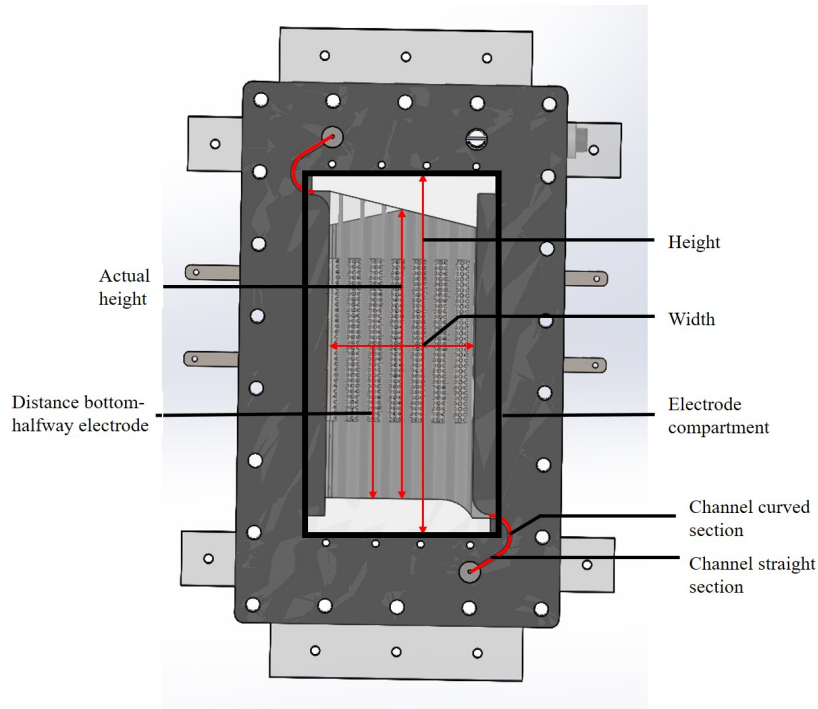


Figure C.1: Indications of the electrode compartment components listed in Table C.4.

## C.2. Stack resistances

The conductivity of the electrolyte used to calculate manifold and channel resistances is measured with a conductivity probe and is 59.8 S/m. The resistances below are calculate according to Equation (C.1), where the length of the manifold is chosen to be distance between the channel of Cell 1 to Cell 5, not the distance between the reference electrodes, as they are placed outside of the channels.

$$R = \frac{L}{\sigma A} \quad (\text{C.1})$$

This resulted in the manifold and channel resistances, without bubble interference accounted for yet, shown in Table C.7.

Stack section	Resistance ( $\Omega$ )
Manifold	7.10
Channel	59.1

Table C.7: Manifold and channel resistance. No void fractions included yet.

The eventual resistance values of the manifolds and channels were calculated based on the Bruggeman Equation and Equations for gas flow rates given below.

$$R_{\text{actual}} = R * (1 - \alpha_{\text{ch/m}})^{-1.5} \quad (\text{C.2})$$

$$\alpha_{\text{ch/m}} = \frac{q_{\text{g}}}{q_{\text{g}} + q_{\text{liq}}} \quad (\text{C.3})$$

$$\bar{q}_{\text{H}_2} = \left( \frac{I_0}{2\mathcal{F}} \right) \frac{R_{\text{g}}T}{P_0} \quad (\text{C.4})$$

$$\bar{q}_{\text{O}_2} = \left( \frac{I_0}{4\mathcal{F}} \right) \frac{R_{\text{g}}T}{P_0} \quad (\text{C.5})$$

This resulted in a separate void fraction, and thus resistance value for both Cathode header and Anode header. The Footer, not being affected by bubbles, maintained resistance values given in Table C.7. All experiments were conducted at atmospheric pressure and room temperature. All void fractions and calculated resistances per flow rate and current density regime are given below.

<b>Constant current 20 A (278 mA/cm<sup>2</sup>)</b>			
<b>liquid flow rate per cell (mL/min)</b>	<b>Void fraction</b>	<b>Cathode channel resistance (Ω)</b>	<b>Cathode manifold resistance (Ω)</b>
0.596	0.99620988	253163.4927	30416.42519
1.192	0.992448381	90016.15547	10815.02562
1.788	0.98871518	49276.36459	5920.327773
2.98	0.981332408	23160.51045	2782.628434
5.96	0.963349001	8418.832483	1011.483866
11.92	0.929289609	3141.635026	377.4529483
23.84	0.867918736	1230.605248	147.8515408
47.68	0.766657627	524.0710549	62.96471842

**Table C.8:** Cathode void fractions and resistances estimated from a constant current of 20 A and a low flow rate regime

<b>Constant current 20 A (278 mA/cm<sup>2</sup>)</b>			
<b>liquid flow rate per cell (mL/min)</b>	<b>Void fraction</b>	<b>Anode channel resistance (Ω)</b>	<b>Anode manifold resistance (Ω)</b>
0.596	0.992448381	90016.15547	10815.02562
1.192	0.985009961	32186.69799	3867.083208
1.788	0.977682213	17717.55944	2128.682992
2.98	0.963349001	8418.832483	1011.483866
5.96	0.929289609	3141.635026	377.4529483
11.92	0.867918736	1230.605248	147.8515408
23.84	0.766657627	524.0710549	62.96471842
47.68	0.621609737	253.787752	30.49142705

**Table C.9:** Anode void fractions and resistances estimated from a constant current of 20 A and a low flow rate regime

<b>Constant current 10 A (139 mA/cm<sup>2</sup>)</b>			
<b>liquid flow rate per cell (mL/min)</b>	<b>Void fraction</b>	<b>Cathode channel resistance (Ω)</b>	<b>Cathode manifold resistance (Ω)</b>
11.72	0.869846427	1258.045787	151.1483949
23.44	0.769670997	534.3891694	64.20439226
35.26	0.690186064	342.5540948	41.15629345
46.88	0.625581447	257.8365888	30.97787611
58.6	0.572036205	210.9939694	25.3499516
70.32	0.527005339	181.5917989	21.81741651
82.04	0.48842493	161.4420002	19.39651119
93.76	0.455160799	146.8852095	17.64757998
105.48	0.426138667	135.88457	16.32590392
117.2	0.400595734	127.2919219	15.29353691

**Table C.10:** Cathode void fractions and resistances estimated from a constant current of 10 A and a mid flow rate regime

<b>Constant current 10 A (139 mA/cm<sup>2</sup>)</b>			
<b>liquid flow rate per cell (mL/min)</b>	<b>Void fraction</b>	<b>Anode channel resistance (Ω)</b>	<b>Anode manifold resistance (Ω)</b>
11.72	0.769670997	534.3891694	64.20439226
23.44	0.625581447	257.8365888	30.97787611
35.26	0.526934433	181.5509728	21.81251145
46.88	0.455160799	146.8852095	17.64757998
58.6	0.400595734	127.2919219	15.29353691
70.32	0.357778174	114.776505	13.78986733
82.04	0.323123171	106.0757514	12.74451195
93.76	0.294633123	99.71442642	11.98022811
105.48	0.270759983	94.85819342	11.39677413
117.2	0.250465591	91.03181994	10.93705301

**Table C.11:** Anode void fractions and resistances estimated from a constant current of 10 A and a mid flow rate regime

<b>Constant current 10 A (139 mA/cm<sup>2</sup>)</b>			
<b>liquid flow rate per cell (mL/min)</b>	<b>Void fraction</b>	<b>Cathode channel resistance (Ω)</b>	<b>Cathode manifold resistance (Ω)</b>
68.4	0.533829625	185.5938504	22.29824452
133	0.370645001	118.3142511	14.2149112
240	0.246059413	90.23497516	10.84131579
368.6	0.175257678	78.86842465	9.475677209
475.8	0.141352802	74.2435026	8.920014171

**Table C.12:** Cathode void fractions and resistances estimated from a constant current of 10 A and a high flow rate regime

<b>Constant current 10 A (139 mA/cm<sup>2</sup>)</b>			
<b>liquid flow rate per cell (mL/min)</b>	<b>Void fraction</b>	<b>Anode channel resistance (Ω)</b>	<b>Anode manifold resistance (Ω)</b>
68.4	0.364097948	116.4917712	13.99594864
133	0.227479586	86.99927662	10.45256155
240	0.14028948	74.10580453	8.903470383
368.6	0.096045165	68.73223878	8.257861259
475.8	0.076051443	66.5133621	7.991273468

**Table C.13:** Anode void fractions and resistances estimated from a constant current of 10 A and a high flow rate regime

<b>Constant flow rate 70 mL/min per cell</b>			
<b>Applied current density (mA/cm<sup>2</sup>)</b>	<b>Void fraction</b>	<b>Cathode channel resistance (Ω)</b>	<b>Cathode manifold resistance (Ω)</b>
69.4	0.357712816	114.7589865	13.78776256
104.2	0.455160799	146.8852095	17.64757998
138.9	0.526934433	181.5509728	21.81251145
173.6	0.581999188	218.5822539	26.26164895
208.3	0.625581447	257.8365888	30.97787611
243.1	0.66093371	299.194542	35.94684331
277.8	0.690186064	342.5540948	41.15629345
312.5	0.714791896	387.826781	46.59559774
347.2	0.735776848	434.9349265	52.25542401

**Table C.14:** Anode void fractions and resistances estimated from a constant flow rate of 70 mL/min per cell and a variable current density

<b>Constant flow rate 70 mL/min per cell</b>			
<b>Applied current density (mA/cm<sup>2</sup>)</b>	<b>Void fraction</b>	<b>Anode channel resistance (Ω)</b>	<b>Anode manifold resistance (Ω)</b>
69.4	0.217813803	85.39164225	10.2594117
104.2	0.294633123	99.71442642	11.98022811
138.9	0.357712816	114.7589865	13.78776256
173.6	0.410436428	130.4922218	15.67803817
208.3	0.455160799	146.8852095	17.64757998
243.1	0.493578036	163.9123923	19.69331741
277.8	0.526934433	181.5509728	21.81251145
312.5	0.556168214	199.7804491	24.00269889
347.2	0.581999188	218.5822539	26.26164895

**Table C.15:** Anode void fractions and resistances estimated from a constant flow rate of 70 mL/min per cell and a variable current density

# D

## (Pseudo)reference electrodes results

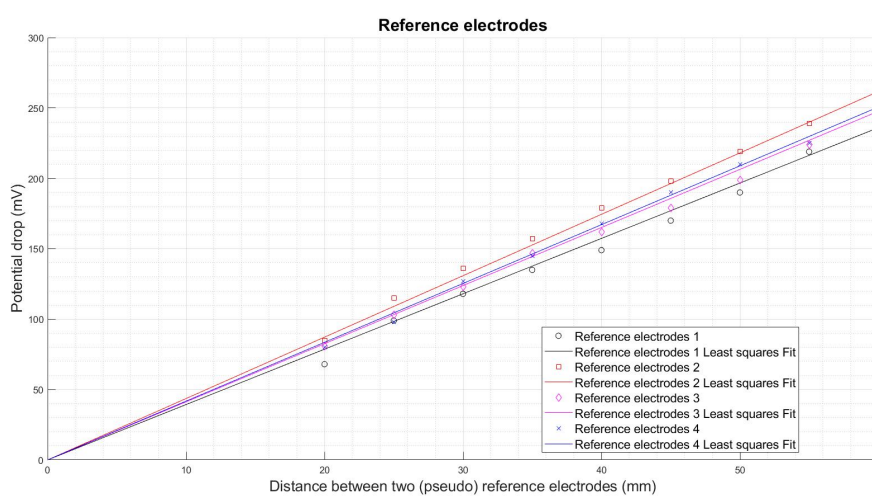


**Figure D.1:** Potential difference between two hydrogen reference electrodes vs the distance between them in the controlled test cell for (pseudo)reference electrode validation.

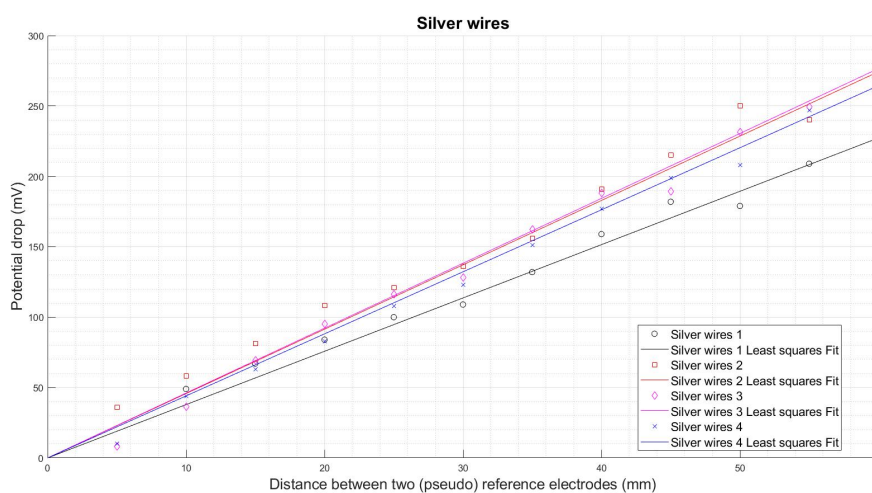


**Figure D.2:** Potential difference between two silver pseudoreference electrodes vs the distance between them in the controlled test cell for (pseudo)reference electrode validation.

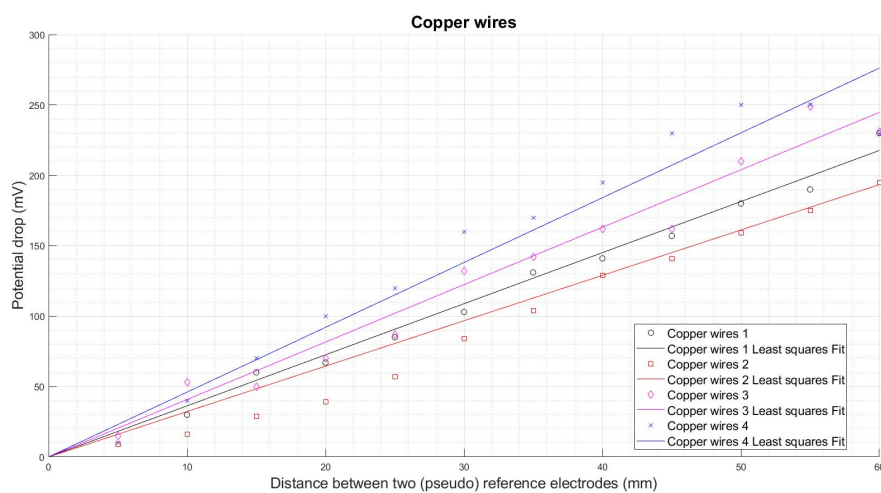


**Figure D.3:** Potential difference between two copper pseudoreference electrodes vs the distance between them in the controlled test cell for (pseudo)reference electrode validation.

## D.1. raw data reference electrodes

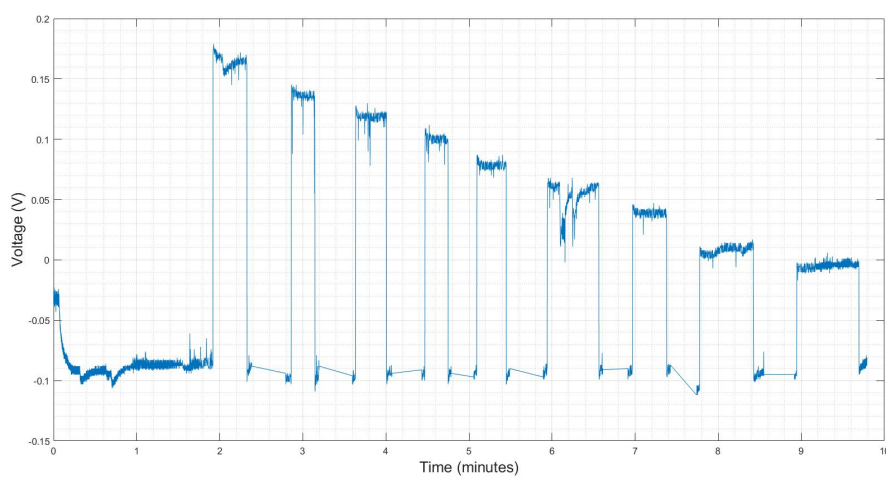


**Figure D.4:** Potential drop versus distance measurement for the reference electrodes. Each voltage jump at a specific time interval indicates a different distance between the reference electrodes. The first step is at 60 mm and the last step is at 20 mm. The distance is decreased by increments of 5 mm.

# E

## Images of the anode and cathode compartment at different flow rate regimes

All liquid flow rate values below are the flow rates per cell, for each cell.

**E.1. Constant gas flow rate: O<sub>2</sub>: 78 mL/min, H<sub>2</sub>: 157 mL/min**

**E.1.1. Liquid flow rate regime: 0.596 - 47.68 mL/min**

Cathode side

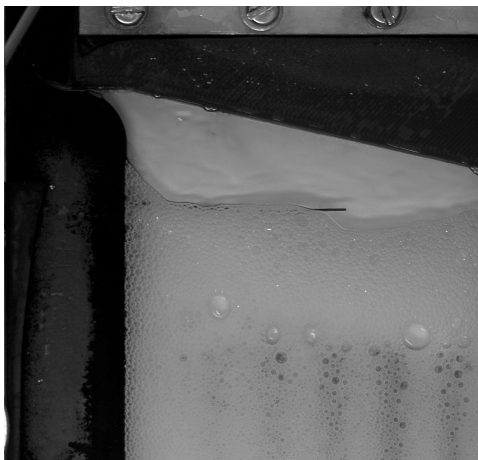


**Figure E.1:** Image of the Cathode side at liquid flow rate: 0.596 mL/min

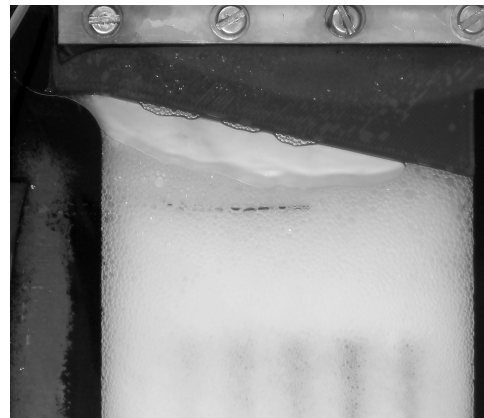


**Figure E.2:** Image of the Cathode side at liquid flow rate: 1.192 mL/min

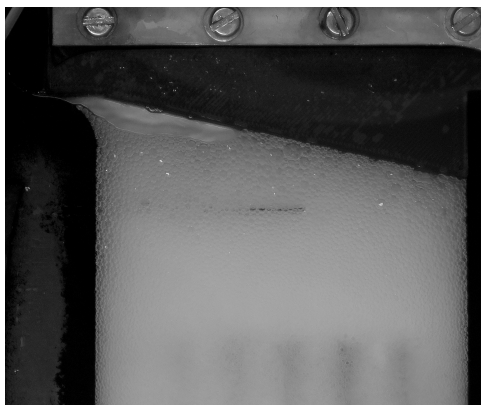


**Figure E.3:** Image of the Cathode side at liquid flow rate: 1.788 mL/min

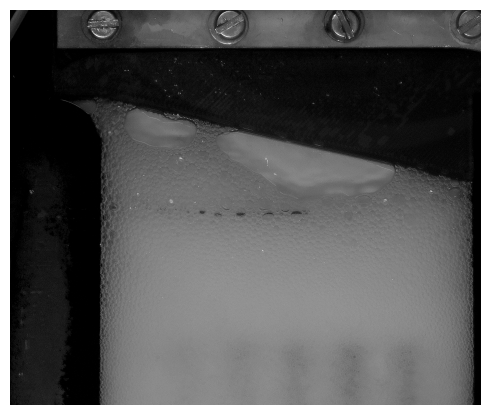


**Figure E.4:** Image of the Cathode side at liquid flow rate: 2.98 mL/min

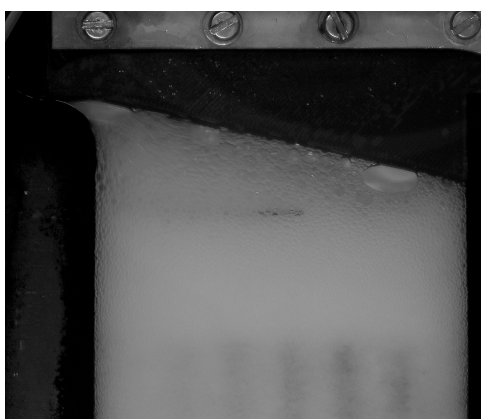


**Figure E.5:** Image of the Cathode side at liquid flow rate: 5.96 mL/min

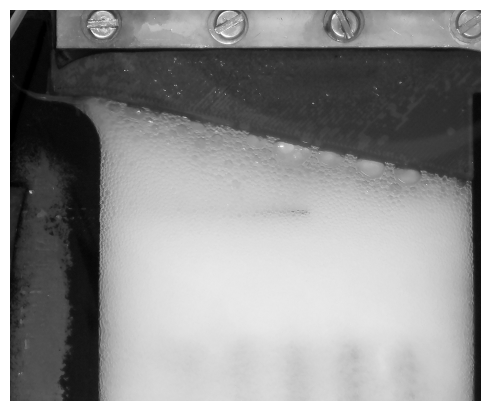


**Figure E.6:** Image of the Cathode side at liquid flow rate: 11.92 mL/min



**Figure E.7:** Image of the Cathode side at liquid flow rate: 23.84 mL/min

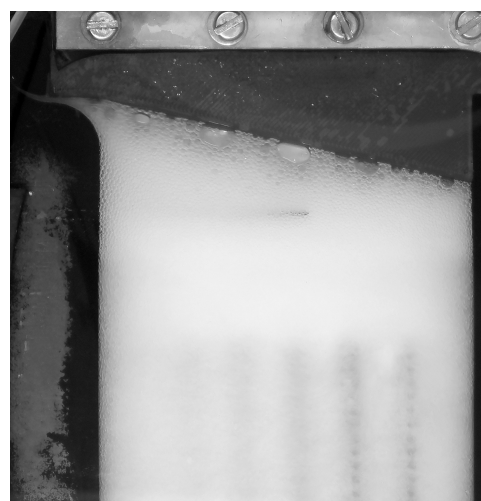


**Figure E.8:** Image of the Cathode side at liquid flow rate: 47.68 mL/min

Anode side

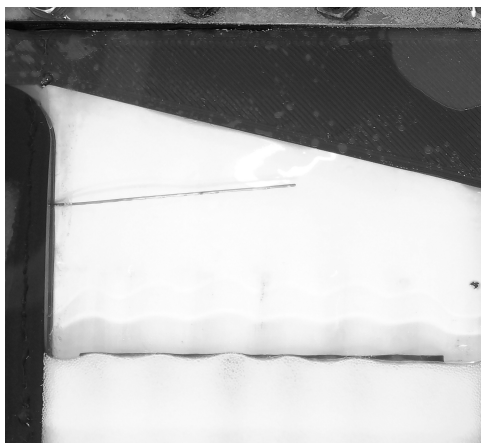


**Figure E.9:** Image of the Anode side at liquid flow rate: 0.596 mL/min

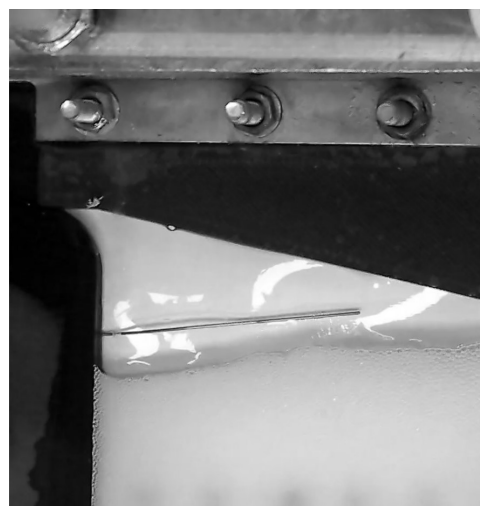


**Figure E.10:** Image of the Anode side at liquid flow rate: 1.192 mL/min

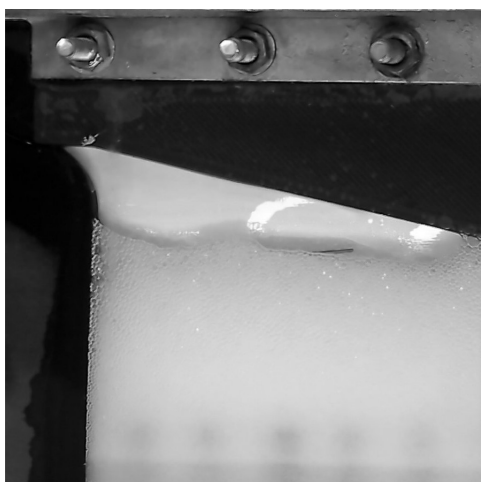


**Figure E.11:** Image of the Anode side at liquid flow rate: 1.788 mL/min

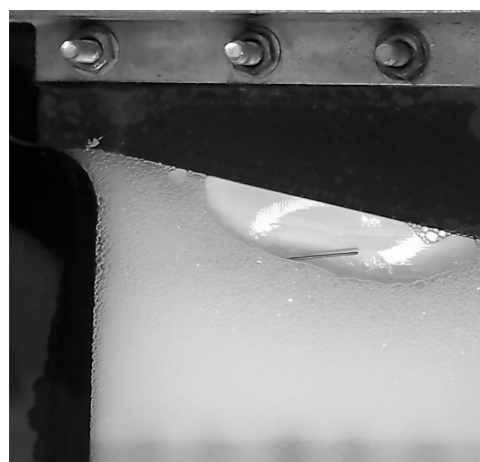


**Figure E.12:** Image of the Anode side at liquid flow rate: 2.98 mL/min

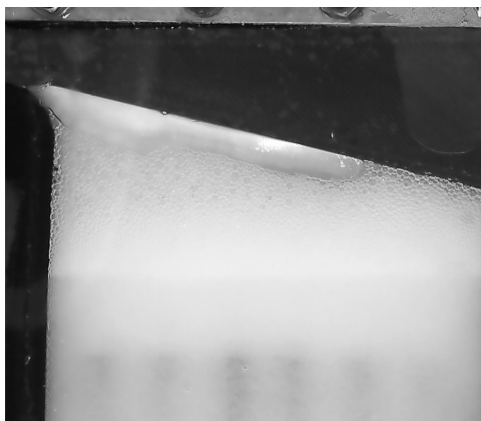


**Figure E.13:** Image of the Anode side at liquid flow rate: 5.96 mL/min



**Figure E.14:** Image of the Anode side at liquid flow rate: 11.92 mL/min



**Figure E.15:** Image of the Anode side at liquid flow rate: 23.84 mL/min

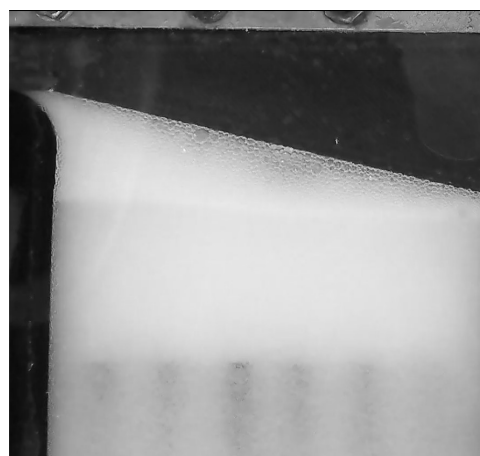


**Figure E.16:** Image of the Anode side at liquid flow rate: 47.68 mL/min

## E.2. Constant gas flow rate: O<sub>2</sub>: 39 mL/min, H<sub>2</sub>: 78 mL/min

### E.2.1. Liquid flow rate regime: 11.72 - 117.2 mL/min

Cathode side



**Figure E.17:** Image of the Cathode side at liquid flow rate: 11.72 mL/min



**Figure E.18:** Image of the Cathode side at liquid flow rate: 23.44 mL/min

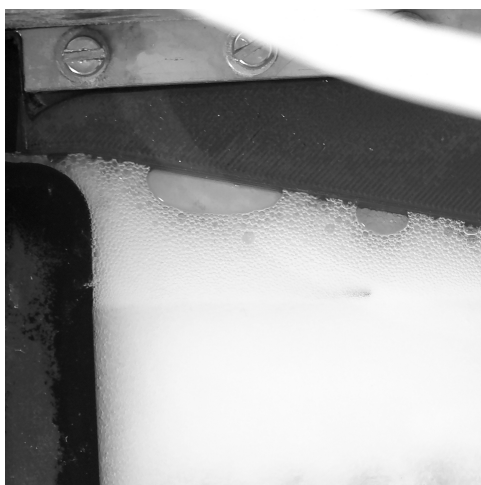


**Figure E.19:** Image of the Cathode side at liquid flow rate: 35.16 mL/min



**Figure E.20:** Image of the Cathode side at liquid flow rate: 46.88 mL/min



**Figure E.21:** Image of the Cathode side at liquid flow rate: 58.60 mL/min



**Figure E.22:** Image of the Cathode side at liquid flow rate: 70.32 mL/min



**Figure E.23:** Image of the Cathode side at liquid flow rate: 82.04 mL/min



**Figure E.24:** Image of the Cathode side at liquid flow rate: 93.76 mL/min



**Figure E.25:** Image of the Cathode side at liquid flow rate: 105.48 mL/min

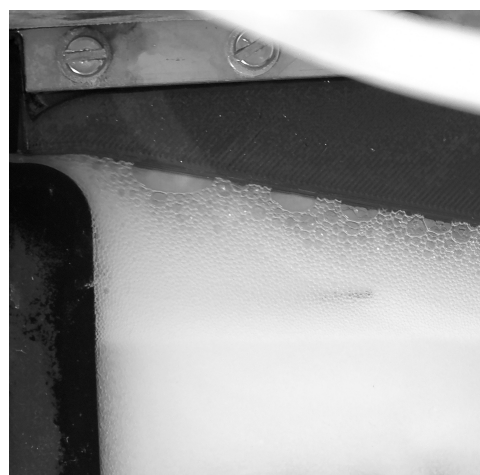


**Figure E.26:** Image of the Cathode side at liquid flow rate: 117.2 mL/min

Anode side

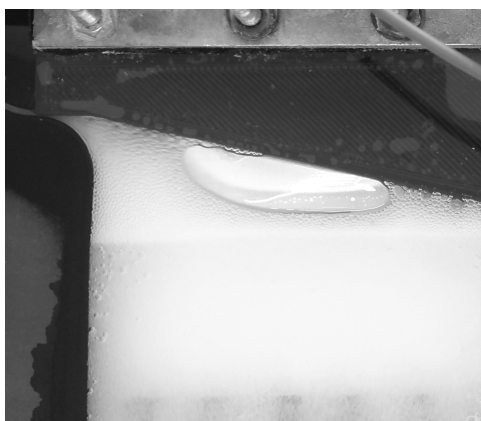


**Figure E.27:** Image of the Anode side at liquid flow rate: 11.72 mL/min

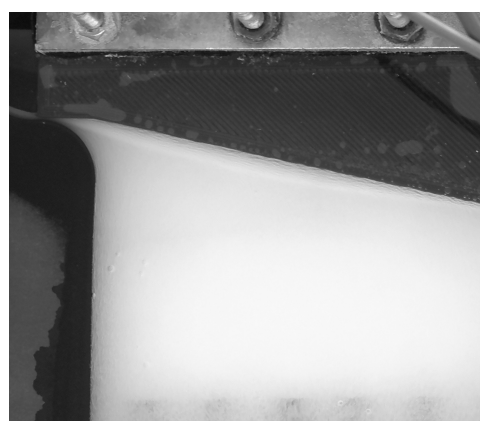


**Figure E.28:** Image of the Anode side at liquid flow rate: 23.44 mL/min

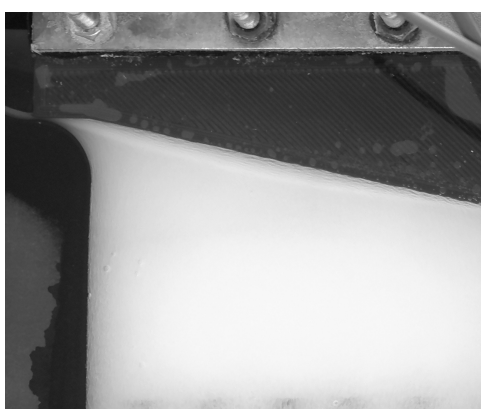


**Figure E.29:** Image of the Anode side at liquid flow rate: 35.16 mL/min

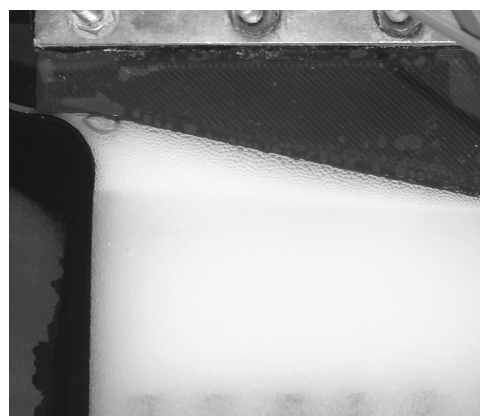


**Figure E.30:** Image of the Anode side at liquid flow rate: 46.88 mL/min

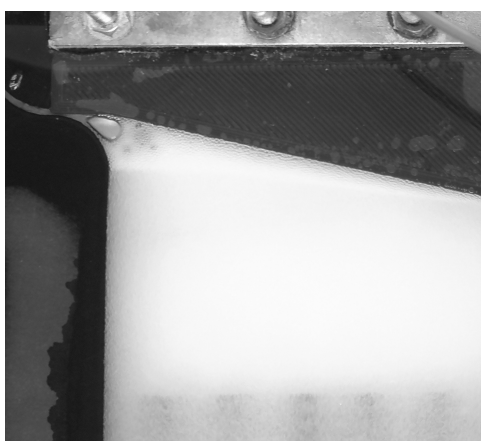


**Figure E.31:** Image of the Anode side at liquid flow rate: 58.60 mL/min

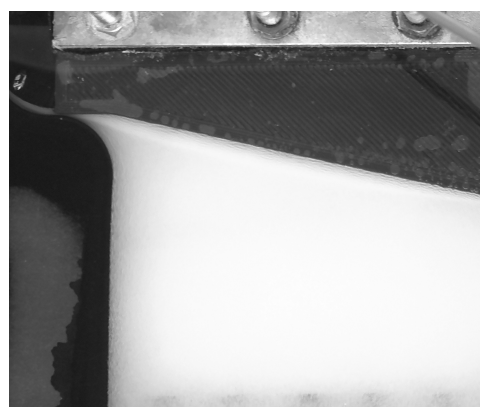


**Figure E.32:** Image of the Anode side at liquid flow rate: 70.32 mL/min

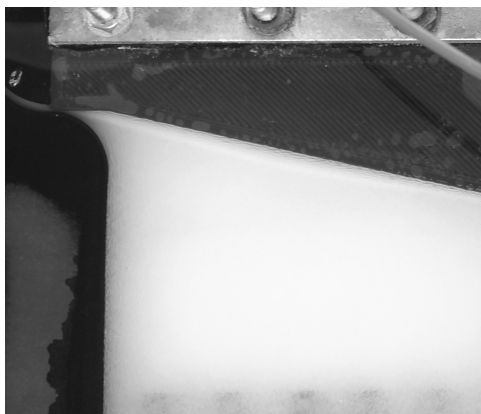


**Figure E.33:** Image of the Anodeside at liquid flow rate: 82.04 mL/min

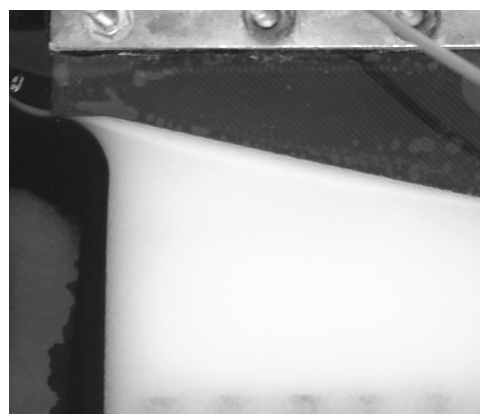


**Figure E.34:** Image of the Anode side at liquid flow rate: 93.76 mL/min

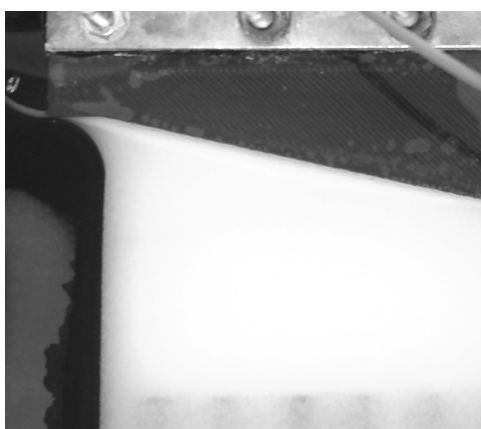


**Figure E.35:** Image of the Anode side at liquid flow rate: 105.48 mL/min

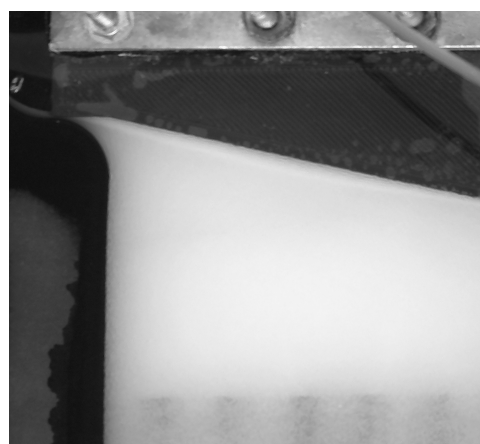


**Figure E.36:** Image of the Anode side at liquid flow rate: 117.2 mL/min

### E.3. Constant liquid flow rate: 70 mL/min

#### E.3.1. Gas flow rate regime: O<sub>2</sub>: 20 - 98 mL/min, H<sub>2</sub>: 39 - 196 mL/min

##### Cathode side

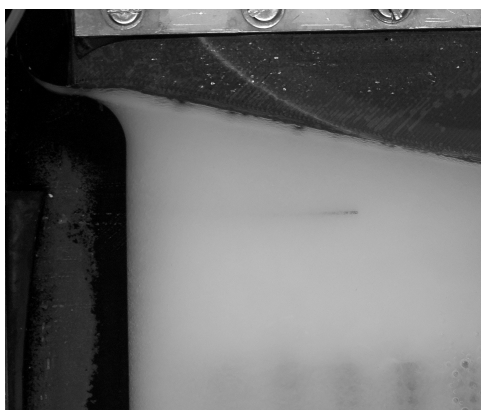


**Figure E.37:** Image of the Cathode side at gas flow rate: 39 mL/min

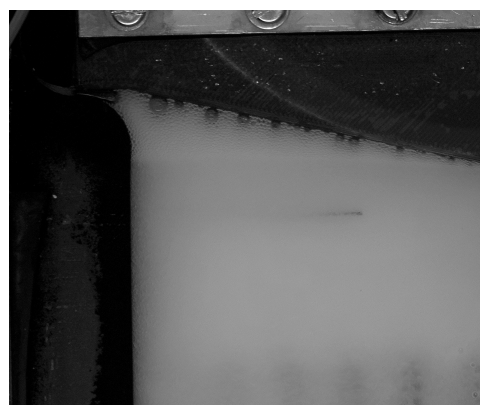


**Figure E.38:** Image of the Cathode side at gas flow rate: 59 mL/min

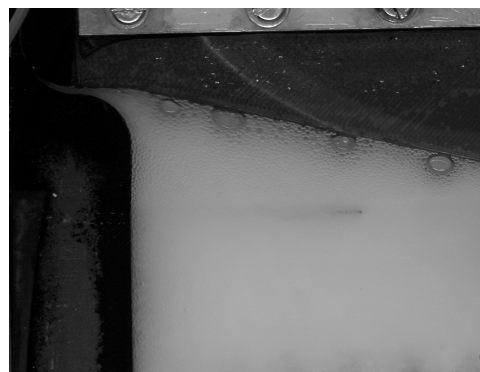
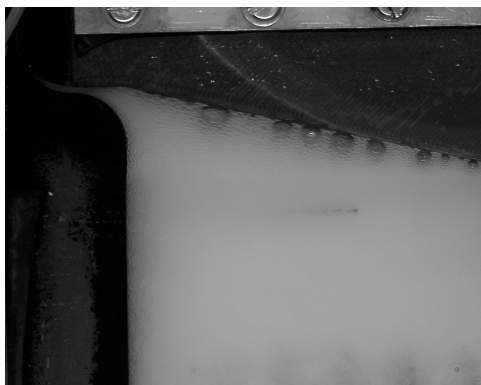


**Figure E.39:** Image of the Cathode side at gas flow rate: 78 mL/min **Figure E.40:** Image of the Cathode side at gas flow rate: 98 mL/min



**Figure E.41:** Image of the Cathode side at gas flow rate: 117 mL/min **Figure E.42:** Image of the Cathode side at gas flow rate: 137 mL/min

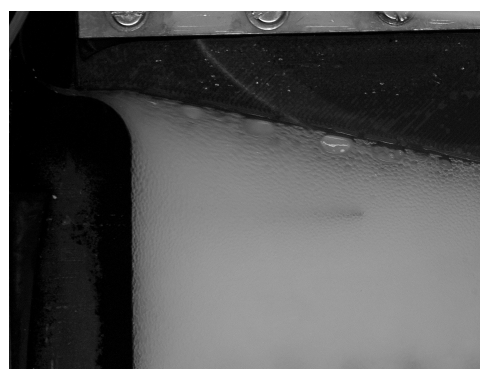
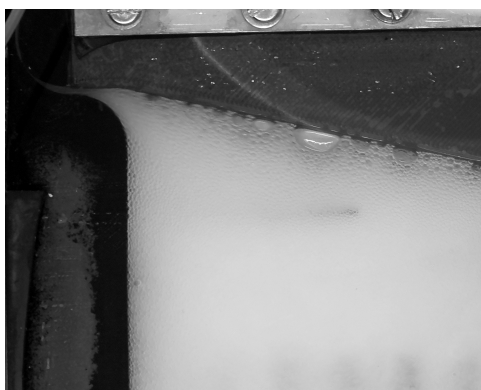


**Figure E.43:** Image of the Cathode side at gas flow rate: 157 mL/min **Figure E.44:** Image of the Cathode side at gas flow rate: 176 mL/min

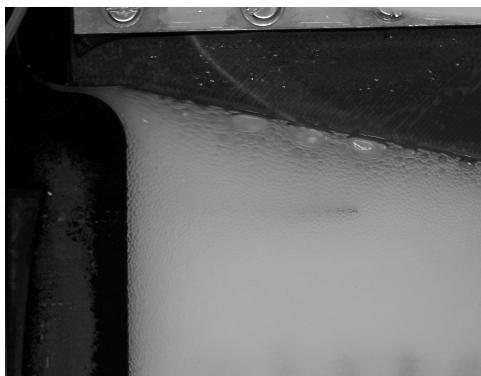


**Figure E.45:** Image of the Cathode side at gas flow rate: 196 mL/min

**Anode side**



**Figure E.46:** Image of the Anode side at gas flow rate: 20 mL/min



**Figure E.47:** Image of the Anode side at gas flow rate: 29 mL/min

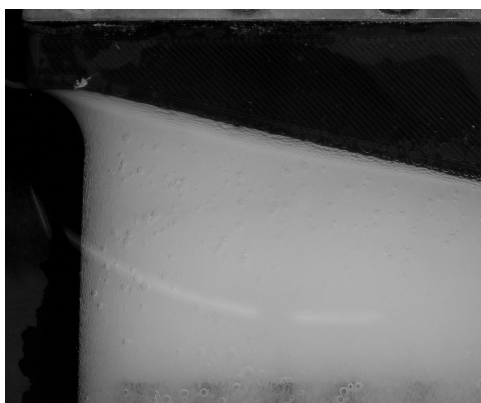


**Figure E.48:** Image of the Anode side at gas flow rate: 39 mL/min



**Figure E.49:** Image of the Anode side at gas flow rate: 49 mL/min

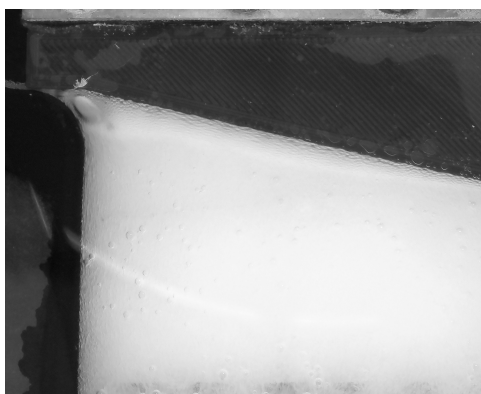


Figure E.50: Image of the Anode side at gas flow rate: 59 mL/min



Figure E.51: Image of the Anode side at gas flow rate: 69 mL/min



Figure E.52: Image of the Anode side at gas flow rate: 78 mL/min



Figure E.53: Image of the Anode side at gas flow rate: 88 mL/min



Figure E.54: Image of the Anode side at gas flow rate: 97 mL/min

# F

## Potential difference measurements along the manifolds

The graphs below are the results of the potential difference measurements. The potential differences measured with the reference electrodes are used to calculate the shunt currents. This is done by dividing the average potential difference over a time interval of 10 minutes, which equals a certain flow rate and current density, by the respective manifold resistance that corresponds to that regime of liquid flow rate and current density. All measurements portrayed below have been executed three times and the average of those three was used for the calculations.

### F.1. Constant current of $278 \text{ mA/cm}^2$ , variable flow rate: 0.596 - 47.68 mL/min

At this current density, the  $\text{O}_2$  gas flow rate is 78 mL/min and the  $\text{H}_2$  gas flow rate is 157 mL/min.

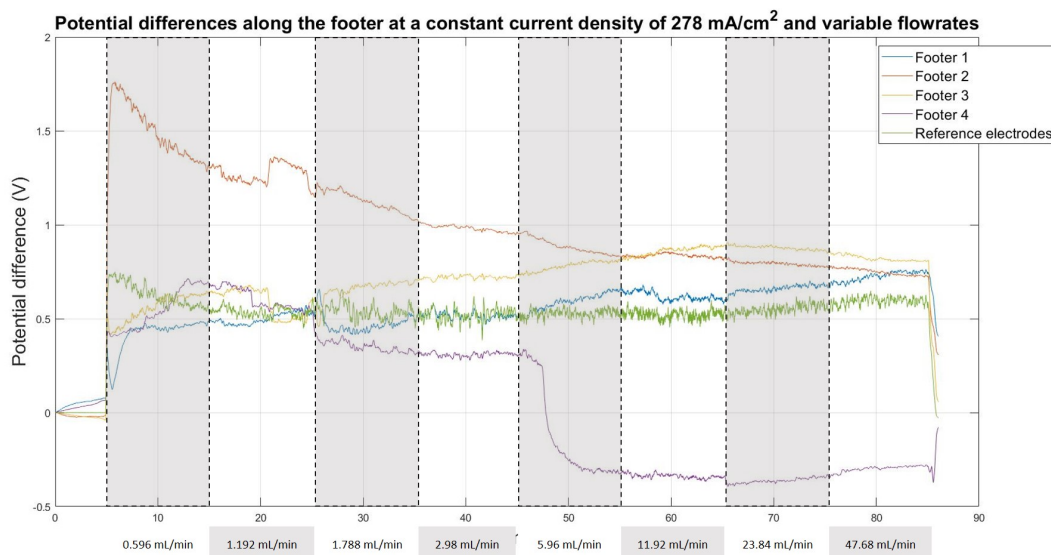


**Figure F.1:** Potential differences along the Footer measured with (pseudo)reference electrodes of the lowest flow rate regime. Footer 1-4 indicate the potential differences measured with the silver wires.

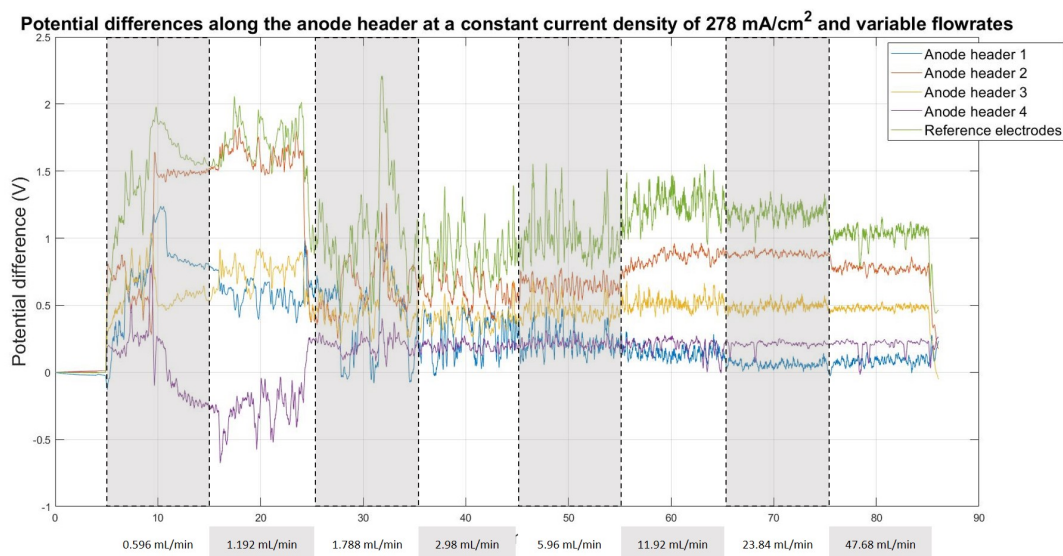


**Figure F.2:** Potential differences along the Anode header measured with (pseudo)reference electrodes of the lowest flow rate regime. Anode header 1-4 indicate the potential differences measured with the silver wires.

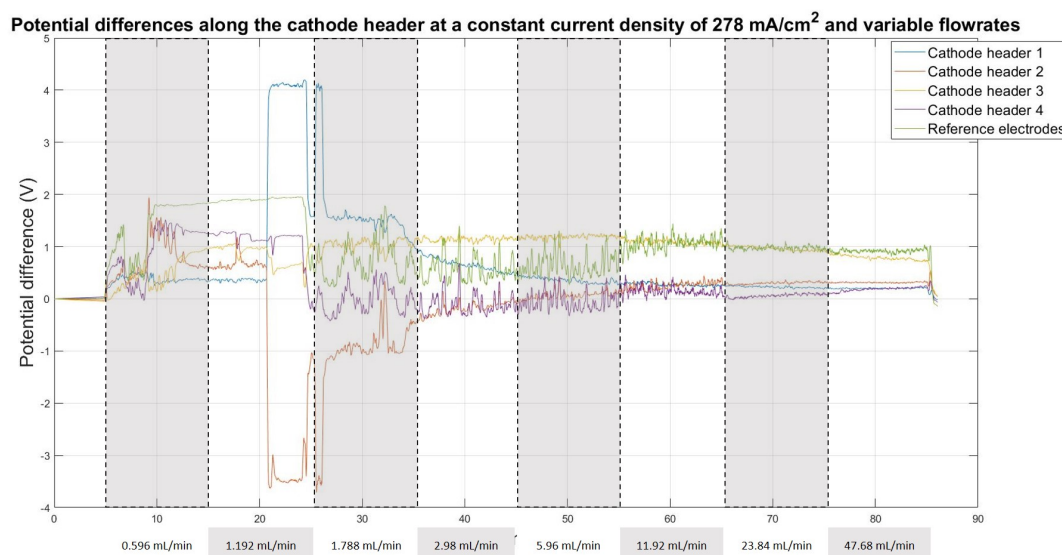


**Figure F.3:** Potential differences along the Cathode header measured with (pseudo)reference electrodes of the lowest flow rate regime. Cathode header 1-4 indicate the potential differences measured with the silver wires.

## F.2. Constant current of 139 mA/cm<sup>2</sup>, variable flow rate: 11.72 - 117.2 mL/min

At this current density, the O<sub>2</sub> gas flow rate is 39 mL/min and the H<sub>2</sub> gas flow rate is 78 mL/min.

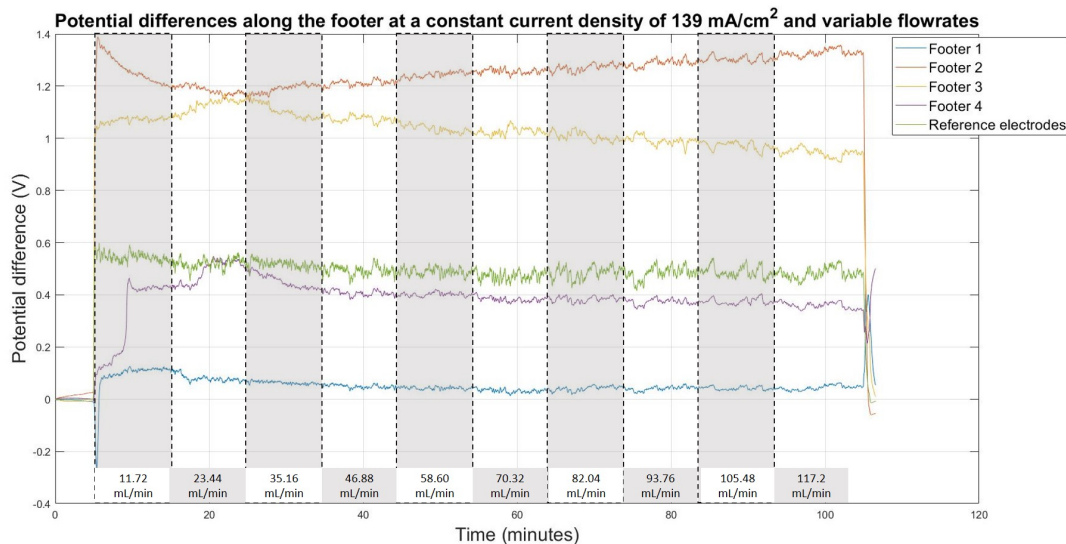


**Figure F.4:** Potential differences along the Footer measured with (pseudo)reference electrodes of the middle flow rate regime. Footer 1-4 indicate the potential differences measured with the silver wires.

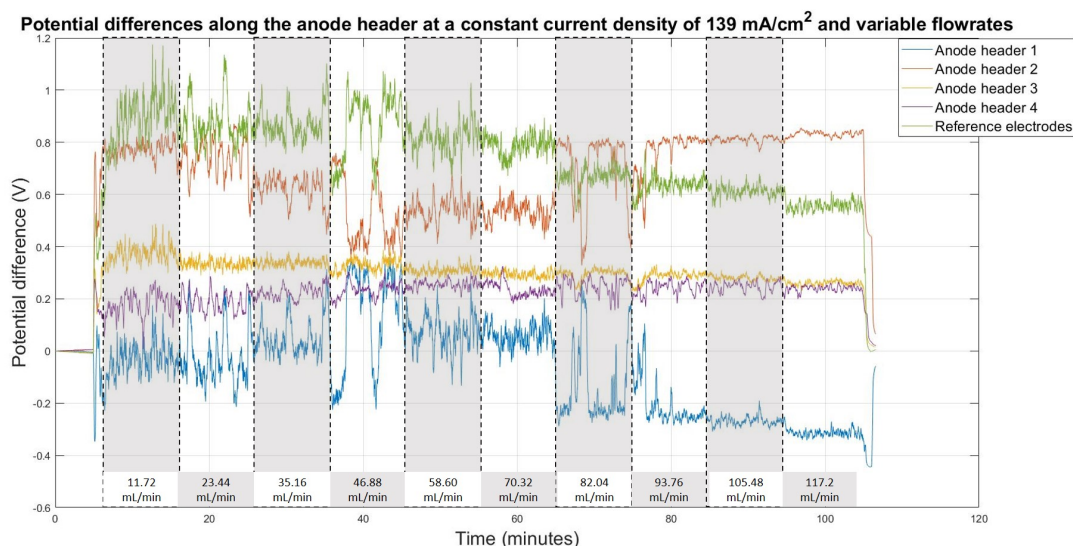


**Figure F.5:** Potential differences along the Anode header measured with (pseudo)reference electrodes of the lowest flow rate regime. Anode header 1-4 indicate the potential differences measured with the silver wires.

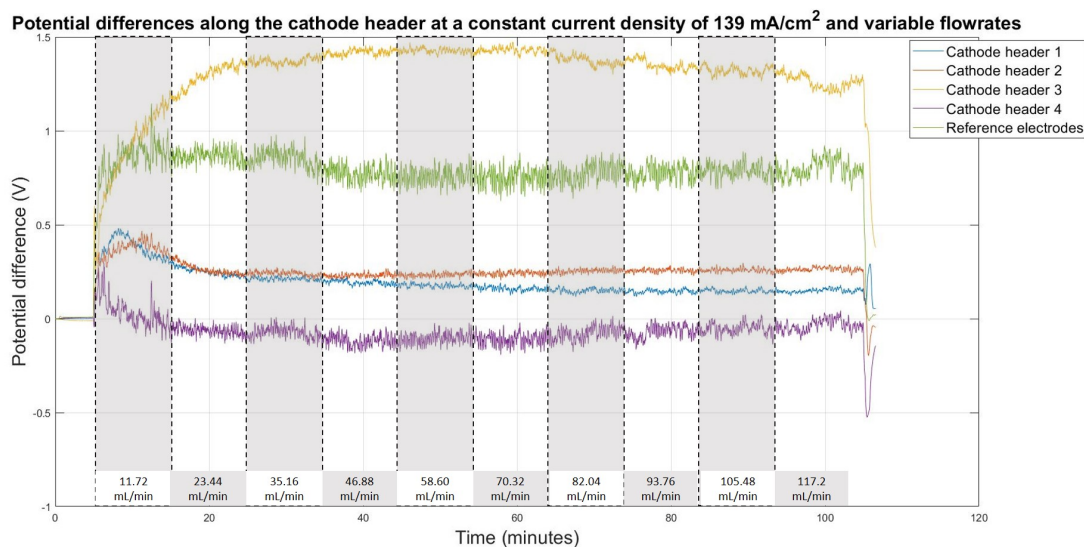


**Figure F.6:** Potential differences along the Cathode header measured with (pseudo)reference electrodes of the middle flow rate regime. Cathode header 1-4 indicate the potential differences measured with the silver wires.

### F.3. Constant current of 139 mA/cm<sup>2</sup>, variable flow rate: 68.4 - 475.8 mL/min

At this current density, the O<sub>2</sub> gas flow rate is 39 mL/min and the H<sub>2</sub> gas flow rate is 78 mL/min.

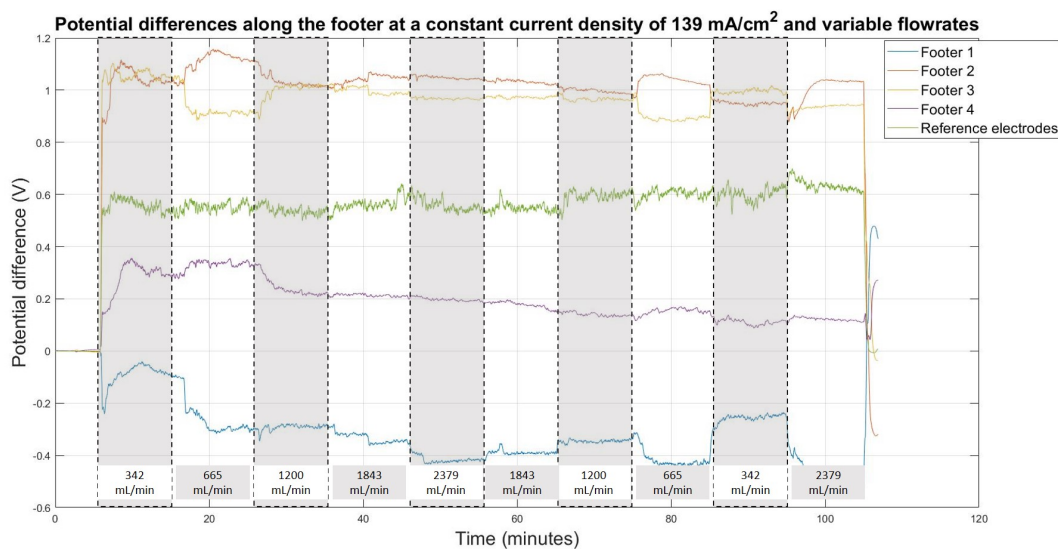


**Figure F.7:** Potential differences along the Footer measured with (pseudo)reference electrodes of the high flow rate regime. Footer 1-4 indicate the potential differences measured with the silver wires.

F.4. Constant liquid flow rate of 70 mL/min per cel, variable current density: 69.4 - 347.2 mA/cm<sup>2</sup>

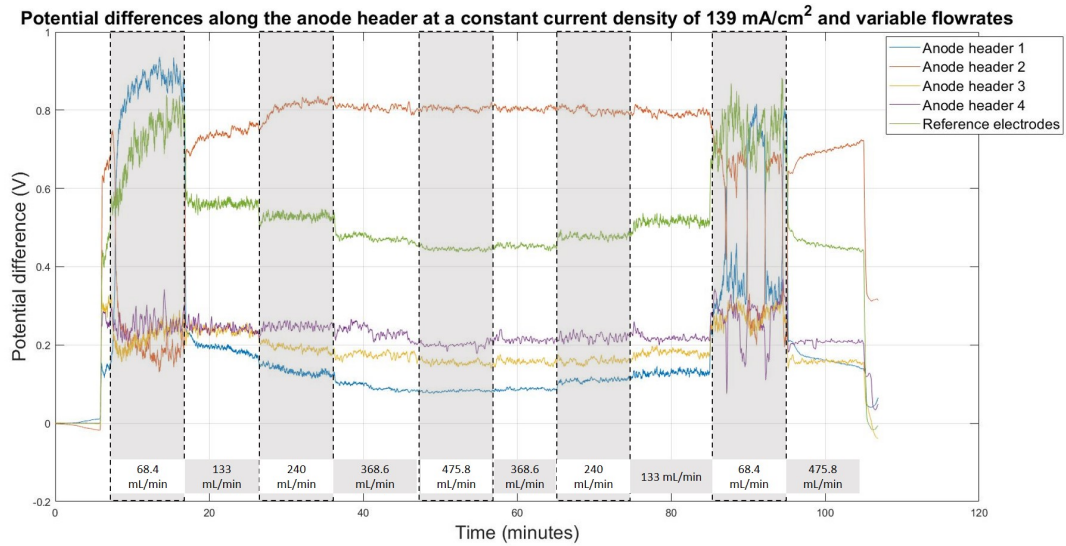


**Figure F.8:** Potential differences along the Anode header measured with (pseudo)reference electrodes of the high flow rate regime. Anode header 1-4 indicate the potential differences measured with the silver wires.

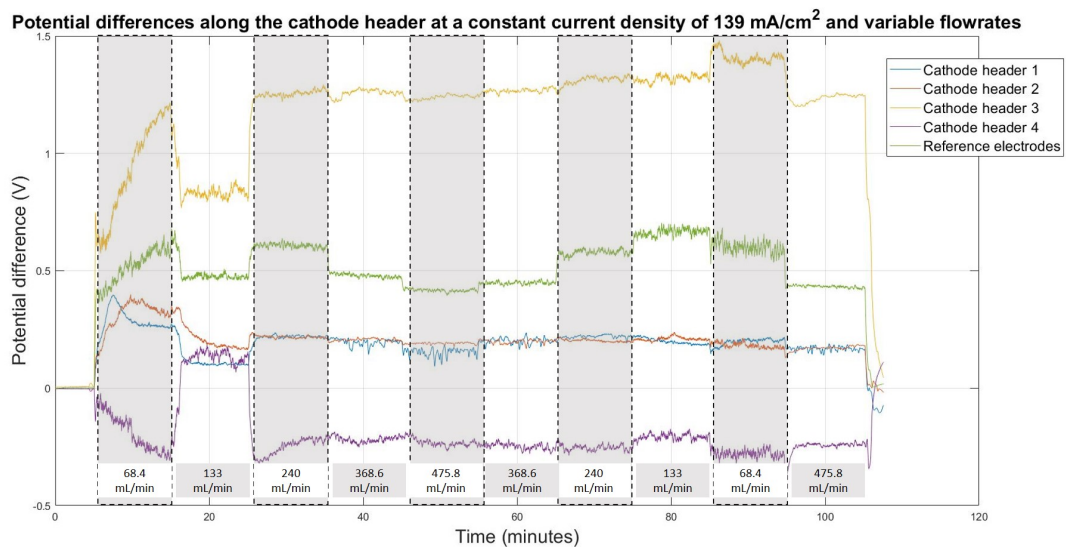


**Figure F.9:** Potential differences along the Cathode header measured with (pseudo)reference electrodes of the high flow rate regime. Cathode header 1-4 indicate the potential differences measured with the silver wires.

**F.4. Constant liquid flow rate of 70 mL/min per cel, variable current density: 69.4 - 347.2 mA/cm<sup>2</sup>**

At these current densities, the O<sub>2</sub> gas flow rate vary between 20 and 98 mL/min and the H<sub>2</sub> gas flow rate vary between 39 and 196 mL/min.

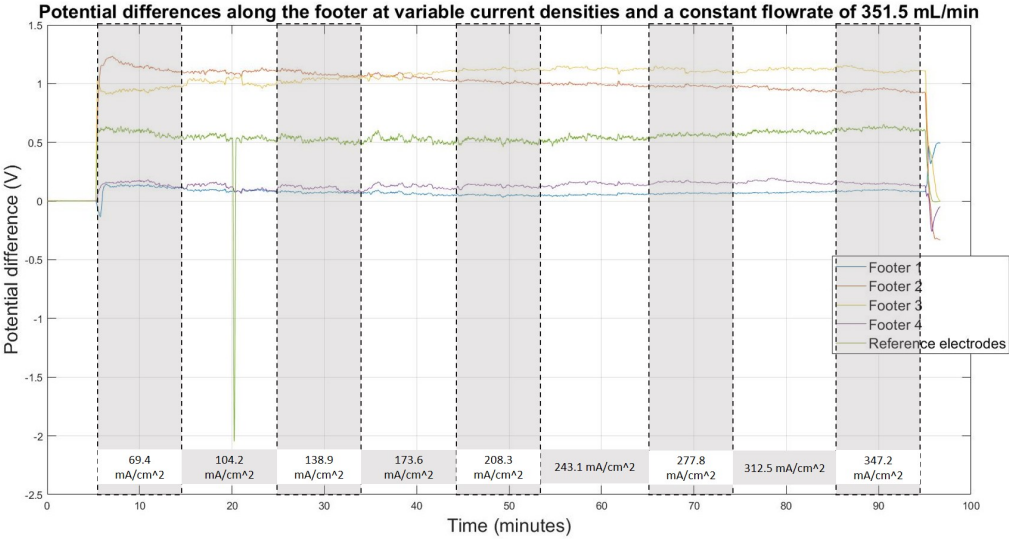


Figure F.10: Potential differences along the Footer measured with (pseudo)reference electrodes of the variable current regime. Footer 1-4 indicate the potential differences measured with the silver wires.

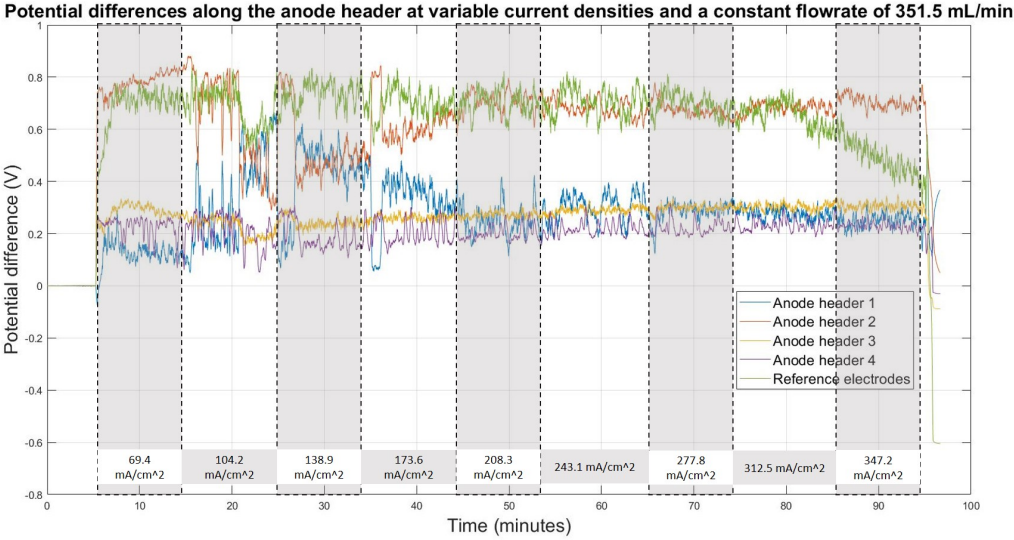
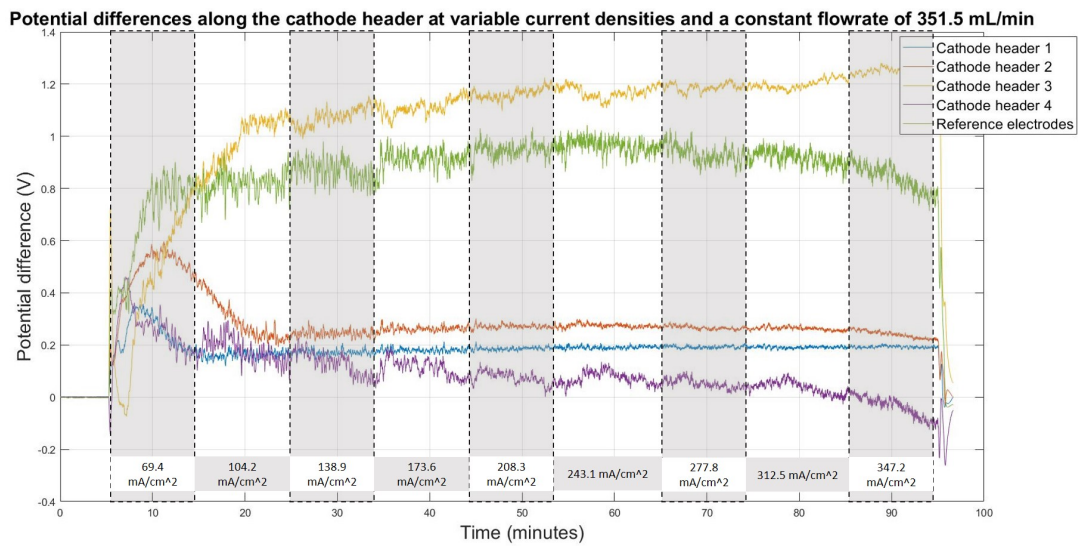


Figure F.11: Potential differences along the Anode header measured with (pseudo)reference electrodes of the variable current regime. Anode header 1-4 indicate the potential differences measured with the silver wires.



**Figure F.12:** Potential differences along the Cathode header measured with (pseudo)reference electrodes of the variable current regime. Cathode header 1-4 indicate the potential differences measured with the silver wires.

# G

## Shunt current vs void fraction

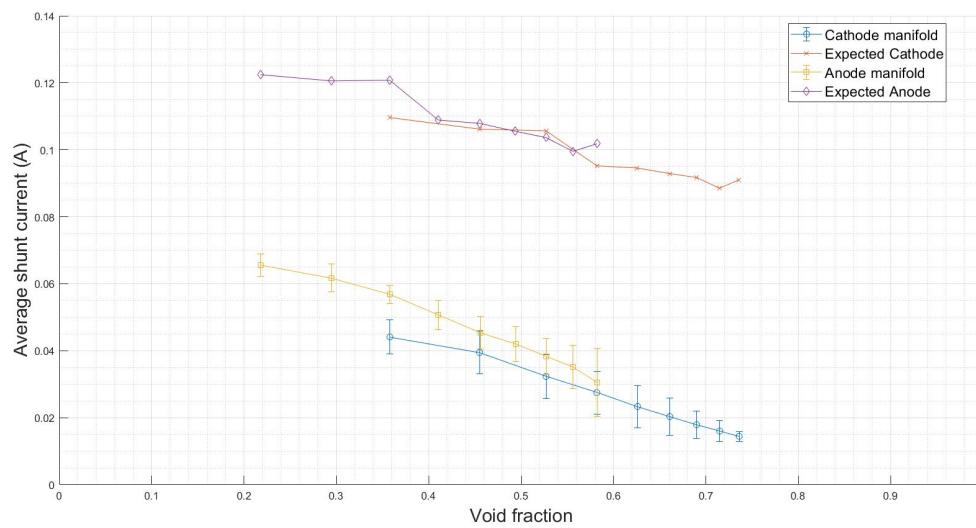


**Figure G.1:** Shunt current vs void fraction for a constant electrolyte flow rate of 70 mL/min. The  $H_2$  gas flow rate ranges from 39 to 196 mL/min and the  $O_2$  flow rate ranges from 20 to 98 mL/min.